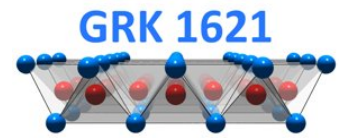




TECHNISCHE
UNIVERSITÄT
DRESDEN



Advanced Cluster Methods for Correlated-Electron Systems

DISSERTATION

zur Erlangung des akademischen Grades

Doctor rerum naturalium

(Dr. rer. nat.)

vorgelegt der

Fakultät Mathematik und Naturwissenschaften

der Technischen Universität Dresden

von

Dipl. Phys. André Fischer

geboren am 24.05.1987 in Erfurt

Eingereicht am 27.04.2015

Die Dissertation wurde in der Zeit von 01/2012 bis 04/2015 am Leibniz-Institut
für Festkörper- und Werkstoffforschung (IFW) Dresden angefertigt.

1. Gutachter: Prof. Jeroen van den Brink
2. Gutachter: Prof. Maria Daghofer

There is a theory which states that if ever anyone discovers exactly what the Universe is for and why it is here, it will instantly disappear and be replaced by something even more bizarre and inexplicable.

There is another theory which states that this has already happened.

Douglas Adams

Contents

1	Introduction	1
2	Quantum Cluster Theories	5
2.1	The Hubbard Model	7
2.2	Cluster Perturbation Theory	9
2.2.1	Introduction	9
2.2.2	CPT for a Noninteracting System	10
2.2.3	Interacting Systems	11
2.2.4	Diagrammatic Approach	12
2.3	Self-Energy-Functional Approach	15
2.4	Variational Cluster Approach	17
2.5	Cluster Solvers	20
2.5.1	Cluster Geometry	21
2.5.2	Limiting Cases	22
3	Superconductivity and Magnetic Ordering on Triangular Lattices	23
3.1	Introduction	24
3.2	Candidates for Stable Phases	25
3.2.1	Magnetically Ordered Phases	25
3.2.2	Superconducting Phases	31
3.3	Methodology	36
3.4	Results	44
3.4.1	SDW Phases on a 12-site Cluster	44
3.4.2	Results Using a Minimal 4-site Cluster	46
3.4.3	Results Using 8-site Clusters	48
3.4.4	Superconducting Phases on a 7-site Cluster	57
3.4.5	Properties of the SDW Phases	62
3.4.6	Properties of the Superconducting Phases	66
3.4.7	Effects of the Cluster Shape	68
3.5	Conclusions	72
4	Breaking of Fourfold Lattice Symmetry in Iron-based Superconductors	77

4.1	Introduction: The Nematic Phase of Iron Pnictides	79
4.2	Model and Method	83
4.3	Results	90
4.4	Conclusions	95
5	Summary and Outlook	97
	Bibliography	101
	Zusammenfassung auf Deutsch	119
	Acknowledgements	121
	Publication List	123

1 Introduction

As the quest for novel materials with new properties has always been important within the scientific community, correlated-electron systems have been in the focus of solid-state physics for several decades with novel compounds being discovered from time to time. Milestones definitely include the discovery of cuprate superconductors in 1986 and the more recent discovery of high-temperature superconductivity in iron-based compounds in 2008. While cuprate superconductors are about to reach their 30th birthday, the investigation of the mechanism that drives superconductivity within these compounds is still ongoing and several challenges are still to be overcome.

The situation for the iron-based superconductors is similar: After an exciting period with the discovery of superconductivity in a lot of compounds in 2008 and 2009 with a peak critical temperature of around 55 K, the curve flattened out and no higher transition temperatures could be reached in the following years. Still, the desire to clarify the mechanisms within these materials is strong because an understanding of the microscopic mechanisms might support the search for materials with desired properties while offering hints which material parameters should be tuned.

Theoretical descriptions of correlated-electron systems are therefore highly sought after and a variety of methods have been developed within the past decades. In correlated materials, the strength of the interactions is comparable to the kinetic energy, making perturbative approaches unsuitable. Within partially filled d or f shells each electron has a strong influence on its neighborhood, making the application of one-electron approaches, such as local-density approximation (LDA), static mean-field theory or Hartree-Fock theory questionable. Instead, new approaches are introduced, which are capable of including electronic correlation effects. For instance, LDA can be extended by the introduction of the Coulomb repulsion U (LDA+ U) or by using the GW approximation. Also, the relatively simple Hubbard model has been successfully applied to correlated systems, for example within dynamical mean-field theory (DMFT).

A striking feature of systems with interacting electrons is a rich phase diagram show-

ing several kinds of phases. A variety of magnetically ordered phases, charge density wave phases or superconducting states with unconventional order parameters may develop. In many cases the dimensionality is lowered to 2D planes due to a layered structure of the compound, enhancing the complexity of the phase diagram even more. Additionally, electron itinerancy plays a central role in the determination of arising ordered phases.

Since the complexity of these systems is rather high, powerful numerical methods are needed to treat the arising effects. Many of these methods are based on the idea of using the properties of finite systems to draw conclusions for the infinite system in the thermodynamic limit, for example quantum cluster methods. In Chapter 2 some of the most promising quantum cluster theories are presented with their advantages and downsides. Here, a special focus lies on cluster perturbation theory (CPT), which is presented in Sec. 2.2, and the variational cluster approach (VCA), explained in Sec. 2.4. The VCA is based on a self-energy-functional approach, which is presented in Sec. 2.3. CPT and the VCA are the methods of choice within this thesis as they allow a treatment of correlated systems beyond mean-field theory, while including short-ranged correlation numerically exactly within the solution of small to medium-sized clusters and treating long-ranged correlations at the mean-field level. The VCA can be seen as the variational extension of CPT. It permits the observation of spontaneous symmetry breaking by the inclusion of a variational principle based on self-energy-functional theory.

Within this thesis, the advantages of CPT and the VCA are used to gain deeper insight into two different correlated materials. In Chapter 3 possible ground states of the triangular lattice at $3/4$ filling are discussed. The phase diagrams of triangular lattices are extremely rich because geometric frustration is essential within this crystal structure. At a filling fraction of $3/4$, the electronic density of states shows a van Hove singularity and the Fermi surface is perfectly nested, allowing numerous magnetically ordered states and unconventional superconducting phases to develop. To decide between the different ground states, the VCA is applied in order to evaluate the grand potentials of the respective phases. The variety of possible ground states of the system is presented in Sec. 3.2. The results obtained from different cluster sizes are given in Sec. 3.4 and discussed subsequently.

Chapter 4 focuses on the materials class of the iron-based superconductors. Within a nematic phase slightly above the onset of magnetic order the fourfold lattice sym-

metry is broken down to a twofold symmetry. Here, mechanisms that might be responsible for the breaking of the symmetry are studied within a three-band model for the iron orbitals of the iron-pnictogen layer. The effects of an orbital ordering field are compared to anisotropic hoppings and anisotropic magnetic couplings. CPT allows a breaking of the symmetry between the x and y directions without imposing long-range magnetic order. The calculated spectral densities from Sec. 4.3 are then compared to angle-resolved photoemission spectroscopy (ARPES). An outlook is given in Sec. 5.

2 Quantum Cluster Theories

Electronic correlations are naturally important to describe magnetism, but they might be also a key to understand other effects arising in correlated systems, such as high-temperature superconductivity in various compounds, including curates [1] or iron-pnictides [2]. Because correlations definitely play an important role in these compounds, methods which treat these correlations as accurately as possible are highly sought after.

Severe problems arise when correlated materials are treated with analytical approaches. Since the magnitude of the different orders of a weak-coupling perturbation approach is generally not known, neglecting higher orders might result in losing important information. An unbiased insight into these compounds is therefore not possible within these methods. Within the regime of weak coupling, where correlations have in general long-range character, the random-phase approximation (RPA) and static mean-field methods deliver reasonable results. Since mean-field theories neglect local quantum fluctuations, these methods fail as soon as quantum fluctuations become important.

A direct calculation for a finite system is possible via exact diagonalization (ED) or quantum Monte Carlo (QMC) methods. ED is only applicable to very small clusters because of an exponential increase of effort. The effort of QMC calculations also increases exponentially by the size of the lattice and additionally with increased temperatures. A huge drawback of QMC is the sign problem at low temperatures. This problem even gets worse when frustration effects play a role. Both methods exhibit strong finite-size effects that cause problems when phase transitions should be determined, which is only possible within QMC using finite-size scaling.

A completely different ansatz would be starting from mean-field theory. Mean-field theories work in the thermodynamic limit and can therefore describe phases of long-range order, but they fail in describing correlation effects. Nevertheless, mean-field theories are very popular and successful. The general scheme consists of treating only a small number of degrees of freedom exactly while the rest acts as a mean field on this set. A prominent example is the coherent-potential approximation (CPA) [3–5].

A promising method which includes the thermodynamic limit and therefore is able to describe phases of long-range order is the dynamical mean-field theory (DMFT) [6, 7]. The DMFT maps the lattice problem onto a local impurity model connected to a self-consistent bath and allows the time-dependent inclusion of quantum fluctuations. Under the assumption of a momentum-independent (local) lattice self-energy also these fluctuations are only local. Because we are interested in different problems where short-range interactions become important, DMFT alone might not be sufficient, although its great success within the last 25 years, especially if combined with numerical band structure methods.

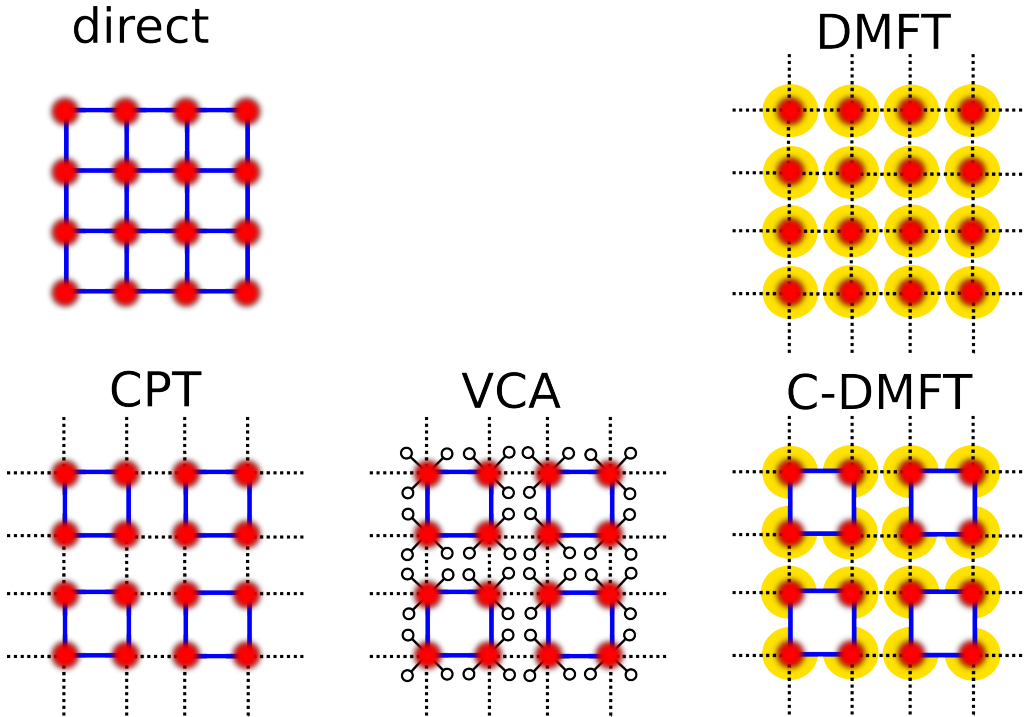


Figure 2.1: Overview over various cluster theories for 2D Hubbard models. Solid, blue lines denote intra-cluster hopping, dashed black lines denote inter-cluster hopping. Red circles denote on-site interactions, while open circles denote bath sites and large, yellow circles denote a mean-field bath with $n_b = \infty$. Adapted from Potthof *et al.* [8].

To be able to treat these nonlocal fluctuations, cluster methods like the ones presented in Fig. 2.1 are promising candidates as they include a direct solution of finite clusters via ED and therefore incorporate correlations and quantum fluctuations numerical exactly as long as their length scales do not exceed the size of the cluster. The dynamical cluster approximation (DCA) [9] and the cellular DMFT (C-DMFT) [10] are the most important examples for a fully causal self-consistent method where nonlocal fluctuations are included.

Regarding the two main topics of this thesis, different approaches have been chosen. For the calculations within the nematic phase of the iron pnictides, cluster perturbation theory (CPT) [11, 12] may be a promising candidate as it allows to switch off long-range magnetic order. For the calculations of magnetic and superconducting ground states in triangular lattices the variational extension of CPT, the variational cluster approach (VCA) [8, 13, 14], seems well suited. Because QMC severely suffers from the sign problem due to geometrical frustration and is therefore not suited as an impurity solver, the VCA allows a rather unbiased view on the problem by allowing relatively large cluster sizes.

A major task within these theories lies in the solution of the impurity problem. Reducing the number of bath sites may result in more effective algorithms since the loss of additional information may be very small. As shown in Fig. 2.1, CPT and C-DMFT can be seen as special cases of a general cluster approach, which has been named self-energy-functional theory (SFT) by its creator Potthoff [8, 15]. While C-DMFT works with an infinite number of bath sites and the CPT does not include bath sites at all, the SFT allows an arbitrary number of bath sites while keeping causality and thermodynamic consistency. A detailed description of the SFT will be given in Sec. 2.3. In Sec. 2.4 the variational cluster approach (VCA), a variational principle based on the SFA, will be presented following studies of Potthoff *et al.* [8, 13].

2.1 The Hubbard Model

The Model introduced independently by Martin Gutzwiller [16], Junjiro Kanamori [17] and John Hubbard [18] in 1963 provides an approach to access the physics of interacting particles on a lattice [19]. It allows to gain insight how metallic, insulating and high-temperature superconducting properties are affected by the strength of electronic interactions. It was originally applied to describe transition metal oxides, but it became an important model to describe the properties of heavy fermion systems and high-temperature superconductors.

The simplest form of a Hubbard Hamiltonian for a model with only one orbital per site can be written as

$$H = -t \sum_{\langle i,j \rangle, \sigma} \left(c_{i,\sigma}^\dagger c_{j,\sigma} + \text{H.c.} \right) + U \sum_i n_{i,\uparrow} n_{i,\downarrow} - \mu \sum_i n_i, \quad (2.1)$$

where the first term is a simple *tight-binding* term, describing the kinetic hopping of electrons between adjacent sites i and j . Here, $c_{i,\sigma}^\dagger$ and $c_{j,\sigma}$ are second-quantized creation and annihilation operators and σ denotes the spin. The amplitude of the hopping is provided by the transfer integral t of the atomic Wannier orbitals $\Phi_{i,\sigma}(\mathbf{r})$ of the respective sites i and j ,

$$t = \int d^3r \Phi_{i,\sigma}(\mathbf{r}) \frac{\hbar^2}{2m} \Delta \Phi_{j,\sigma}(\mathbf{r}). \quad (2.2)$$

If one considers only the first term, electrons can hop independently between neighboring sites with the kinetic energy $-t$. The additional second term in Eq. (2.1) describes the *on-site* Coulomb repulsion of electrons on a doubly occupied site. The strength of this repulsion is mediated by the Hubbard parameter U and $n_{i,\sigma} = c_{i,\sigma}^\dagger c_{i,\sigma}$ is the number operator. This term is in general competing with the first term. When U dominates over t , the Hubbard model predicts a metal-insulator transition resulting in the formation of a *Mott insulator*. The third term of Eq. (2.1) controls the particle number within the system via the chemical potential μ . While the model Hamiltonian can be easily written down, its complexity lies in the application to complex physical systems.

While simple systems can successfully be treated by Eq. (2.1) [20, 21], the desire to study more complex problems requires generalizations and the inclusion of additional terms. For example, a system with more than one band would require an additional band index ν and the hopping matrix $t_{i,j,\nu,\nu'}$ would now also include intraband hopping $\nu \rightarrow \nu$ and additional interband hopping between different orbitals $\nu \rightarrow \nu'$.

There exists a variety of multi-orbital materials with partially filled d shells where multiple bands contribute to the Fermi surface and orbital degeneracy plays a central role, such as iron pnictides or iron chalcogenides. These materials exhibit rather strong electronic correlations while they are in a metallic state far away from a Mott insulator. To accurately describe these materials additional interactions have to be taken into account [22, 23]. Such interactions can be written as Coulomb

integrals

$$U = \int d^3r d^3r' |\Phi_m(\mathbf{r})|^2 V_c(\mathbf{r}, \mathbf{r}') |\Phi_m(\mathbf{r}')|^2, \quad (2.3)$$

$$U' = \int d^3r d^3r' |\Phi_m(\mathbf{r})|^2 V_c(\mathbf{r}, \mathbf{r}') |\Phi_{m'}(\mathbf{r}')|^2, \quad (2.4)$$

$$J = \int d^3r d^3r' \Phi_m(\mathbf{r}) \Phi_{m'}(\mathbf{r}) V_c(\mathbf{r}, \mathbf{r}') \Phi_m(\mathbf{r}') \Phi_{m'}(\mathbf{r}'), \quad (2.5)$$

if effects of crystal field splitting are neglected. To minimize the resulting intra-atomic exchange energy, the system has to follow *Hund's rules* [24]. The interaction part H_{int} of the Hubbard Hamiltonian is then enhanced and given by [25, 26]

$$\begin{aligned} H_{\text{int}} = & U \sum_{i,\nu} n_{i,\nu,\uparrow} n_{i,\nu,\downarrow} + (U' - J/2) \sum_{i,\nu < \nu'} n_{i,\nu} n_{i,\nu'} \\ & - 2J \sum_{i,\nu < \nu'} \mathbf{S}_{i,\nu} \mathbf{S}_{i,\nu'} + J' \sum_{i,\nu < \nu'} (c_{i,\nu,\uparrow}^\dagger c_{i,\nu,\downarrow}^\dagger c_{i,\nu',\downarrow} c_{i,\nu',\uparrow} + \text{H.c.}), \end{aligned} \quad (2.6)$$

with the intraorbital Coulomb repulsion U , the interorbital repulsion U' , Hund's rule coupling J and pair hopping $J' = J$. $\mathbf{S}_{i,\nu} = \frac{1}{2} \sum_{\sigma,\sigma'} c_{i,\nu,\sigma}^\dagger \boldsymbol{\sigma}_{\sigma,\sigma'} c_{i,\nu,\sigma}$ is the electron-spin operator with the vector of the Pauli matrices $\boldsymbol{\sigma} = (\sigma^x, \sigma^y, \sigma^z)$.

2.2 Cluster Perturbation Theory

2.2.1 Introduction

The cluster perturbation theory was presented by S  n  chal *et al.* [12] in 2000 and combines Lanczos' exact diagonalization [27, 28] (ED) with strong-coupling perturbation theory [29]. The central idea of this method is to divide the lattice into identical clusters and evaluate the one-particle Green's function

$$G_{a,b}(z) = \langle \Omega | c_a \frac{1}{z - H} c_b^\dagger | \Omega \rangle + \langle \Omega | c_b^\dagger \frac{1}{z + H} c_a | \Omega \rangle \quad (2.7)$$

within an isolated cluster. Here, z is a complex frequency, a and b denote lattice sites within the cluster and c_a is the electron destruction operator at site a . The Hamiltonian is given by H and $|\Omega\rangle$ is the ground state obtained by ED. The Green's function of the isolated cluster is then used to calculate the Green's function of the infinite system, $G_{\mathbf{Q},a,b}(z)$, where \mathbf{Q} denotes the superlattice wave vector. With this approach, short-range correlations are calculated numerically exact within the framework of ED while long-range interactions are treated on an RPA-like level.

2.2.2 CPT for a Noninteracting System

In the case of a noninteracting system the CPT approach is very easy to apply [13]. An entirely kinetic Hamiltonian

$$H_0 = \sum_{a,b,\sigma} \left(t_{a,b} c_{a,\sigma}^\dagger c_{b,\sigma} + \text{H.c.} \right) \quad (2.8)$$

is divided into separated identical clusters

$$H'_0 = \sum_{a,b,\sigma} \left(t'_{a,b} c_{a,\sigma}^\dagger c_{b,\sigma} + \text{H.c.} \right) \quad (2.9)$$

and an intercluster hopping matrix \mathbf{V} , which contains all hopping elements between neighboring clusters. This is done the same way as in Fig. 2.2, just without Coulomb interaction. The hopping matrix \mathbf{t} is then described by $\mathbf{t} = \mathbf{t}' + \mathbf{V}$ and a solution for the system can be given via Green's function formalism. The noninteracting Green's function

$$\mathbf{G}_0(z) = \frac{1}{z + \mu - \mathbf{t}}, \quad (2.10)$$

where z is a complex frequency and μ is the chemical potential, can be easily calculated using the cluster Green's function

$$\mathbf{G}'_0(z) = \frac{1}{z + \mu - \mathbf{t}'}. \quad (2.11)$$

This immediately leads to the equation

$$\mathbf{G}_0(z) = \mathbf{G}'_0(z) + \mathbf{G}'_0(z) \mathbf{V} \mathbf{G}_0(z). \quad (2.12)$$

For noninteracting systems an exact solution for the Green's function can be found by solving Eq. (2.12),

$$\mathbf{G}_0(z) = \frac{1}{\mathbf{G}'_0(z)^{-1} - \mathbf{V}}, \quad (2.13)$$

provided that a solvable reference system with \mathbf{G}'_0 can be found, which might not be difficult since there are no interactions. A single isolated site would provide the simplest example of a solvable reference system. Because no approximations have been made in the above derivation the CPT procedure becomes exact in the noninteracting limit by being just an awkward way of performing a Fourier transformation. The main interest lies of course in interacting systems where CPT gets useful and, according to its name, perturbative.

2.2.3 Interacting Systems

We consider the full Hubbard Hamiltonian of the system,

$$H = H_0 + H_1 = \sum_{a,b,\sigma} \left(t_{a,b} c_{a,\sigma}^\dagger c_{b,\sigma} + \text{H.c.} \right) + U \sum_i n_{i,\uparrow} n_{i,\downarrow}, \quad (2.14)$$

with the noninteracting part H_0 and the interacting part H_1 , whose strength is given by the Coulomb repulsion U . One can split up the noninteracting Hamiltonian $H_0 = H'_0 + V$ into an intraccluster part

$$H'_0 = \sum_{m,a,b} \left(t_{m,a,b} c_{m,a}^\dagger c_{m,b} + \text{H.c.} \right) \quad (2.15)$$

and an intercluster part

$$V = \sum_{m,n,a,b} V_{a,b}^{m,n} c_{m,a}^\dagger c_{n,b}, \quad (2.16)$$

where $m, n \in \mathbb{Z}$ denotes the cluster number and the intercluster hopping is given by $V_{a,b}^{m,n}$. In Fig. 2.2 this process has been visualized. We dropped the spin index σ for convenience.

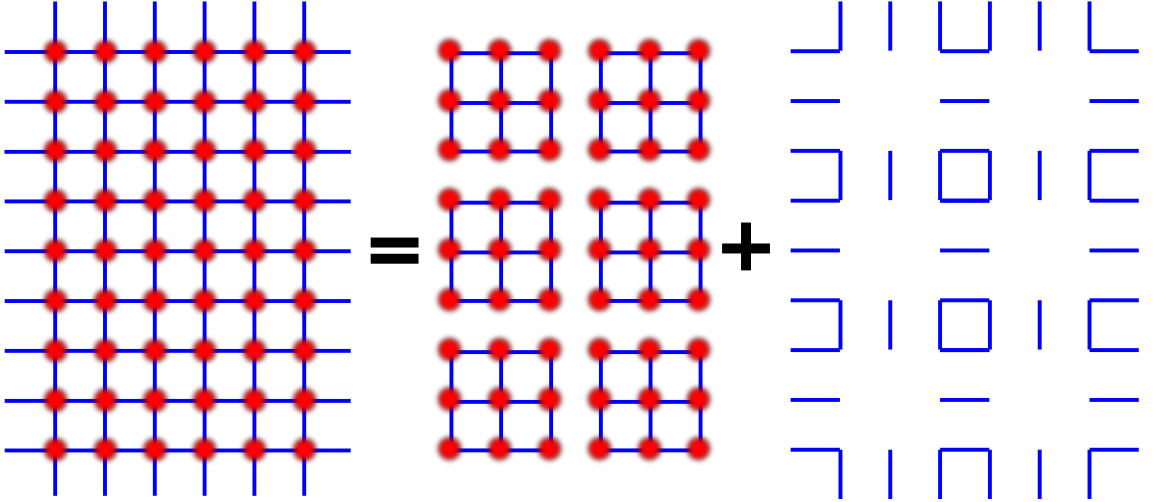


Figure 2.2: Division of a 2D Hubbard model with pure nearest neighbor hopping (blue lines) and on-site Coulomb interaction (red balls) into isolated clusters and an intercluster hopping V described by Eq. (2.16).

Following [12, 29], strong coupling perturbation theory is applied to calculate the Green's function $G_{a,b}(\mathbf{Q}, z)$ with the superlattice wave vector \mathbf{Q} , where the lowest order contribution is given by

$$G_{a,b}(\mathbf{Q}, z) = \left(\frac{\mathbf{G}'(z)}{1 - \mathbf{V}(\mathbf{Q})\mathbf{G}'(z)} \right)_{a,b}. \quad (2.17)$$

Here, $\mathbf{G}'(z)$ is a $N \times N$ matrix generalization of the atomic Green function in the space of the site indices of the cluster and \mathbf{V} is the superlattice representation of the hopping. Eq. (2.17) can also be understood as a generalization of the Hubbard-I approximation [18]. Instead of single sites in the Hubbard-I approximation, now clusters are coupled, allowing the treatment of short-range correlations. As $G_{a,b}(\mathbf{Q}, z)$ denotes the Green's function in real space inside the cluster and in reciprocal space outside the cluster a Fourier transform is applied to get the CPT Green's function in terms of the reciprocal space of the original lattice

$$\mathbf{G}_{\text{CPT}}(k, z) = \frac{1}{N} \sum_{a,b} e^{-ik(a-b)} G_{a,b}(Nk, z). \quad (2.18)$$

2.2.4 Diagrammatic Approach

In this section, a more intuitive approach is given by the use of diagrammatic language. At first, a noninteracting system from Sec. 2.2.2 is considered.

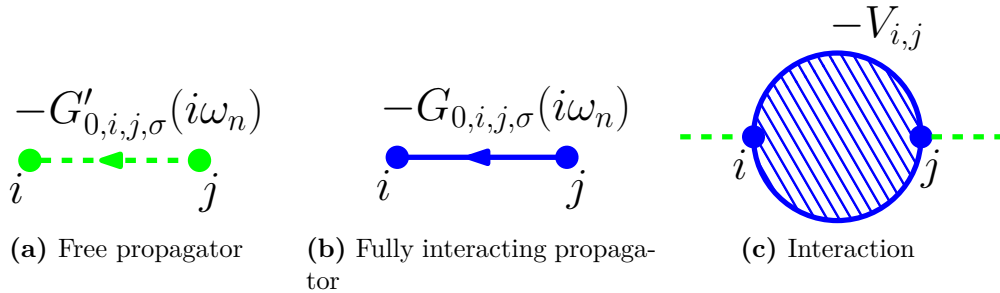


Figure 2.3: Diagrammatic approach to the noninteracting system.

To derive Eq. (2.12) diagrammatically we follow the notation of [13] and introduce the free propagator $G'_{0,i,j,\sigma}(i\omega_n)$ by a dotted green line (Fig. 2.3(a)) and the fully interacting propagator $G_{0,i,j,\sigma}(i\omega_n)$ by a straight blue line (Fig. 2.3(b)). The terms ‘free’ and ‘fully interacting’ are referring to scattering at the potential \mathbf{V} . Propagators from site i to site j carry a spin σ and a complex frequency $i\omega$. The scattering at the potential $V_{i,j}$ is pictured by a circle with links for an incoming and an outgoing propagator (Fig. 2.3(c)). Following Wick’s theorem one derives the fully interacting propagator by summing over all topologically different diagrams which are simply connected by free propagators, which has been visualized in Fig. 2.4.

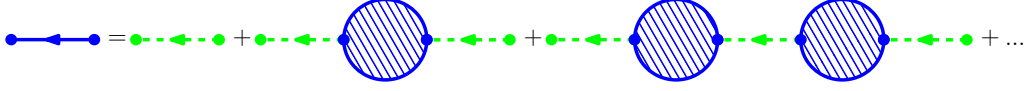


Figure 2.4: Summation over all simply connected diagrams.

Using a matrix representation of Fig. 2.4 directly leads to Dyson's equation:

$$\begin{aligned} \mathbf{G}_0 &= \mathbf{G}'_0 + \mathbf{G}'_0 \mathbf{V} \mathbf{G}'_0 + \mathbf{G}'_0 \mathbf{V} \mathbf{G}'_0 \mathbf{V} \mathbf{G}'_0 + \dots = \mathbf{G}'_0 + \mathbf{G}'_0 \mathbf{V} (\mathbf{G}'_0 + \mathbf{G}'_0 \mathbf{V} \mathbf{G}'_0 + \dots) \\ &= \mathbf{G}'_0 + \mathbf{G}'_0 \mathbf{V} \mathbf{G}_0 \end{aligned} \quad (2.19)$$

The result of Eq. (2.19) matches Eq. (2.12) and has been visualized in Fig. 2.5.

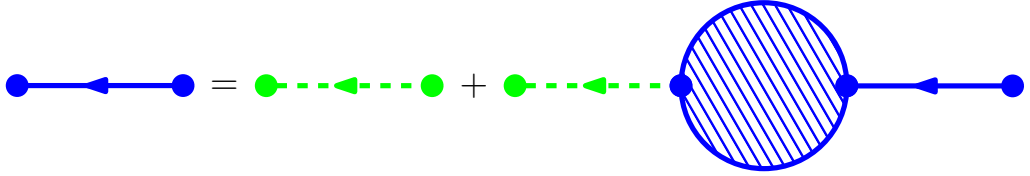


Figure 2.5: Iterative equation for noninteracting systems.

So far, only noninteracting systems with H_0 were treated. We include local Coulomb interaction by a red dotted line, which lets us draw the Hubbard interaction term H_1 from Eq. (2.14) in the shape of a vertex at site i (Fig. 2.6(a)) with two incoming and two outgoing propagators.

In contrast to the noninteracting system it is now difficult to obtain the interacting propagator $G_{i,j,\sigma}(i\omega_n)$ because any Green's function line $G_{0,i,j,\sigma}(i\omega_n)$ can be dressed by an arbitrary number of self-energy insertions of any order. An example of a 4th order contribution to the fully interacting Green's function is given in Fig. 2.6(b). This diagram is reducible as it can be divided by erasing a single propagator, leaving two irreducible self-energy parts. The part on the left has an additional self-energy insertion (a subgraph connected to the graph with two propagators) while the right graph is already a skeleton diagram, meaning it has no further self-energy insertions. Since the self-energy consists of an infinite number of such diagrams (two of them are given as an example in Fig. 2.6(c)), we chose the symbol given in Fig. 2.6(d) to depict the self-energy. With a similar argument as used in Eq. (2.19) one can calculate the fully interacting Green's function $G_{i,j,\sigma}$ by factoring out the 0th order G_0 term on the left and a following self-energy term, leaving Green's function terms with an arbitrary number of self-energy insertions on the left side. This leads to the Dyson equation (Fig. 2.7)

$$\mathbf{G} = \mathbf{G}_0 + \mathbf{G}_0 \Sigma \mathbf{G}. \quad (2.20)$$

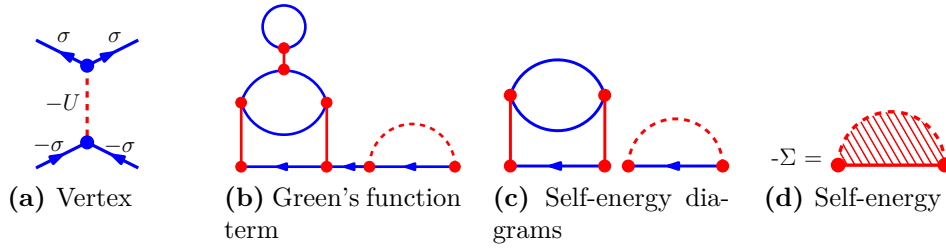


Figure 2.6: Diagrammatic approach to systems with Hubbard interaction.

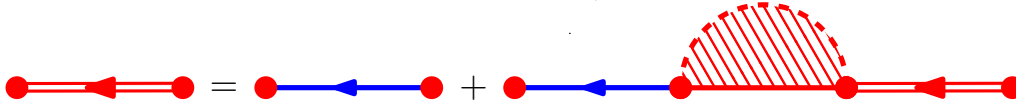


Figure 2.7: Dyson equation in diagrammatic language.

A detailed derivation of the whole diagrammatic approach is given in the textbooks of Abrikosov *et al.* [30] and Negele and Orland [31].

Figure 2.8 shows how the self-energy can be described as a functional of the interacting Green's function from Fig. 2.7. Here, only so-called fully dressed skeleton diagrams survive. This infinite summation leads to a final result for the exact Green's function of the interacting system,

$$\mathbf{G} = \frac{1}{\mathbf{G}_0^{-1} - \Sigma[\mathbf{G}]}, \quad (2.21)$$

which includes the functional $\Sigma[\mathbf{G}]$. This functional dependence is in general very difficult to evaluate, even for finite systems. Therefore, an obvious approach would be to switch the order in which the perturbations to H'_0 are treated. In contrast to Fig. 2.4 we first include Hubbard interaction to the noninteracting system of isolated clusters. This leads to the fully interacting cluster Green's function \mathbf{G}' , which has been introduced in Fig. 2.9 as a dashed and doubled red line. Luckily, this function can be evaluated by numerical exact methods, provided cluster sizes are sufficiently small. An infinite summation over all self-energy contributions to \mathbf{G}' can therefore be avoided. In a second step, Coulomb interaction is included as pictured in the second line of Fig. 2.9, which corresponds to Eq. (2.17) from Sec. 2.2.3.

In Fig. 2.9 only a special subclass of possible diagrams is included. The CPT therefore cannot be exact for finite Coulomb interaction U . Furthermore, the procedure is not self-consistent and studying spontaneous symmetry breaking is not possible.

CPT includes short-range interactions exactly within sufficiently large finite clus-

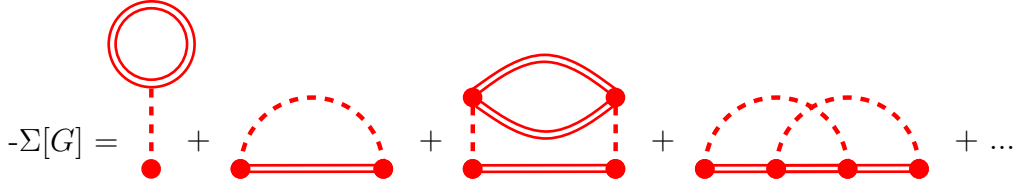


Figure 2.8: Functional dependence of the self-energy $\Sigma[G]$ in terms of fully dressed skeleton diagrams.

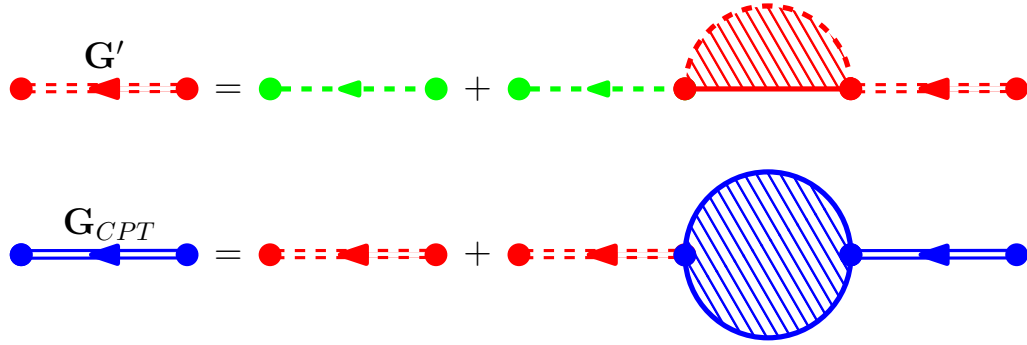


Figure 2.9: Diagrammatic description of the CPT via the cluster Green's function G' .

ters, while long-range interactions are at best treated on the mean-field level [12]. The method is therefore best suited for systems with medium to strong interactions.

The CPT equation can also be derived via a locator approach [32] or by inserting the self-energy of the reference system [11] by applying the Dyson equation

$$\Sigma'(i\omega_n) = \mathbf{G}'_0(i\omega_n)^{-1} - \mathbf{G}'(i\omega_n)^{-1} \quad (2.22)$$

and inserting this into Eq. (2.21). Hereby - as well as in the locator approach - the approximation has been made that the self-energy of the reference system $\Sigma'(i\omega_n)$ corresponds to the self-energy of the original system $\Sigma(i\omega_n)$.

2.3 Self-Energy-Functional Approach

The self-energy-functional approach (SFA) presented by Potthoff [13, 15, 33] uses the functional dependence $\Omega[\Sigma]$, which can be shown to be stationary at the physical self-energy Σ . This variational dependence can be evaluated exactly (without any approximation for the functional dependence, e.g., summing over lowest order contributions) on the subspace of an exactly solvable reference system. This procedure is selfconsistent and therefore yields results in the thermodynamic limit, allowing for example phase transitions and spontaneous symmetry breaking.

To construct the variational principle the Luttinger-Ward functional [34] $\Phi[\mathbf{G}]$ is used, which is defined as the sum over all closed, connected and fully dressed diagrams (Fig. 2.10). The functional derivative is given by

$$\frac{\delta\Phi[\mathbf{G}]}{\delta\mathbf{G}} = \frac{1}{\beta}\Sigma[\mathbf{G}], \quad (2.23)$$

which can be easily verified from Fig. 2.10, taking into account that the functional derivative leads to a removal of one fully interacting propagator, leaving a self-energy contribution.

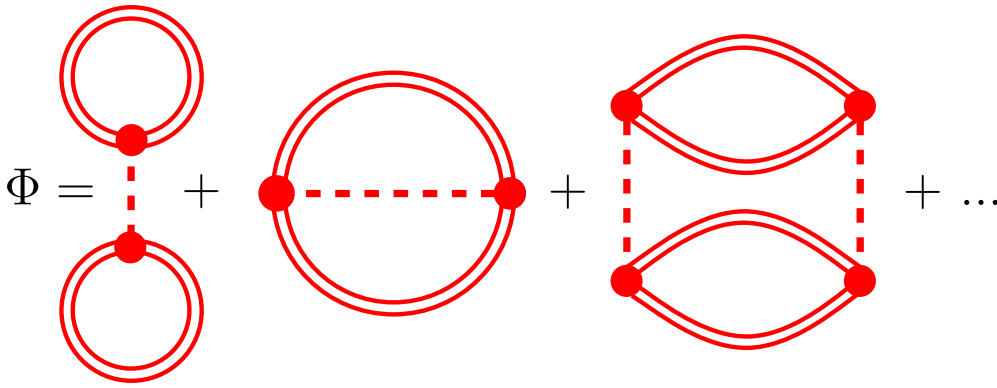


Figure 2.10: The lowest-order contributions to the Luttinger-Ward functional $\Phi[\mathbf{G}]$ in diagrammatic language. It is defined as the sum over all closed, connected and fully dressed diagrams.

With the help of the Luttinger-Ward functional we can define the grand potential $\Omega[\Sigma]$ as a functional of the self-energy

$$\Omega[\Sigma] = \text{Tr} \ln \frac{1}{\mathbf{G}_0^{-1} - \Sigma} + \Phi[\mathbf{G}[\Sigma]] - \text{Tr} (\Sigma \mathbf{G}[\Sigma]). \quad (2.24)$$

After applying a Legendre transformation $F[\Sigma] = \Phi[\mathbf{G}[\Sigma]] - \text{Tr} (\Sigma \mathbf{G}[\Sigma])$ one finds

$$\Omega[\Sigma] = \text{Tr} \ln \frac{1}{\mathbf{G}_0^{-1} - \Sigma} + F[\Sigma]. \quad (2.25)$$

By using

$$\frac{1}{T} \frac{\delta F[\Sigma]}{\delta \Sigma} = \mathbf{G}[\Sigma] \quad (2.26)$$

one sees that the stationary condition

$$\frac{\delta \Omega[\Sigma]}{\delta \Sigma} = 0 \quad (2.27)$$

is fulfilled exactly for $\mathbf{G}[\Sigma] = (\mathbf{G}_0^{-1} - \Sigma)^{-1}$, which recovers the Dyson equation (Eq. 2.20) [15]. The dynamical variational principle now consists of finding the physical self-energy, which will make the grand potential stationary (Eq. (2.24) together with Eq. (2.27)).

Still, the functional dependence $\Omega[\Sigma]$ is in general too complex to evaluate. Luckily, the Luttinger-Ward functional $\Phi[\mathbf{G}]$ does not depend on the single-particle part \mathbf{t} of the Hamiltonian but solely on the Coulomb repulsion U . Its Legendre transform $F[\Sigma]$ has the same property, which can be used to construct a subspace consisting of trial self-energies $\Sigma_{\mathbf{t}'}$, which depend on a set of kinetic parameters \mathbf{t}' . These parameters have to belong to exactly solvable subsystems with the same interaction part U as the reference system, such usually an alignment of identical, isolated clusters. For such a reference system one can again write

$$\Omega'[\Sigma] = \text{Tr} \ln \frac{1}{\mathbf{G}_0'^{-1} - \Sigma} + F[\Sigma], \quad (2.28)$$

where $F[\Sigma]$ stays the same as in Eq. (2.25) because it does not depend on \mathbf{t}' . With the help of Eq. (2.25) one can eliminate the unknown functional $F[\Sigma]$ and obtain

$$\Omega[\Sigma] = \Omega'[\Sigma] + \text{Tr} \ln \frac{1}{\mathbf{G}_0^{-1} - \Sigma} - \text{Tr} \ln \frac{1}{\mathbf{G}_0'^{-1} - \Sigma}, \quad (2.29)$$

with the still unknown functional $\Omega'[\Sigma]$. But this disadvantage can be lifted by inserting a trial self-energy of an exactly solvable reference system $\Sigma_{\mathbf{t}'}$. Now, the functional $\Omega'[\Sigma]$ reduces to the grand potential Ω' of the reference system, which can be numerically calculated.

An exact evaluation of $\Omega[\Sigma]$ is possible using

$$\Omega[\Sigma_{\mathbf{t}'}] = \Omega' + \text{Tr} \ln \frac{1}{\mathbf{G}_0^{-1} - \Sigma_{\mathbf{t}'}} - \text{Tr} \ln \mathbf{G}', \quad (2.30)$$

at least for trial self-energies from the subspace of exactly solvable reference systems which have to share the same interaction part with the original system. The quality of the result will of course depend on the subspace of the respective reference system.

2.4 Variational Cluster Approach

The previously described SFA can be used to improve the mechanism of CPT by removing the arbitrariness of the CPT construction concerning the intra-cluster one-particle operators by including the variational principle from Sec. 2.3. The VCA [8,

[13, 35, 36] works in the thermodynamic limit and therefore allows the investigation of spontaneous symmetry breaking, in contrast to CPT. In addition, the improved approach should be self-consistent and thermodynamical consistent.

Local interactions are treated accurately by ED of finite clusters while phases with long-range order are studied by the variational optimization of a fictitious symmetry-breaking field, where the dynamical information of an exactly solvable reference system is used. In contrast to CPT, the VCA has a self-consistent procedure included and works in the thermodynamic limit, which enables it to treat phase transitions. In contrast to static mean-field approaches, dynamic informations are used, allowing the observation of temporal correlations. Using ED allows an exact treatment of short-range correlations, which are neglected by methods based on DMFT or the recent density matrix embedding theory (DMET) [37, 38], which can solve the impurity problem with much lesser effort than in DMFT by taking the single-particle density matrix $\langle a_i^\dagger a_j \rangle$ as the quantum variable instead of the Green function in DMFT and using one bath site only. Reducing the numerical effort is also an argument for using the VCA as the number of bath sites is reduced in comparison to DMFT. In the cluster extension of DMFT (C-DMFT) Liebsch and Ishida found that the size of the bath can be reduced if more correlated sites are used [39]. This statement might hold also for the VCA, where the results may still be reasonable, even if no bath sites at all are included.

In the CPT the hopping parameter \mathbf{t} is taken as the original value from the infinite lattice, which has not necessarily to be a good choice. For example, CPT neglects some subclasses of self-energy diagrams describing inter-cluster scattering (see Fig. 2.9). An enhanced intra-cluster hopping could possibly compensate this shortcoming [13].

In the variational cluster approach a set of intra-cluster hoppings \mathbf{t}' is used to construct the corresponding trial self-energies. The interaction \mathbf{U} has to stay the same for all reference systems and cannot be optimized. For each parameter Eq. (2.29) is used to obtain $\Omega[\Sigma_{\mathbf{t}'}]$. Its optimum value $\Omega[\Sigma_{\mathbf{t}'_{\text{opt}}}]$ can then be determined at a stationary point of the grand potential functional:

$$\left. \frac{\delta \Omega[\Sigma_{\mathbf{t}'}]}{\delta \mathbf{t}'} \right|_{\mathbf{t}'=\mathbf{t}'_{\text{opt}}} = 0. \quad (2.31)$$

CPT is generalized by optimizing its starting point, which has been presented in Sec.

2.2.3. Based on equations (2.14), (2.15) and (2.16) one can add *any* local single-particle term Δ to the intracluster part H'_0 . In order to retain the Hamiltonian (Eq. (2.14)), Δ has to be subtracted from the intercluster part V , which leads to the transformation

$$H'_{0,m} \rightarrow H'_{0,m} + \Delta_m, \quad (2.32)$$

$$V_{m,n} \rightarrow V_{m,n} - \delta_{m,n} \Delta_m, \quad (2.33)$$

where m, n denote the cluster position.

The arbitrary single particle operator in general has the form

$$\Delta_m = \sum_{a,b} \Delta_{a,b} c_{m,a}^\dagger c_{m,b}. \quad (2.34)$$

Δ can not only be a hopping parameter but also a fictitious symmetry breaking field term, like a staggered magnetic field [36].

In the noninteracting case (see chapter 2.2.2) the result does not depend on Δ , while in the interacting case it does. This can be used to optimize $\Omega(\Delta)$ with the help of SFT on the restricted subspace of trial self-energies because the general functional dependence $\Omega[\mathbf{G}(\Delta)]$ is not unique and no variational principle is valid for that case. A variation of Δ leads to a change in the noninteracting part H'_0 , while the interaction part is fixed. Cluster solvers allow a calculation of the self-energy $\Sigma(\Delta)$, the cluster Green's function $\mathbf{G}'(\Delta)$ and the grand potential $\Omega'(\Delta)$ of the respective reference system. Using the SFA, one retains in analogy to Eq. (2.30)

$$\begin{aligned} \Omega(\Delta) = & \Omega'(\Delta) + T \sum_n \sum_{\mathbf{Q}} \text{Tr} \ln \frac{-1}{\mathbf{G}_{0,\mathbf{Q}}(i\omega_n)^{-1} - \Sigma(\Delta, i\omega_n)} \\ & - N_{\text{cl}} T \sum_n \text{Tr} \ln (-\mathbf{G}'(\Delta, i\omega_n)), \end{aligned} \quad (2.35)$$

where N_{cl} is the number of clusters.

The VCA offers a number of advantages: It is an entirely nonperturbative approach because no diagrammatic series has ever been cutted and no subclass has been neglected. Also, it is a thermodynamical consistent approach and the quality of the result is scalable via the cluster size L_c . For $L_c \rightarrow \infty$ the result converges towards the exact solution. Of course, ED as the cluster solver will never allow large clusters as the effort increases exponentially with system size. On the other hand, finite

size effects and effects from the cluster geometry might play an important role, so different cluster sizes should always been applied as a check of consistency. Like all cluster mean-field approximations, also the VCA is not capable of describing non-local two-particle correlations.

Several variational parameters are suggested by Potthoff [13]: To ensure thermodynamical consistency, one should always include terms that shift the level of the on-site energies, for example a chemical potential. Of course, in the case magnetic systems a corresponding Weiss field should be included and optimized. The space of variational parameters can additionally be increased by the insertion of fictitious, noninteracting ($U = 0$) *bath sites*, which are coupled via additional hopping terms to the cluster. These sites do not change the interaction part H_1 , but they might locally increase the quality of the approximation, while increasing the cluster size might improve nonlocal correlations as well.

2.5 Cluster Solvers

One general problem of cluster theories lies in solving the actual cluster problem. While for exact methods the effort increases exponentially with cluster size, perturbative approaches suffer from dynamical changes of low-energy many-body excitations, which complicates the setting of an energy scale.

In contrast to the problem of an isolated cluster, quantum cluster theories have to take care of additional bath degrees of freedom which couple the cluster to an effective medium. The simplest solution for such a problem was found 1961 by Anderson with the Anderson impurity model [40]. The quality of new approaches can basically be judged by comparing it to the well-understood physics of the Anderson model. But this comparison gets difficult when the complexity of the system gets to large. As a conclusion, any obtained result should carefully be checked for consistency.

A big problem of weak-coupling approaches like the fluctuation-exchange approximation (FLEX) [41–43] is the inability to describe effects originating from strong-coupling mechanisms, like the opening of a Mott gap, even if it is embedded in a quantum cluster method. In contrast to perturbative approaches like FLEX or the noncrossing approximation [44, 45], nonperturbative methods yield numerically exact results at the expense of numerical effort, which increases exponentially with cluster size. A realization with a simple code that allows relatively large cluster

sizes is the quantum Monte Carlo (QMC) method. Beside the large numerical effort needed, another shortcoming of QMC is the sign problem.

Another nonperturbative approach is Wilson’s numerical renormalization group [46–49], which treats small energy scales with exceptional accuracy and is in principal not limited in the parameter space. Limitations include shortcomings in describing features with higher energies.

In this work, Lanczos’ exact diagonalization [27, 50] has been used to calculate the properties of the reference clusters. A conventional diagonalization is impossible due to matrix sizes reaching into millions. ED is a wave-function based method at zero temperature, that uses a small set of l orthonormal states, where l denotes the number of states taken to discretize the bath degrees of freedom [51–53]. With a basis in this subspace it is possible to determine the lowest-lying eigenstates and the cluster self-energy [54]. ED is still limited to modest-size clusters and because of finite precision vectors lose their orthogonality. As a result, only the ground state can be numerically accurately calculated. While the calculated ground state is practically exact, its Green function may suffer from the re-orthonormalization problem in some cases. Especially higher states in energy exhibit this behavior more often. Generally, Green functions converge very fast within ED, despite exhibiting high frequencies. In [55] it is argued, that ED in fact works out very well on short time scales, which corresponds to high frequencies. Due to this fast convergence, no re-orthonormalization is needed in general, but this procedure can of course be included, which is of course only feasible for small to modest-size clusters.

2.5.1 Cluster Geometry

Due to the severe limitation of ED cluster sizes are limited to small values. Inevitably, finite size effects occur, which are not well understood in the case of advanced cluster methods like CPT, the VCA or C-DMFT. From DCA-studies it is known the lattice point symmetry and the configuration of nearest neighbors should be comparable to the one of the original lattice [32, 56, 57]. A recent CPT study on the honeycomb lattice [58] also presented tiling-dependent effects of the quasiparticle band structure. Only in the case of a 6-site cluster, which preserves the point group symmetry of the honeycomb lattice, the right quasi-particle band structure can be retrieved.

Also the symmetry of the order parameter should be taken care of. For example, antiferromagnetic order requires a bipartite cluster, which limits the choice of the cluster shape additionally.

2.5.2 Limiting Cases

The cluster methods presented here (CPT, C-DMFT and the VCA) become exact in the weak-coupling limit because the cluster self-energy Σ' vanishes. In this case, the solution is given by the noninteracting Green's function. Also the strong-coupling limit leads to exact results because lattice sites decouple and a single-site problem is left, which can be solved easily by the Green's function of an isolated site.

In the formal case of infinite large clusters $N_{\text{cl}} \rightarrow \infty$, the original problem is recovered and the cluster Green's function solves the problem exactly. For a cluster size of $N_{\text{cl}} = 1$, DCA and C-DMFT recover DMFT, while CPT reduces to the Hubbard-I approximation [18]. Following [32], quantum cluster theories can thus be seen as an interpolation between the exact result for an infinite cluster size and the Hubbard-I approximation or the DMFT at $N_{\text{cl}} = 1$, respectively.

3 Superconductivity and Magnetic Ordering on Triangular Lattices

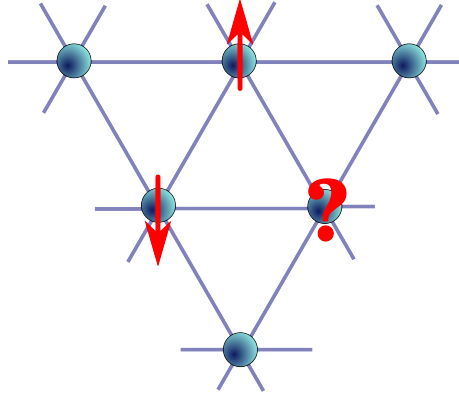


Figure 3.1: Classical problem of spatial frustration on the triangular lattice with antiferromagnetic couplings.

The triangular lattice provides a simple model system to study frustration effects of correlated electrons. Due to its geometry, already nearest-neighbor antiferromagnetic interactions cause geometric frustration effects, as shown in Fig. 3.1. The classical solution for local Heisenberg spins is given in Fig. 3.2. Here, the local spins order in a coplanar but noncollinear structure while forming angles of 120° .

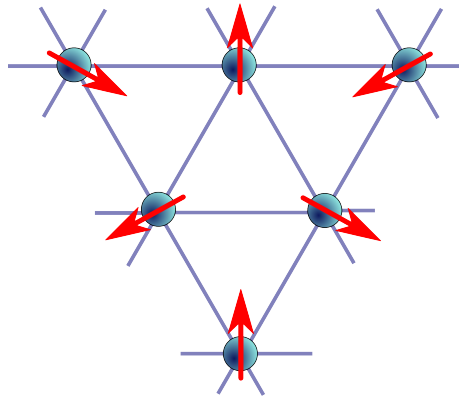


Figure 3.2: One possible 120° coplanar solution for local Heisenberg spins on a triangular lattice.

But this classical solution is by far not the only possible phase on the triangular lattice. Following the general rule that electronic interactions on low dimensional systems cause ‘interesting’ phase diagrams, we see a variety of phases develop if we do not restrict ourselves to Heisenberg spins but allow itinerant fermions. The formation of these phases depends on various parameters such as on-site repulsion, the filling of the lattice, and the shape and strength of the coupling parameters. Also, the model and the method used might impact the results due to shortcomings or overestimations of the respective method. For example, itinerant and local degrees of freedom are separated within the Kondo lattice model, while they originate from the same electrons within the Hubbard model.

Using CPT (see Sec. 2.2) and its variational extension VCA (Sec. 2.4) allows a treatment the system beyond mean-field level. CPT and VCA should give the best results in the regime of moderate to strong couplings, where correlation effects are mainly located within the cluster.

In the following sections, an introduction of the problem will be given (Sec. 3.1), followed by a description of other methods and stable phases found (Sec. 3.2). Some details concerning the methodology will be given in Sec. 3.3. After the presentation of the results achieved with VCA in Sec. 3.4, effects that might have affected the calculations will be discussed in Sec. 3.4.7.

3.1 Introduction

Besides intrinsic geometric frustration, triangular lattices exhibit interesting electronic properties. Their density of states (DOS) diverges at $3/4$ filling forming a van Hove singularity (Fig. 3.3). At this van Hove filling of 1.5 electrons per site the formation of ordered phases is enhanced and additionally supported by a perfectly nested Fermi surface (Fig. 3.5(b) for $n = 1.5$). The Fermi surface forms a perfect hexagon inside the hexagon of the Brillouin zone of the lattice by connecting the three inequivalent M_i points by three different nesting vectors \mathbf{Q}_i (Fig. 3.5(d)), which are half the size of the reciprocal lattice vector:

$$\mathbf{Q}_1 = \left(0, \frac{2\pi}{\sqrt{3}}\right), \quad (3.1)$$

$$\mathbf{Q}_2 = \left(\pi, \frac{\pi}{\sqrt{3}}\right), \quad (3.2)$$

$$\mathbf{Q}_3 = \left(\pi, -\frac{\pi}{\sqrt{3}}\right) \quad (3.3)$$

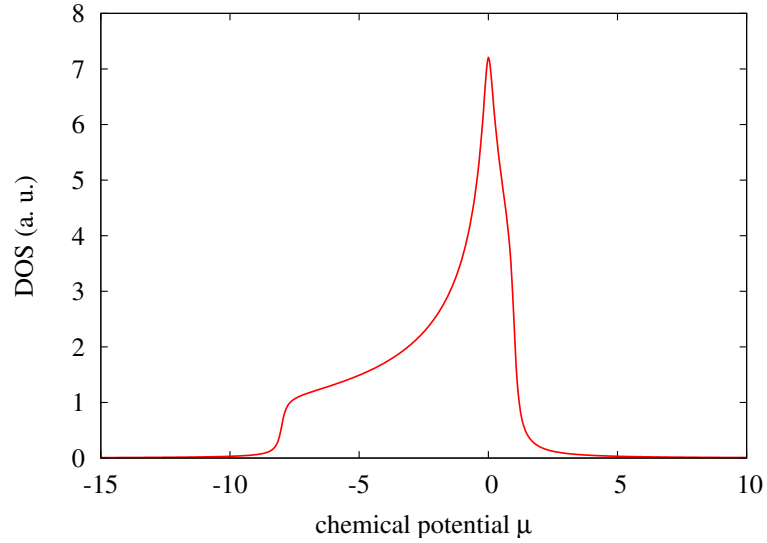


Figure 3.3: Density of states for the noninteracting triangular lattice. The chemical potential is chosen corresponding to $3/4$ filling, pushing the Fermi energy to the van Hove singularity.

For the honeycomb lattice a similar situation occurs at a filling fraction of $5/8$, as has been shown in Fig 3.4. Here, one finds van Hove singularities in the DOS for fillings of $3/8$ and $5/8$ but only at the filling of $5/8$ the Fermi surface is perfectly nested and corresponds to the hexagonal Fermi surface shown in Fig. 3.5(b) [60, 61]. Because the triangular and the honeycomb lattice share the same Fermi surface in the respective filling regime, similar ordering effects should be expected.

3.2 Candidates for Stable Phases

3.2.1 Magnetically Ordered Phases

Martin and Batista proposed a noncoplanar state for the triangular lattice [62] with unusual transport [63] and magnetoelectric [64] properties. For example, a noncoplanar spin alignment can lead to a nonzero scalar spin chirality $\langle \mathbf{S}_i \cdot (\mathbf{S}_j \times \mathbf{S}_k) \rangle \neq 0$,

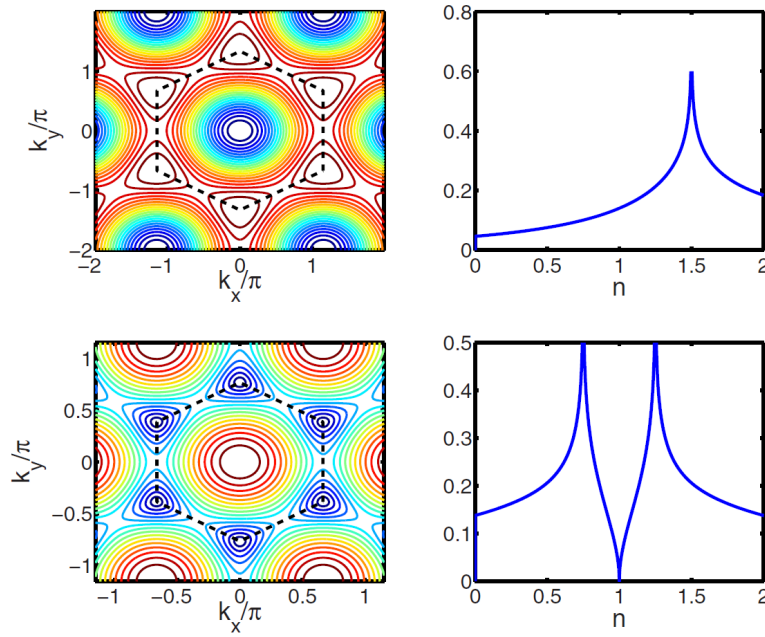


Figure 3.4: Lines of constant energy (left) and density of states (right) for the triangular lattice (top) and for the honeycomb lattice (bottom). Picture taken from [59].

where \mathbf{S}_i is the magnetic moment at site i . This spin chirality breaks time-reversal and parity symmetry. A spontaneous quantum Hall effect without an external magnetic field may occur and, if a full gap is opened by the spin structure, the system may become a spontaneous quantum Hall insulator [63] because the electronic wave function obtains a Berry Phase through the exchange interaction between the local moments and the spins of the conduction electrons. Indications of such an anomalous Hall effect have been found also in an experiment by Ueland *et al.* [65] in the highly correlated metal UCu_5 .

Batista and Martin [62] found the noncoplanar phase from Fig. 3.6 to appear as a weak-coupling instability at $3/4$ filling in the Kondo lattice and Hubbard model. Here, the three different ordering vectors \mathbf{Q}_i perfectly nest the Fermi surface (see Fig. 3.5(d)), supporting four-sublattice ordered phases. In principle, a variety of $3q$ ordered states, such as collinear, coplanar and noncoplanar, are possible and unfortunately, while coplanar (noncollinear) states are not favored, noncoplanar and collinear phases are very close in energy on the mean-field level, making a distinction impossible.

Chern and Batista [66] found another $3q$ ordered state, shown in Fig. 3.7. It exhibits a collinear spin order with nonuniform spin moments. This state cannot be

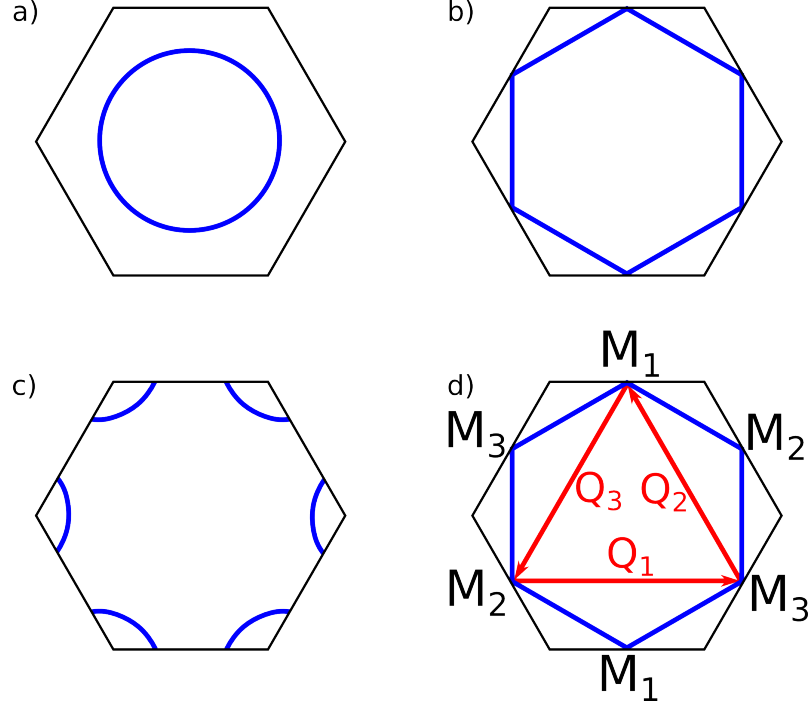


Figure 3.5: Fermi surfaces of the noninteracting triangular lattice at different fillings reaching from $n \approx 0.65$ (a) over $n = 1.5$ (b) to $n \approx 1.8$ (c). The perfectly nested Fermi surface at $n = 1.5$ is shown in (d), where the nesting vectors \mathbf{Q}_i connect the three inequivalent points M_i .

addressed by starting with a model of local moments of fixed length. A model with itinerant fermions is required to obtain this particular spin-density-wave state, which may be a reason that this state was missed in former publications. The SDW phase pictured in Fig. 3.7 is the first example of an emerging quadratic Fermi point with nonzero winding number ($n = \pm 2$). They state that the noncoplanar phase from Fig. 3.6 always wins over any collinear $3q$ -ordered state because the chiral phase lowers its energy by creating a full gap due to the spontaneous quantum Hall effect, while in the collinear phase only one spin branch in the electronic excitation spectrum is gapped and the other one allows gapless excitations (see Fig. 3.8(a)). Since the Fermi surface exists only for one spin branch while the other is gapped out, the collinear state may be called a ‘half metal’. Its properties may be interesting for nano-science applications as they allow the electrical control of spin currents [60].

Using Ginzburg-Landau theory, Chern and Batista found a low-energy mean-field

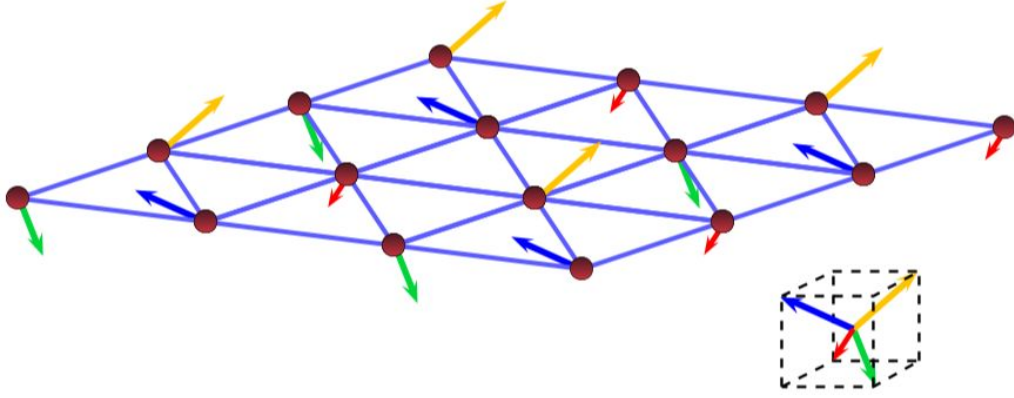


Figure 3.6: Four-sublattice chiral spin ordering on the triangular lattice. The local moments point towards the corners of a regular tetrahedron.

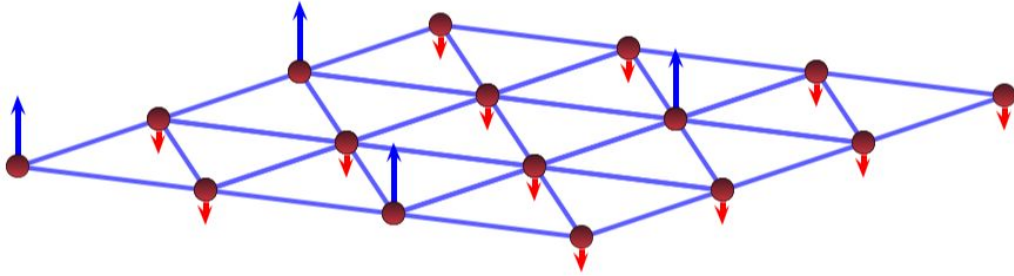


Figure 3.7: Four-sublattice collinear spin ordered state with nonuniform spin moments. The quadrupled unit cell contains one large spin moment of $3\mathbf{S}$ (blue) and three small spin moments with $-\mathbf{S}$ (red).

Hamiltonian for the collinear state [66],

$$H_{\text{MF}} = \frac{1}{\nu'} \int d\mathbf{r} \sum_{\eta} |\mathbf{m}_{\eta}|^2 + \sum_{\mathbf{k}} \Psi_{\mathbf{k}}^{\dagger} \mathcal{H}(\mathbf{k}) \Psi_{\mathbf{k}} + \int d\mathbf{r} \Psi^{\dagger}(\mathbf{r}) \left[\frac{1}{\sqrt{6}\Delta} (Q_1 \tau^z + Q_2 \tau^x) + \frac{\kappa}{\sqrt{3}\Delta^2} \tau^y \right] \Psi(\mathbf{r}), \quad (3.4)$$

with the effective inverse coupling $1/\nu'$, the three order parameters $\Delta_{\eta} = \Delta \mathbf{z}$ and their small deviations perpendicular to the \mathbf{z} -direction \mathbf{m}_{η} , the low energy doublet manifold $\Psi = (\Psi_1, \Psi_2)$, the doublet order parameter (Q_1, Q_2) and the pseudospin τ .

The minimization of Eq. (3.4) shows two minima of the order parameter κ , which can be identified with the scalar spin chirality. The solution for $\kappa = 0$ yields the collinear SDW state, whereas a solution with finite κ denotes the chiral phase. The energy of the latter is always lower than the energy of the collinear state but at higher temperatures the system may rest in this state and undergo a discontinuous

transition into the noncoplanar phase at low temperatures.

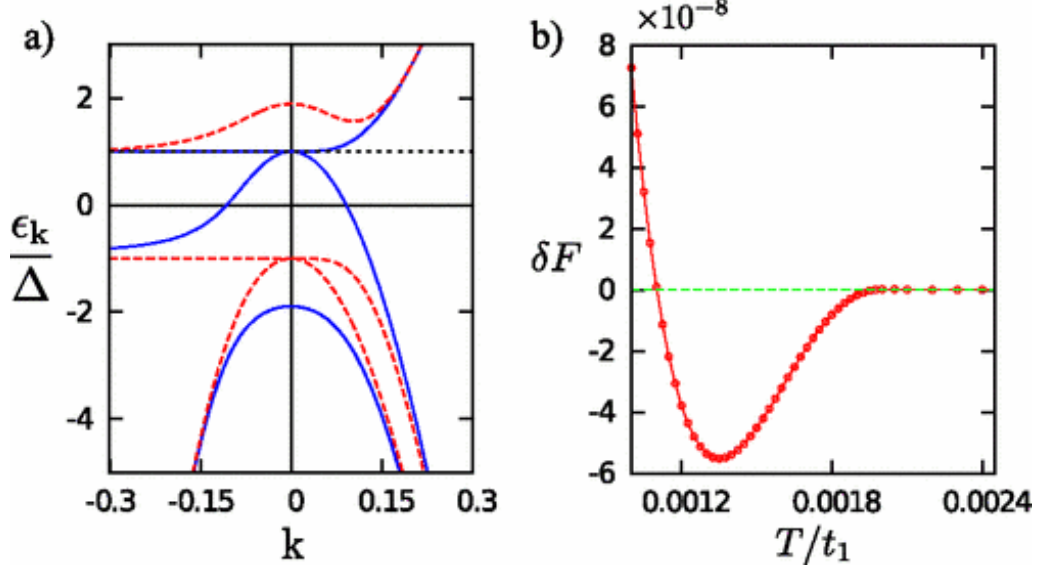


Figure 3.8: a) Spin-dependent excitation spectrum of the 3q-collinear SDW-state at an M -point along the Fermi surface (negative k) and along the Brillouin zone boundary (positive k). Excitations with spin projection along the order parameter are printed in red (dashed) and the spin-down branch is printed in blue. b) Difference in the free energy between the collinear and the chiral state. Picture taken from [60].

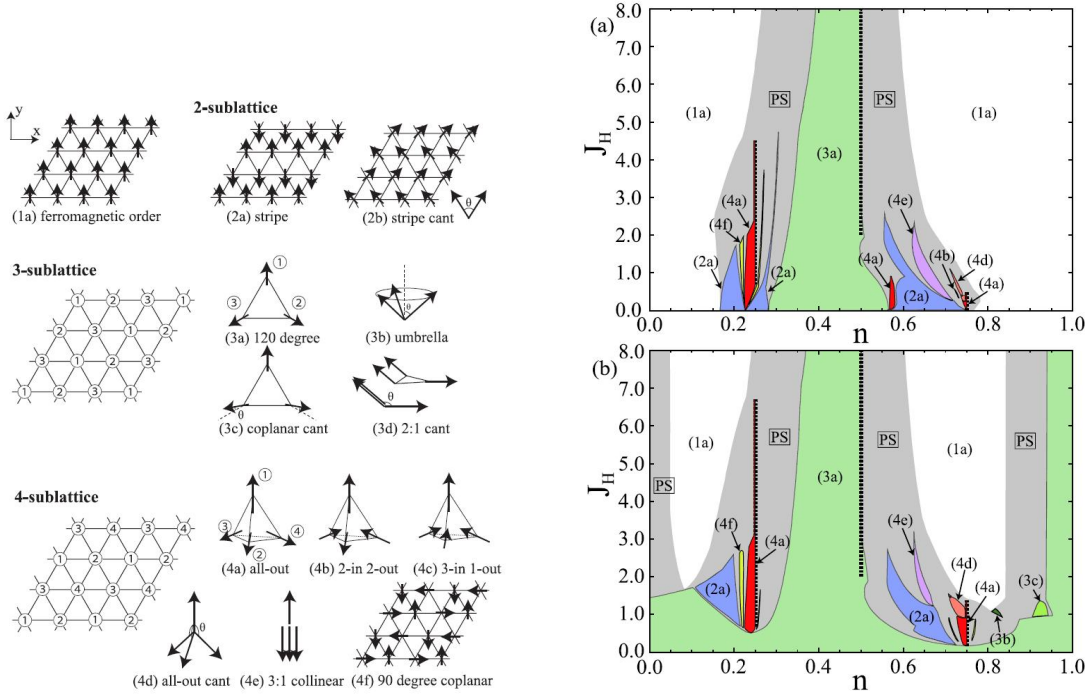
In a publication by Nandkishore *et al.* [60] the 3q-collinear SDW-state wins over the noncoplanar state in a wide temperature regime, as can be seen by the comparison of the respective free energy in Fig. 3.8(b). Towards zero temperature, the chiral state wins again with the same argument as in [66], namely that a full gap in the excitation spectrum is opened. Here, the free energies have been calculated within Ginzburg-Landau theory.

Akagi *et al.* performed a variety of studies on the triangular lattice using the Kondo lattice model [67–69]. The Hamiltonian of the Kondo lattice model is given by

$$\mathcal{H} = -t \sum_{\langle i,j \rangle, \alpha} \left(c_{i,\alpha}^\dagger c_{j,\alpha} + \text{h.c.} \right) - J_H \sum_{i,\alpha,\beta} c_{i,\alpha}^\dagger \boldsymbol{\sigma}_{\alpha,\beta} c_{i,\beta} \cdot \mathbf{S}_i + J_K \sum_{\langle i,j \rangle} \mathbf{S}_i \cdot \mathbf{S}_j, \quad (3.5)$$

where $c_{i,\alpha}^\dagger$ ($c_{i,\alpha}$) are the creation (annihilation) operators for conduction electrons with spin α on site i , J_H is the Hund’s rule coupling, $\boldsymbol{\sigma}_{\alpha,\beta}$ a vector of the Pauli spin matrices and \mathbf{S}_i is a classical localized spin on site i . For $J_K \neq 0$, a superexchange

between localized spins is taken into account.



(a) Ordering patterns of localized spins compared by Akagi *et al.* in variational calculations. Phase (3a) is the classical solution while phase (4a) equals the chiral state from Fig. 3.6, that exhibits an anomalous Hall effect. Picture taken from [67].

(b) Phase diagram of the ground-states for $J_K = 0$ (top) and $J_K = 0.01$ (bottom). Vertical dashed lines indicate gapful solutions and PS indicates areas of phase separation. Picture taken from [67].

Figure 3.9: Results for the Kondo lattice model by Akagi *et al.* several phases with localized spins with

In [67], the stability of 13 different ordered states with local spins were compared (see Fig. 3.9(a)) by a calculation of the ground-state energies and a variational calculation. The results are given in Fig. 3.9(b). It can be seen, that the previously proposed chiral state is indeed supported at $3/4$ filling, and - to large surprise - also at $1/4$ filling. The state at $1/4$ filling has indeed the same properties as the state at $3/4$ filling, e.g. the opening of a gap due to spontaneous quantum Hall effect, but it has a different origin because the its Fermi surface is almost circular and not perfectly nested as the one at $3/4$ filling. Interestingly, a finite superexchange interaction (lower figure of Fig. 3.9(b)) further stabilizes both chiral phases. Additional spin-charge ordered phases with collinear and noncollinear alignments of the local moments and larger unit cells than shown in Fig. 3.9(a) have been found in a recent study by Deja *et al.* [70] to develop at electronic fillings of one third and two thirds.

The chiral phase at $1/4$ filling is stabilized by a positive biquadratic interaction arising from perturbation theory up to fourth order in terms of the spin-charge coupling [68]. The critical enhancement of the biquadratic interaction signals an instability towards a chiral phase near $1/4$ filling and has its origin by the formation of ordering wave vectors, which connect the Fermi surface. Additionally, the chiral phase at $1/4$ filling seems to be robust against quantum spin fluctuations [69], whereas the phase at $3/4$ filling is destabilized by quantum fluctuations.

The tendency of quantum fluctuations to destabilize chiral magnetic ordering within the picture of localized spins collides with the energetic preference of the chiral state by the formation of a gap for itinerant electrons. The effects of quantum fluctuations have also been studied within the Heisenberg model with nearest and next-nearest neighbor interactions [71], with the result that the classical degeneracy of collinear and chiral phases is lifted by fluctuations, preferring collinear phases. Whether these quantum fluctuations will also be present in the Hubbard model is to be studied in this thesis, where they will compete with the mechanism of the spontaneous quantum Hall effect, forming a gap for the chiral state.

So far, the discussion of the stability of SDW states in [60] does not take into account the possibility of superconductivity. The mean-field decoupling used to construct the Kondo lattice model out of the Hubbard model is performed using density-like operators and not pairing operators. In the following section, properties of possible superconducting phases will be presented.

3.2.2 Superconducting Phases

A temperature flow renormalization group (RG) analysis by Honerkamp [72] studied the RG flow for a one-band Hubbard model on the triangular lattice at weak to medium electron-electron interactions (values of the Coulomb repulsion U reaching from $3t$ to $4t$). The method used was a \mathbf{k} -space resolved N -patch RG that covers the full Fermi surface [73]. No low-energy cutoff is induced in the temperature-flow RG scheme, where the temperature T itself is used as flow parameter, which allows an unbiased comparison between FM and AFM tendencies [72].

At the van Hove singularity, a RG flow to strong coupling has been found for purely local Coulomb interactions. The spin susceptibility diverges at the three nesting vectors of the hexagonal Fermi surface \mathbf{Q}_n , indicating magnetic ordering at these

three vectors. Unfortunately, no statement could be made whether the system orders at a superposition of the three wave vectors, only one of the wave vectors or whether ordering occurs at all.

Slightly away from $3/4$ filling (± 0.03 around the van Hove filling of 1.50 for $U = 4$), a cut-off of the SDW channel leads to a singlet-pairing channel becoming the dominant instability. This singlet-pairing channel has a f -wave symmetry, where the gap function $\Delta(\theta) \propto \sin(6\theta)$, with 12 nodes while θ moves around the Fermi surface.

Another more recent renormalization group analysis by Nandkishore *et al.* [61] on doped graphene monolayers found chiral superconductivity to be dominant if the system is doped to the van Hove singularity. This chiral superconducting phase has $d_{x^2-y^2} + id_{xy}$ (short ‘ $d + id$ ’) gap structure with a phase change of multiples of 2π while winding around the Fermi surface, breaking time reversal symmetry (TRS). Usually, interactions favor either $d_{x^2-y^2}$ or d_{xy} pairing due to a strong momentum dependence. However, in triangular and honeycomb lattices both pairing channels are degenerate by symmetry, allowing a superposition of both [74]. Such a superposition of order parameters with nodes at different values in reciprocal space should be energetically preferred because the superposition opens a complete gap without any nodes.

Of course, if repulsive interactions are applied, superconductivity has to compete with SDW and charge density wave (CDW) instabilities. At first sight, repulsive interactions might favor density wave orders, but renormalizations on the susceptibilities to the different phases have to be taken into account. A patch renormalization group around the saddle points, which dominate the DOS, was performed in [61], finding a suppression of the CDW vertex, but an enhancement of the SDW vertex. But chiral $d + id$ superconductivity diverges even faster at the van Hove point, making it the leading order. Also, away from perfect nesting the spin channel diverges more slowly than the superconducting channel. Additionally, a suppression of the s -wave channel has been found, making chiral d -wave superconductivity the leading instability for all values of filling. This statement of course only holds within the validity of RG, which is for weak interactions.

Because the properties of graphene at the van Hove point at $5/8$ -filling (divergent DOS and perfectly nested, hexagonal shaped Fermi surface) correspond to the situation in the triangular lattice at the van Hove point for $3/4$ filling, the results of [61]

should also be applicable for the triangular lattice, although the honeycomb lattice of graphene lacks geometric frustration.

An additional evaluation of a Ginzburg-Landau functional [75] that includes both order parameters of chiral d -wave superconductivity and collinear SDW revealed that the ordering temperature T_N of the SDW phase is slightly lower than the critical temperature of superconductivity T_c at the van Hove point of graphene, indicating that these two phases are mutually exclusive. Since the symmetry groups of the ordered phases do not match each other, a second order transition is forbidden. Therefore, the phases are separated by a first order transition.

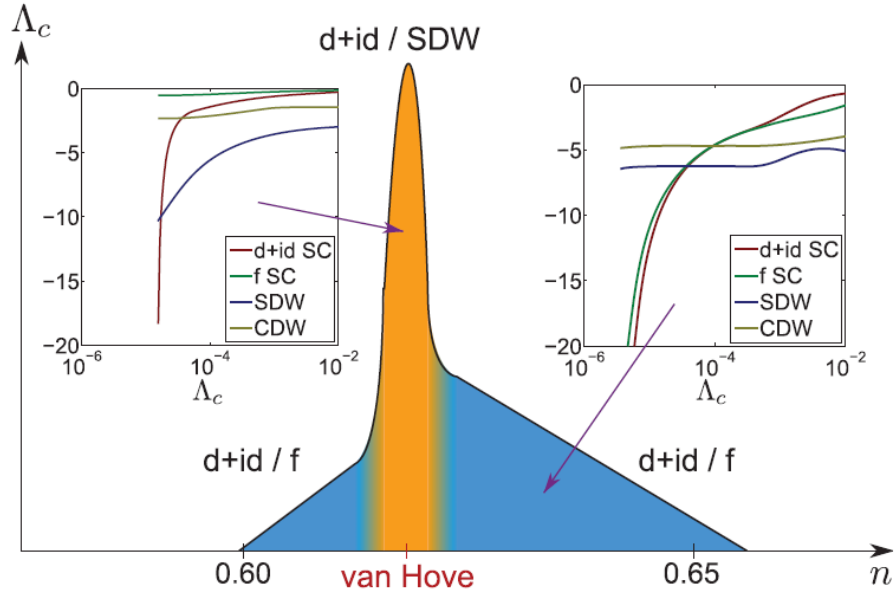


Figure 3.10: Possible phase diagram for graphene from functional RG [76]. $d + id$ SC is found to be the leading instability at the van Hove point for realistic parameters. Whether $d + id$ or f -wave SC develops away from the van Hove singularity depends on the long range of the Hubbard repulsion. Picture taken from [76].

Kiesel *et al.* performed a functional RG method to compare competing many-body instabilities at and around the van Hove singularity of graphene. They found a rich phase diagram (see Fig. 3.10), where the results depend on the long rangedness of the Coulomb repulsion U and the hopping t . They applied a tight-binding model up to third nearest neighbor hopping,

$$H_0 = \left[t_1 \sum_{\langle i,j \rangle, \sigma} c_{i,\sigma}^\dagger c_{j,\sigma} + t_2 \sum_{\langle\langle i,j \rangle\rangle, \sigma} c_{i,\sigma}^\dagger c_{j,\sigma} + t_3 \sum_{\langle\langle\langle i,j \rangle\rangle\rangle, \sigma} c_{i,\sigma}^\dagger c_{j,\sigma} + \text{H.c.} \right] - \mu n, \quad (3.6)$$

and a long-range Hubbard interaction

$$H_{\text{int}} = U_0 \sum_i n_{i,\uparrow} n_{i,\downarrow} + \frac{1}{2} U_1 \sum_{\langle i,j \rangle, \sigma, \sigma'} n_{i,\sigma} n_{j,\sigma'} + \frac{1}{2} U_2 \sum_{\langle\langle i,j \rangle\rangle, \sigma, \sigma'} n_{i,\sigma} n_{j,\sigma'}. \quad (3.7)$$

Using realistic values for the hopping parameters of graphene ($t_1 = 2.8$, $t_2 = 0.1$ and $t_3 = 0.07$ eV [77]), the $d + id$ instability is dominant for $U_0 = 10$ eV. However, the SDW becomes dominant if the on-site repulsion is increased up to $U_0 = 18$ eV. Decreasing longer-ranged hopping stabilizes SDW fluctuations in the nesting channel. SDW therefore becomes the leading order already at $U_0 = 8.5$ eV if only nearest neighbor interactions are included. Away from the van Hove singularity, SDW fluctuations are weakened and the $d + id$ SC state may win, depending on the long range of the Coulomb repulsion. For long-range Coulomb interactions, also CDW fluctuations play a role as they might push the system towards a triplet f -wave superconducting state.

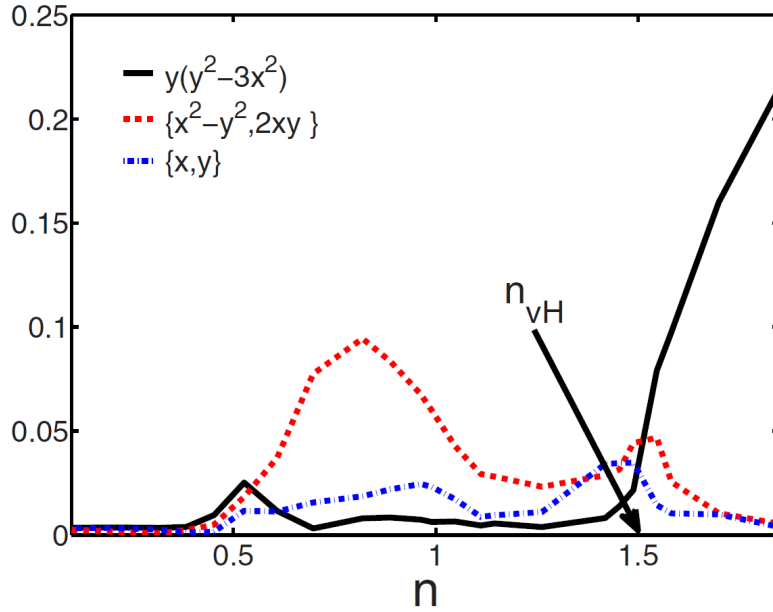


Figure 3.11: Pairing strength as a function of filling n for different superconducting order parameters. The superposition of $d_{x^2-y^2}$ and d_{xy} (dotted red line) is dominating the hole-doped regime whereas triplet f -wave superconductivity (straight black line) is the leading instability at dopings beyond van Hove filling. Picture taken from [59].

A different picture was found by Daghu *et al.* [59], where a RG analysis was applied to a variety of lattice structures within the Hubbard model in the weak-coupling regime. A comparison of the coupling strengths of s -wave, d -wave and f -wave superconducting order parameters (see Fig. 3.11) revealed a superposition of $d_{x^2-y^2}$ and d_{xy} -wave pairing to be the dominant instability in a wide hole doping regime.

At dopings beyond $3/4$ filling f -wave superconductivity becomes the dominant order parameter, which can be explained by symmetry arguments. The Fermi surface at fillings beyond van Hove filling is separated into six disjoint pockets which are situated at the corners of the Brillouin zone and which are symmetric under a rotation of $\pi/3$. An order parameter with f -wave symmetry can be placed within the Brillouin zone in such a way that its nodes are situated exactly between these pockets. These nodal lines do not cross the disjoint Fermi surface and therefore a fully gapped state can be observed where the gap changes its sign between neighboring Fermi surface pockets.

Precisely at the van Hove point, both $d + id$ and f -wave pairing strengths are almost equal, which prevents a determination of the leading instability. Additionally, only pairing channels have been studied in [59], leaving out possible flows towards SDW-phases.

Recently, Nandkishore *et al.* also tried to access the strong-coupling regime with a parquet RG analysis [78]. Taking the full Fermi surface into account, the leading instability remains chiral d -wave superconductivity at the van Hove point, like previous patch RG studies predicted [59, 61]. Hereby, d -wave superconductivity is also the leading instability at the edges of the Fermi surface. Towards strong interactions, the results have to be treated with caution as the RG procedure is no longer controlled. Performing a patch RG analysis the two leading instabilities are towards d -wave superconductivity and - surprisingly - ferromagnetism, although it might be destabilized by effects of edge Fermions. SDW phases might become the leading instability only if the the RG flow is stopped at an intermediate energy scale.

While superconductivity at the van Hove point arises for all choices of bare interactions $U(r)$ in [78], Nandkishore *et al.* claim that superconductivity at generic fillings is a threshold phenomenon that occurs only if the interaction $U(r)$ is large enough. The appearance of superconductivity in the weak-coupling regime despite bare repulsive Coulomb interaction is known as the Kohn-Luttinger formalism [79, 80], which describes instability towards superconductivity in systems where the long-range oscillatory tail of a screened Coulomb potential becomes over-screened and attractive at large distances [81].

For Kohn-Luttinger superconductivity studied in [78], a long-range Coulomb interaction $U(r)$ up to next nearest neighbors is needed to stabilize d -wave and f -wave

superconductivity. Additionally, the attraction from the Kohn-Luttinger mechanism has to be large enough to exceed the bare interaction for superconductivity to develop, while superconductivity at the van Hove point arises at arbitrary weak interactions. At generic fillings, Nandkishore *et al.* [78] find *f*-wave superconductivity to be the most likely scenario. For pure local on-site Hubbard repulsion, only *s*-wave channels exhibit a nonvanishing interaction.

Jiang *et al.* combined ED, density matrix renormalization group and the variational Monte Carlo method on finite size systems on the honeycomb lattice within the Hubbard model and the $t - J$ model [82]. Their results showed that either a chiral SDW phase or a new phase, denoted as spin-charge-Chern liquid (SSCL), is supported at van Hove filling within the Hubbard model over a wide physical parameter regime $1 < U/t < 40$ and between $0.1 < J/t < 0.8$ within the $t - J$ model. Beyond $J/t = 0.8$ $d + id$ superconductivity is supported within the $t - J$ model but it is never found to be the leading instability within the Hubbard model. The SSCL phase arises if long-range magnetic order in the SDW phase is quantum melted by strong quantum fluctuations. It also breaks TRS but not translational and rotational symmetry. In the finite size systems studied in [82] no distinction between the SDW and the SSCL phase could be made because of the lack of long-range order. The SSCL state has not been found in previous studies.

3.3 Methodology

To describe systems of strongly correlated electrons, a variety of model Hamiltonians have been introduced. In this thesis, a simple one-band Hubbard Hamiltonian

$$H = - \sum_{\langle i,j \rangle, \sigma} t_{i,j} \left(c_{i,\sigma}^\dagger c_{j,\sigma} + \text{H.c.} \right) + U \sum_i n_{i,\uparrow} n_{i,\downarrow} - \mu \sum_i n_i \quad (3.8)$$

is used.

The first term can be identified with a kinetic energy that allows electrons to hop between sites i and j via the hopping matrix $t_{i,j}$, which represents the transfer integral between the two sites. In many cases it is sufficient to take only nearest neighbor hopping between adjacent sites into account. The hopping matrix $t_{i,j}$ should of course be translational invariant ($t_{i,j} = t_{j,i}$), which fulfilled by a uniform t . In a homogeneous system t is taken to be uniform within all sites of the lattice anyways. Depending on the sign of t , the interaction becomes ferromagnetic ($t < 0$) or antiferromagnetic ($t > 0$). Since ferromagnetic interactions usually simply generate

ferromagnetic phases at low temperatures if they are the leading energy scale, antiferromagnetic interactions can lead to rich phase diagrams and frustration effects. An antiferromagnetic $t > 0$ is therefore assumed in this study. Furthermore, $t = 1$ will define the energy scale for simplicity. The second-quantized operators $c_{i,\sigma}^\dagger (c_{i,\sigma})$ create (annihilate) an electron at site i with the spin σ , which can take the two values \uparrow or \downarrow .

The second term of the Hubbard Hamiltonian 3.8 describes the Coulomb repulsion. Hereby, U is the energy that needs to be paid when two electrons are located on the same site i . Following Pauli's principle these two electrons must have opposite spin directions. In the limit of very large Coulomb interaction $U \gg t$ the system tries to avoid double-occupancies at any cost. For half filling this results in the classical solutions, for example the 120° phase from Fig. 3.2 in case of a triangular lattice or a nonfrustrated antiferromagnet on the 2D square lattice.

The third term of the Hubbard Hamiltonian determines the particle number of the system using the chemical potential μ . The number operator on site i is given by $n_i = \sum_\sigma c_{i,\sigma}^\dagger c_{i,\sigma}$. To push the Fermi energy of the noninteracting triangular lattice towards the van Hove singularity at $3/4$ filling, $\mu = 2.0$ is needed, as applied in Fig. 3.3.

The reciprocal lattice vectors of the triangular lattice are

$$\mathbf{b}_{1/2} = \left(\frac{2\pi}{a}, \pm \frac{2\pi}{\sqrt{3}a} \right), \quad (3.9)$$

where for the lattice parameter $a = 1$ is used for simplicity. Using the Hubbard Hamiltonian from Eq. (3.8), these immediately lead to the noninteracting tight-binding energy

$$\varepsilon(\mathbf{k}) = -2t \left[\cos(k_x) + 2 \cos\left(\frac{k_x}{2}\right) \cos\left(\frac{\sqrt{3}}{2}k_x\right) \right] - \mu. \quad (3.10)$$

The employed program code used easily allows the construction of square lattices but problems arise when the triangular lattice needs to be included. As a workaround the triangular lattice is mapped onto a square lattice in the way pictured in Fig. 3.12. Here, the original square lattice becomes triangular by including additional hopping elements t in on diagonal direction. With this transformation one also changes the properties of the reciprocal space. The new reciprocal lattice vectors

for the implemented triangular lattice are

$$\mathbf{b}'_1 = \left(\frac{2\pi}{a}, -\frac{2\pi}{a} \right), \quad \mathbf{b}'_2 = \left(0, \frac{2\pi}{a} \right). \quad (3.11)$$

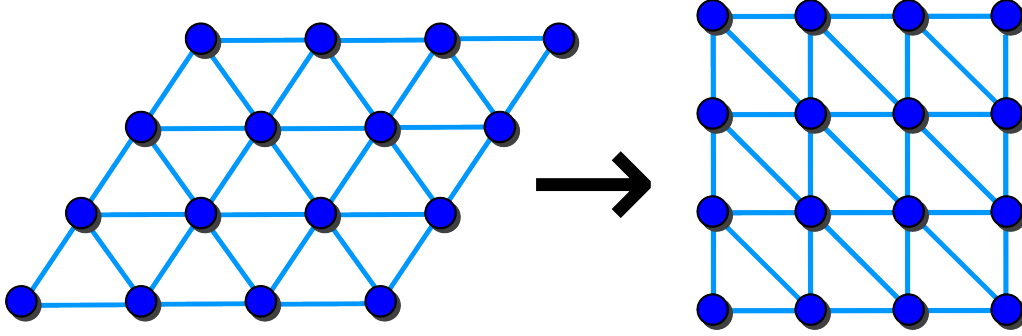


Figure 3.12: Deformation of the original triangular lattice when mapped onto a square lattice.

The resulting tight binding energy is denoted by

$$\varepsilon(\mathbf{k}) = -2t [\cos(k_x) + \cos(k_y) + 2 \cos(k_x + k_y)] - \mu, \quad (3.12)$$

which is shown on the right side of Fig. 3.13. The shape of the original Brillouin zone is reconstructed using the symmetry of $\varepsilon(\mathbf{k})$.

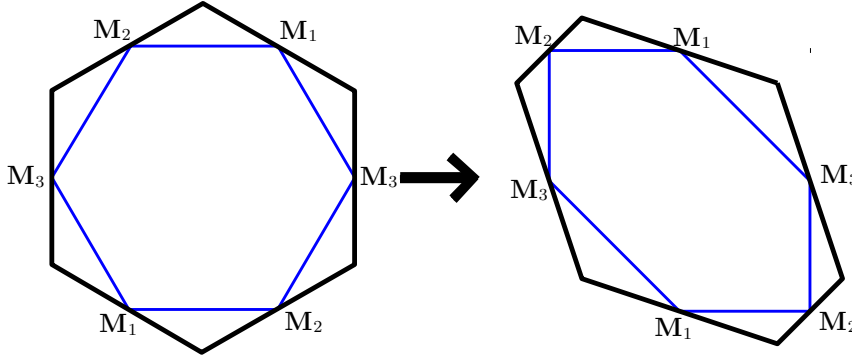


Figure 3.13: Deformation of the Brillouin zone (black) and the Fermi surface at van Hove filling (blue) if the transformation from Fig. 3.12 is applied.

The problem of selecting a proper cluster for CPT or VCA calculations arises immediately. One has to pay attention to different limitations, pictured in Fig. 3.14. First of all, the isolated cluster has to be solvable by ED, which limits the size of the cluster depending on other (e.g. orbital or spin) degrees of freedom and the size of the respective Hilbert space. In the case of a one-band Hubbard model on the triangular

lattice, possible cluster sizes range up to approximately 12 sites. Beyond this size the Lanczos algorithm requires too much memory and can therefore not be executed.

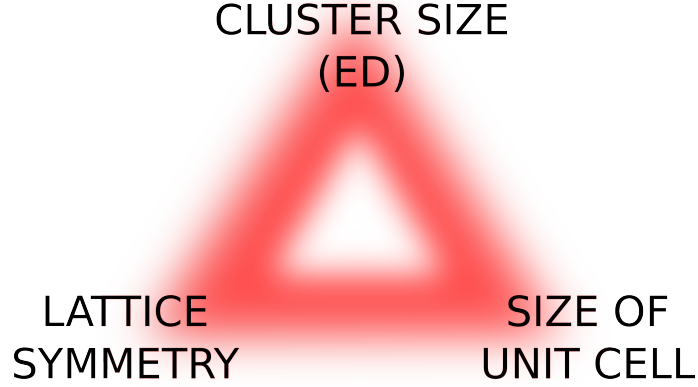


Figure 3.14: Illustration of the interplay between the different mechanisms limiting the choice of the cluster.

The other two limitations given in Fig. 3.14 do not limit the actual executability of the calculation, but they may have an severe impact on the quality of the results. When choosing a cluster geometry, attention has to be paid that a possible ordered phase fits onto the cluster. Additionally, any long-range ordered phase has to be reproduced when the clusters are aligned in 2D. Taking for example a SDW phase with a quadrupled unit cell, such as the chiral phase pictured in Fig. 3.15(a), limits the choice of the cluster to a size of a multiple of four. In addition, aligning the clusters has to reproduce the pattern of the local moments.

Another limitation arises from the underlying symmetry of the lattice. Clusters shall be ‘as symmetric as possible’, which can for example be measured by the number of bonds into the different spatial directions. Of course, these limitation interact, leaving only little space choosing a fitting cluster.

In this scenario we want to study several magnetically ordered phases shown in Fig. 3.15 and presented in Sec. 3.2.1, plus additional superconducting phases, proposed in Sec. 3.2.2. In addition to the chiral SDW phase (Fig. 3.15(a)) and the four-sublattice collinear phase (Fig. 3.15(b)), we study a collinear phase with a 3-site unit cell and nonuniform local moments (Fig. 3.15(c)) and a bipartite collinear ‘stripe’ phase with ferromagnetic interactions into one hopping direction and AFM interactions into the other two directions (Fig. 3.15(d)). Keeping in mind that finite size effects will arise,

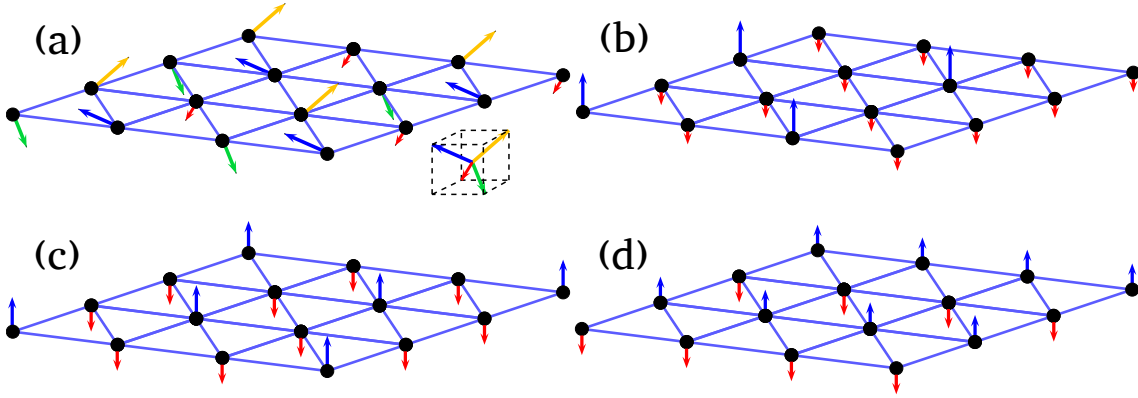


Figure 3.15: Different possibilities of magnetic ordering on a triangular lattice. (a) Noncoplanar phase on a 4-site unit cell where the magnetic moments of the respective sublattice point towards the corners of a regular tetrahedron. (b) 4-site collinear phase with nonuniform spin moments. On the quadrupled unit cell one finds three sites with a small spin moment $-\Delta$ while the other site exhibits a large moment 3Δ . (c) 3-site collinear state with with 2 moments of the value $-\Delta$ and one moment with 2Δ . (d) 2-site collinear stripe phase with ferromagnetic ordering along one direction and antiferromagnetic ordering along the other direction.

which may limit the comparability of different cluster shapes, a ‘one for all’ solution which allows studying all phases on the same cluster is sought after.

Figure 3.16 reviews cluster sizes and shapes used in this thesis. The smallest 4-site cluster (Fig. 3.16(a)) is only used as a starting point due to fast numerical convergence resulting from small system size. Such a small system might be a good approximation for square lattices, but it becomes highly anisotropic in the case of a triangular lattice with only one diagonal connection and two bonds in the respective directions of the square lattice. Additionally, the 3-site collinear SDW phase from Fig. 3.15(c) cannot be studied using this cluster. The 7-site cluster shown in Fig. 3.16(b) has been designed to study superconducting phases with different order parameters. It exhibits a high isotropy and preserves the point group symmetry of the lattice. The maximal cluster size for studying superconducting phases on the triangular lattice within the single-band Hubbard model turns out to be 8 for the hardware used. Two examples of 8-site clusters are pictured in Fig. 3.16(c) and Fig. 3.16(d), where the former exhibits a quite large anisotropy and the latter is fairly symmetric. Both 8-site clusters allow a mapping of SDW phases with quadrupled unit cell for comparability reasons.

The largest cluster used in this thesis is the 12-site cluster shown in Fig. 3.16(e),

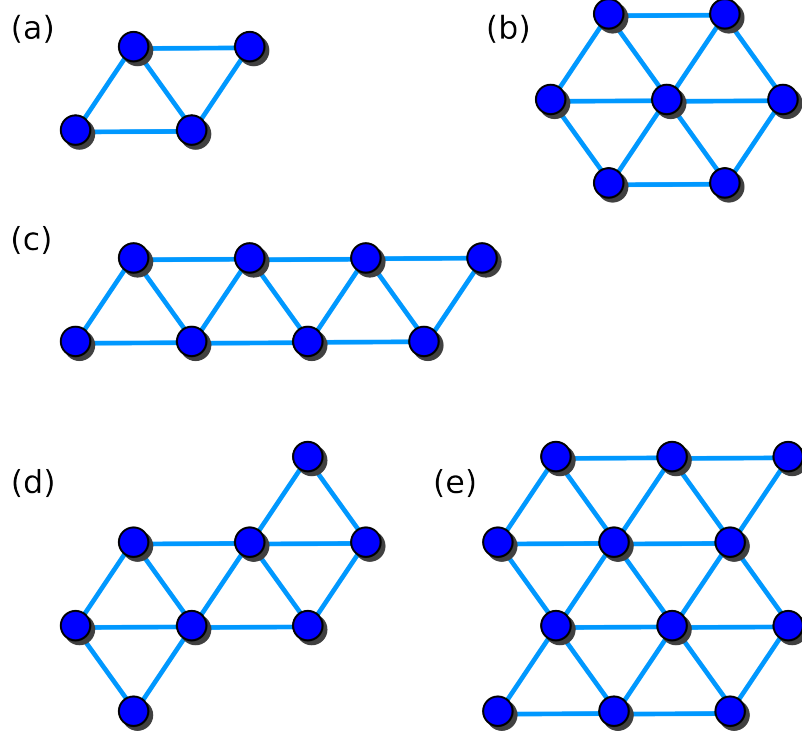


Figure 3.16: Overview over the different cluster sizes and shapes used in this thesis: (a) small 4-site cluster, (b) 7-site cluster that preserves lattice symmetry of the triangular lattice, (c) first 8-site cluster, (d) second 8-site cluster and (e) largest possible cluster with 12 sites.

which is used to compare the stability of the proposed SDW phases in Fig. 3.15. The shape and the size of this 12-site cluster allows a treatment of all SDW phases with doubled, tripled and quadrupled unit cells on equal footing. Only the mapping of the cluster on the 2D plane has to be re-arranged, as pictured in Fig. 3.17. Therefore, long-range ordered phases with quadrupled unit cells can be reproduced for superlattice vectors $(2, 2)$ and $(4, -2)$ (in units of a) and a phase with tripled unit cell can be obtained by superlattice vectors $(3, 0)$ and $(1, -3)$.

For the implementation of superconducting order parameters, a particle-hole transformation in one spin channel is conducted to be able retrieve order parameters which are coupled to one-particle operators within mean-field decoupling:

$$d_{i,\uparrow}^\dagger = c_{i,\uparrow}, \quad d_{i,\uparrow} = c_{i,\uparrow}^\dagger, \quad d_{i,\downarrow} = c_{i,\downarrow}, \quad d_{i,\downarrow}^\dagger = c_{i,\downarrow}^\dagger. \quad (3.13)$$

Application of this transformation to the Hubbard Hamiltonian 3.8 leads to the

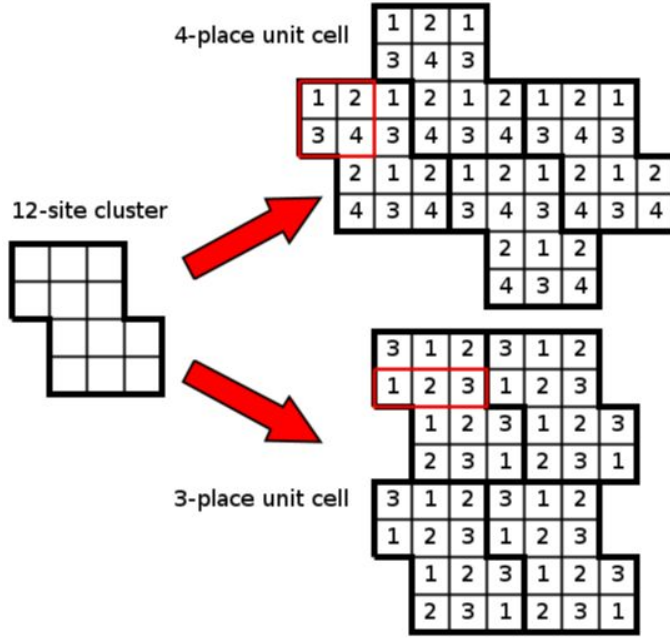


Figure 3.17: Possible cluster shape of a 12-site cluster to fit 4-place unit cells (like the ones showed in Fig. 3.15(a) and Fig. 3.15(b)) and 3-place unit cells (Fig. 3.15(c)) into the resulting lattice by aligning the cluster in the two different ways shown. Note that the cluster shown in Fig. 3.16(e) is hereby transformed on a square lattice with additional diagonal bonds into one direction, as pictured in Fig. 3.12. These diagonal bonds are not shown in the figure. Each square stands for one site and numbers within the square indicate the number of the site within the unit cell (red frame).

Hamiltonian \tilde{H} in the new basis of the operators $d_{i,\sigma}^\dagger$ and $d_{i,\sigma}$,

$$\tilde{H} \propto -t \sum_{\langle i,j \rangle, \sigma} (d_{i,\sigma}^\dagger d_{j,\sigma} - \text{H.c.}) - U \sum_i n_{i,\uparrow} n_{i,\downarrow} + U \sum_i n_{i,\uparrow} - \mu \sum_i n_{i,\uparrow} + \mu \sum_i n_{i,\downarrow}, \quad (3.14)$$

whereas $d_{i,\uparrow}^\dagger$ and $d_{i,\downarrow}$ now describe the creation and annihilation of a hole. The main changes of \tilde{H} with respect to 3.8 are a sign change in the hopping t for the spin-down channel and a total sign change in the Coulomb repulsion U , which is now attractive. Also, the chemical potential μ_\uparrow seen by the spin-up electrons and the one seen by the spin-down holes (μ_\downarrow) is different now. Here, the holes experience a sign change in the chemical potential $\mu_\downarrow = -\mu$, whereas the electrons see an additional term corresponding to the strength of the Hubbard interaction $\mu_\uparrow = \mu + U$.

The above transformation changes the effective filling within the lattice. While the electron channel stays at 3/4 filling, half of the particles are transformed into holes, which only fill the system to one quarter. Therefore, the lattice is now effectively half filled at the van Hove singularity, which increases the Hilbert space with respect

to the original 3/4 filled state. At this point, ED of the 12-site cluster that was chosen to study SDW phases (see Fig. 3.16(e)) fails and a switching towards smaller clusters is inevitable, limiting the comparability between the two types of phases.

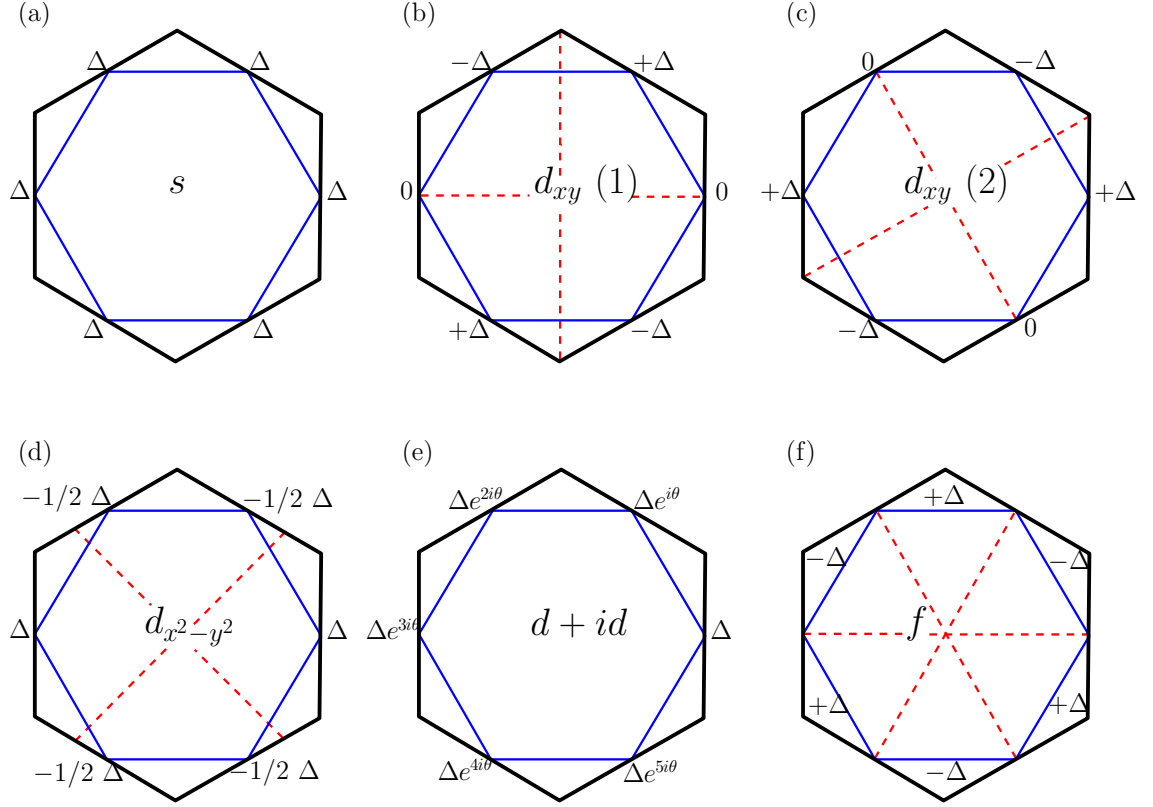


Figure 3.18: Possible order parameters of superconducting phases on the hexagonal Fermi surface of the triangular lattice: (a) s -wave symmetry with uniform order parameter, (b) and (c) d_{xy} -wave symmetry with two different arrangements, (d) $d_{x^2-y^2}$ -wave symmetry, (e) time reversal and pairing symmetry breaking $d_{x^2-y^2} + id_{xy}$ -wave symmetry, (f) triplet f -wave symmetry. Red dashed lines indicate nodes of the order parameter.

Figure 3.18 gives an overview about the superconducting order parameters studied at van Hove filling on the triangular lattice. As s -wave superconductivity (Fig. 3.18(a)) has been omitted since it is suppressed in all previous studies, three different alignments of order parameters with d -wave symmetry have been implemented. In addition to d_{xy} and $d_{x^2-y^2}$ -wave symmetry (Fig. 3.18(b) and Fig. 3.18(d)) an additional phase with d_{xy} symmetry has been studied, where the order parameter has been rotated by 60° (Fig. 3.18(c)). This rotated phase equals the phase shown in Fig. 3.18(b) if rotational symmetry is preserved within the cluster, as can be seen by a comparison of the gap symmetries in Fig. 3.18. A comparison of the properties

of the two phases with d_{xy} -wave character therefore allows a judgement about the symmetry of the cluster.

After implementing hoppings, interactions, the number of particles within the cluster, and the respective ordering Weiss fields, the VCA is applied to the system to evaluate the grand potential Ω . Here, the results of CPT calculations are optimized by applying a variational procedure on one-particle operators while searching for a stationary point in the grand potential in the subspace of the one-particle operators. A variation of an additional chemical potential $v\mu$ shall always be included to ensure thermodynamic consistency [83]. Optimizing the chemical potential leads to a change in the filling fraction and demands a new selection of the original chemical potential when searching for a particular filling. Of course, also the order parameter should be optimized, which allows the determination of the strength of the order parameter and therefore the detection of a phase transition. In the case of $d+id$ superconductivity, the superposition of the $d_{x^2-y^2}$ and d_{xy} order parameters is treated as two individual order parameters. This allows to obtain information whether the system chooses a chiral superposition of the two order parameters or only one order parameter.

After the VCA finishes, the optimized one-particle Green function of the full system is obtained. This allows the calculation and visualization of one-particle properties of the system, such as the quasiparticle spectrum, Fermi surface and density of states. In particular, the formation of a gap can be studied, which is essential for various phases.

3.4 Results

In this section, the VCA results that were obtained with different cluster sizes and shapes are presented. An evaluation of the influence of the choice of the cluster is given afterwards in Sec. 3.4.7.

3.4.1 SDW Phases on a 12-site Cluster

The 12-site cluster shown in Fig. 3.16(e) turned out to be the most promising candidate to study the stability of ordered SDW phases on the triangular lattice at van Hove filling. Since the size of the cluster is limited by ED, a 12-site cluster displays the largest possible system size. Luckily, the particular shape of the 12-site cluster

allows the treatment of ordered phases with trippled and quadrupled unit cells on equal footing, just by re-arranging the cluster alignment like pictured in Fig. 3.17 due to the fact that 12 is the lowest common multiple of 3 and 4. Therefore, a comparison between the particular ordered phases becomes possible.

Table 3.1: Calculated grand potentials Ω from VCA for selected types of magnetic order parameters at different on-site interactions U (in units of t) for the 12-site cluster (3.16(e)) at 3/4 filling. Additional information is given about the value of the respective chemical potential μ and the optimized values for the variational procedure on the chemical potential $-v\mu$ and on the order parameter.

U	μ	$-v\mu$	order parameter	value	Ω
1	2.773	0.407	noncoplanar	0.023	-4.823
1	2.77	0.404	4-site collinear	0.024	-4.818
12	13.06	0.232	noncoplanar	0.11	-14.577
12	13.15	0.345	4-site collinear	0.095	-14.723
12	13.09	0.412	3-site collinear	0.085	-14.628
12	13.09	0.352	2-site collinear	0.04	-14.629
20	20.99	0.205	noncoplanar	0.115	-22.451
20	21.07	0.372	4-site collinear	0.075	-22.588
20	21.01	0.334	3-site collinear	0.085	-22.498
20	21.02	0.36	2-site collinear	0.06	-22.508
40	40.95	0.178	noncoplanar	0.12	-42.374
40	41.00	0.38	4-site collinear	0.07	-42.477
40	40.98	0.37	3-site collinear	0.08	-42.446
40	40.97	0.37	2-site collinear	0.09	-42.426

In Tab. 3.1 the results for the grand potential Ω of the respective SDW phase for different strengths of the Hubbard interaction U is given. For small values of U , either no optimized solution with a stationary point in the grand potential was found for a nonzero order parameter, or the order parameter was very small. As an example, results are given for $U/t = 1$ for the chiral phase and the 4-sublattice collinear phase. The respective order parameter is very small, compared to the results at increased Coulomb interaction and they lie extremely close to the energy of the disordered ground state with no order parameter. For the coplanar SDW phases with trippled unit cell and for the stripe-like phase, no finite order parameter has been found at all. The characteristics of the strength of the order parameters is somehow consistent using the 12-site cluster, reaching from very small to vanishing strength in the weak-coupling regime towards a finite order parameter at stronger interactions, whereas the stability of the respective SDW phases becomes rather uncontrolled on

smaller clusters, as can be seen in the following sections.

The SDW states start to exhibit a recognizable order parameter in the regime of intermediate to strong coupling. In Tab. 3.1, results are given for $U = 12$, $U = 20$, and $U = 40$ (in units of t). When comparing the stability of the individual phases by the value of their grand potential, one finds that in the whole regime *collinear* phases have lower grand potentials than the noncoplanar chiral phase.

As one aim of this thesis is to compare SDW phases to superconducting phases, also several superconducting order parameters were implemented following the procedure described in Sec. 3.3. Unfortunately, the particle-hole transformation of one spin channel (Eq. (3.13)) increases the Hilbert space of the cluster, which prevents a successful application of the ED algorithm because the effort increases exponentially and machines may run out of memory. In the following sections, smaller clusters are applied to the system, which allow a treatment of superconducting phases. But, as there is always a price to pay, other limitations arise, as will be discussed in the following sections.

3.4.2 Results Using a Minimal 4-site Cluster

After a successful implementation of the superconducting order parameters into the Hamiltonian, the small 4-site cluster shown in Fig. 3.16(a) is used to gain insight into the stability of the phases with moderate numerical effort. Since the system size is rather small, strong finite-size effects are to be expected.

The results delivered in Tab. 3.2 are partly inconsistent. For example, the results lack the feature of degenerate superconducting states with d -wave symmetry. Because of the 6-fold lattice symmetry, phases with a d_{xy} and a $d_{x^2-y^2}$ order parameter should be degenerate. Therefore, also the value of the respective grand potential should be the same. As can be seen in Tab. 3.2 and in Fig. 3.19, all superconducting states with d -wave symmetry are severely split along a large energy scale, displaying the intrinsic asymmetry of the 4-site cluster.

An attempt to quantify the symmetry of a cluster could be made by counting the number of bonds into the respective spatial direction. Obviously, the 4-site cluster possesses two bonds into x and y direction (from the implemented cluster point of view, where the triangular lattice has been mapped onto a square lattice), and only one bond into the diagonal direction. Additionally, one can define a scaling

Table 3.2: Calculated grand potentials Ω from VCA for selected types of magnetic ordering and superconducting order parameters at different on-site interactions U (in units of t) for the 4-site cluster shown in Fig. 3.16(a) at 3/4 filling.

U	μ	$-v\mu$	order parameter	value	Ω
1	2.79	0.668	noncoplanar	<0.02	-4.839
1	2.79	0.663	4-site collinear	0.00008	-4.839
1	2.77	0.47	$d_{x^2-y^2}$	0.472	-4.832
1	2.79	0.574	d_{xy} (1)	0.919	-4.868
1	2.77	0.44	d_{xy} (2)	0.22	-4.813
1	2.81	0.538	f -wave	0.5889	-4.881
4	5.20	0.543	$d_{x^2-y^2}$	0.565	-6.9068
4	5.31	0.674	d_{xy} (1)	0.880	-7.041
4			d_{xy} (2)	- - -	
4	5.50	0.552	f -wave	0.475	-7.321
8			$d_{x^2-y^2}$	- - -	
8	9.08	0.709	d_{xy} (1)	0.647	-10.634
8	9.04	0.326	d_{xy} (2)	0.28	-10.55
8	9.38	0.632	f -wave	0.338	-11.091
12			$d_{x^2-y^2}$	- - -	
12	13.01	0.689	d_{xy} (1)	0.601	-14.493
12	13.30	0.226	d_{xy} (2)	0.300	-14.864
12	13.34	0.666	f -wave	0.280	-15.011
40	41.08	0.111	noncoplanar	<0.1	-42.56
40	41.35	0.760	2-site collinear	0.00001	-42.99
40	40.90	0.507	$d_{x^2-y^2}$	0.368	-42.365
40	41.37	0.788	d_{xy} (1)	0.25	-42.98
40	41.28	0.707	d_{xy} (2)	0.28	-42.91
40	41.28	0.695	f -wave	0.214	-42.811

parameter Q defined by the fraction of the number of hopping links inside the clusters divided by the number of total links within a unit cell of the super-lattice of clusters [84]. For the present 4-site cluster we find a value of $Q \approx 0.61$, which means that almost 40% of the original bonds are treated as a perturbation and therefore phases with different symmetries of the order parameter are treated inequivalently. As a result, the grand potentials of the respective phases become nondegenerate and the strength of their order parameters vary to a large extent and become heavily dependent on the strength of the interaction, as visible in Tab. 3.2 for five values of the Coulomb interaction, reaching from the weak-coupling regime of $U = 1$ to strong coupling with $U = 40$. Actually, in the case of intermediate interactions, several phases like the superconducting phase with $d_{x^2-y^2}$ order parameter at $U = 8$ could not be stabilized at all, which shows the severe symmetry-dependence of the

calculations.

Figure 3.19 shows the behavior of the different superconducting phases and SDW phases that could be stabilized on the 4-site cluster around the van Hove filling of $n = 1.5$ electrons per site for a wide range of interactions from $U = 1$ to $U = 40$. Especially in the weak-coupling regime of $U = 1$ and in the scenario of strong interactions at $U = 40$ one can clearly observe the phenomenon that only certain phases are stabilized within the VCA, while others, including all SDW phases, remain in the regime of the grand potential of the disordered ground state (see Tab. 3.6) with no order parameter. In Fig. 3.19(a) for $U = 1$, only the phases with superconducting d_{xy} order parameter and the phase with f -wave symmetry differ significantly from the energy of the disordered state. The grand potential of the superconducting phase with the order parameter denoted as ' $d_{xy}(2)$ ', which equals ' $d_{xy}(1)$ ' rotated by 60° actually lies above the grand potential of the disordered phase and is therefore disfavored. At the same time ' $d_{xy}(1)$ ', the other phase with d_{xy} -symmetry, is preferred in comparison to the energy of the disordered state, whereas the state with $d_{x^2-y^2}$ -symmetry remains near energy of the disordered state, despite exhibiting a finite order parameter. The fact that all three superconducting phases with d -wave symmetry act different might result from the large anisotropy of the small cluster. At larger values for the Coulomb interaction a similar picture arises but the order of the d -wave phases is permuted (e.g. in Fig. 3.19(e)), which indicates inconsistency in the results.

In the regime of weak to medium interactions, the superconducting state with triplet f -wave symmetry wins but the result should be treated with caution, for the reasons mentioned above. In the following sections larger cluster sizes are discussed with the goal of achieving an improvement in the quality of the results.

3.4.3 Results Using 8-site Clusters

Due to the poor quality of the results using a cluster with only four sites the cluster size has been increased to improve the consistency of the results. To retain the goal of providing comparability with SDW phases the cluster size is increased towards eight sites, which turns out to be the maximum cluster size solvable for ED for systems with superconducting order parameters. The shape of the 8-site cluster is selected following the demand of allowing a tiling of SDW phases with quadrupled unit cells, which allows at least the option to compare the results of the respective

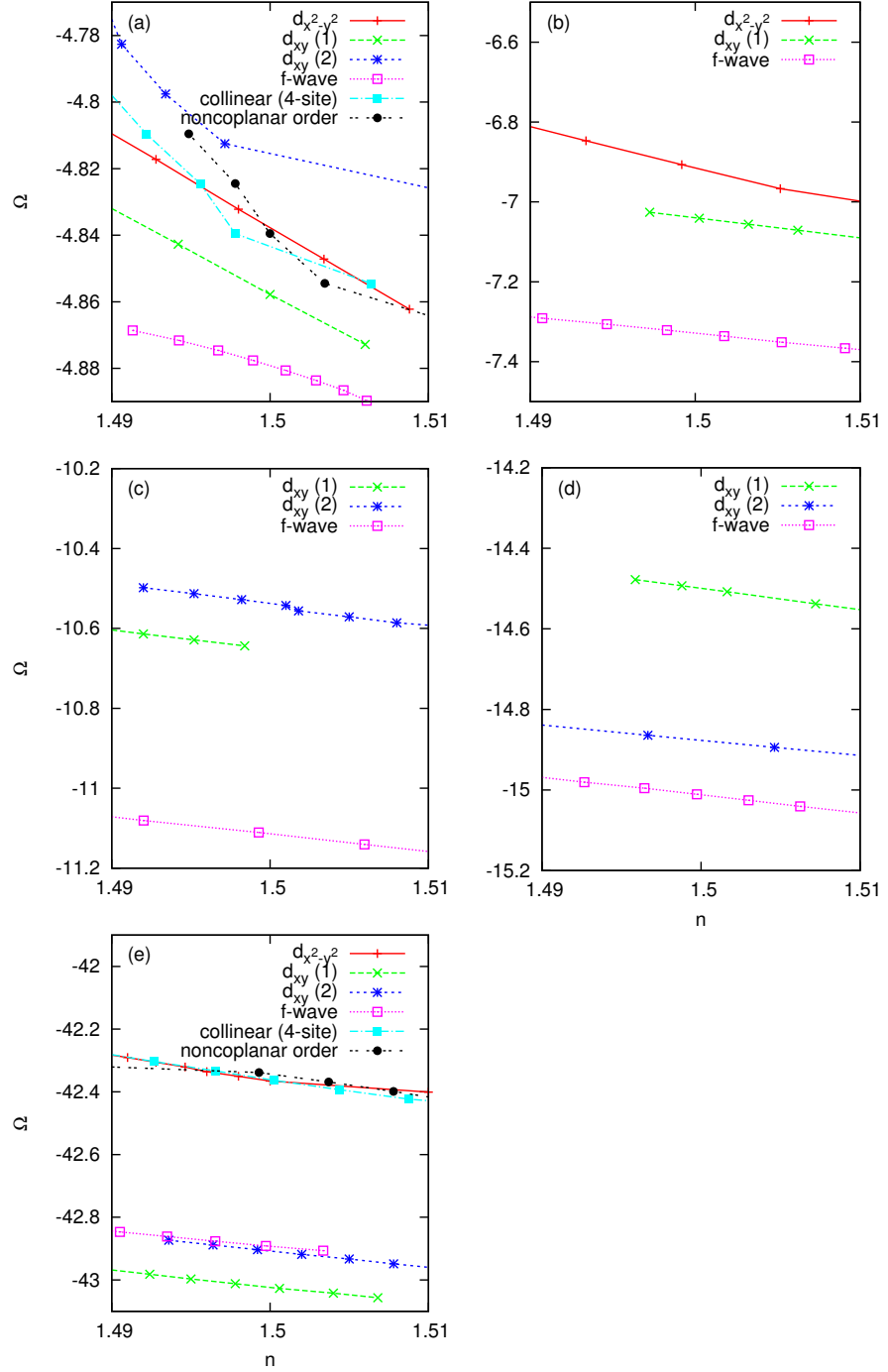


Figure 3.19: The grand potential Ω as function of the doping n around the van Hove filling for (a) $U=1$, (b) $U=4$, (c) $U=8$, (d) $U=12$, and (e) $U=40$ for the 4-site cluster given in Fig. 3.16(a).

superconducting phases to the energy of the 4-site collinear phase shown in Fig. 3.15(b). Although we drop a direct comparability with the 3-site collinear phase from Fig. 3.15(c), the SDW phases can still be compared with each other in the environment of the 12-site cluster in Sec. 3.4.2.

As a simple approach, a ‘brick-like’ cluster with a 2×4 layout is applied. This cluster, which is shown in Fig. 3.16(c), exhibits a scaling parameter of $Q \approx 0.71$, which is substantially better than the scaling parameter of the 4-site cluster. Nevertheless, the anisotropy of this cluster is quite large. It exhibits six bonds in the horizontal direction and four bonds in the vertical direction, while exhibiting only three diagonal bonds.

Another cluster shape, that allows a mapping of quadrupled unit cells, is presented in Fig. 3.16(d). Because its scaling parameter $Q \approx 0.72$ is comparable to the scaling parameter of the 2×4 cluster, its isotropy is much better. It exhibits four bonds into the horizontal and diagonal direction respectively and five bonds in the vertical direction, which should improve the results a lot.

Table 3.3: Calculated grand potentials Ω from VCA for selected types of magnetic ordering at different on-site interactions U (in units of t) for the ‘brick-like’ 8-site cluster from Fig. 3.16(c) at the van Hove filling.

U	$-\mu$	$-v\mu$	order parameter	value	Ω
1	-2.78	0.429	4-site collinear	0	-4.836
1	-2.77	0.413	$d_{x^2-y^2}$	0.377	-4.831
1	-2.78	0.974	d_{xy} (1)	0.027	-4.836
1	-2.77	0.546	d_{xy} (2)	0.385	-4.826
1	-2.78	0.612	f -wave	-0.112	-4.837
8	-9.18	0.274	4-site collinear	0.038	-10.769
8	-9.00	0.429	$d_{x^2-y^2}$	0.264	-10.564
8	-9.08	0.609	d_{xy} (1)	0.436	-10.629
8	-9.10	0.385	d_{xy} (2)	0.354	-10.690
8	-9.18	0.511	f -wave	0.189	-10.801
40	-40.98	0.171	4-site collinear	0.016	-42.412
40	-40.92	0.344	$d_{x^2-y^2}$	0.255	-42.311
40	-40.96	0.311	d_{xy} (1)	0.273	-42.392
40	-40.90	0.302	d_{xy} (2)	0.345	-42.335
40	-41.06	0.500	f -wave	0.171	-42.560

The results for the grand potential of the respective phases at van Hove filling on the 2×4 cluster are summarized in Tab. 3.3. In the weak-coupling regime at $U = 1$ all

superconducting phases deliver comparable values for the respective grand potential, only with slight deviations. Additionally, the order parameter of the 4-site collinear phase vanishes, leaving a disordered state behind, which energy lies also in the same regime. Since none of the grand potentials of the respective superconducting states is considerably lowered compared to the disordered states, one may conclude that none of the superconducting phases is stabilized despite exhibiting a finite order parameter.

In the intermediate coupling regime at $U = 8$ the values of the grand potential of the respective superconducting phases split up, leaving triplet f -wave superconductivity as the leading ground state. The negative aspect of the splitting of the ground state energies lies in the arising nondegeneracy of the states with d -wave symmetry. At least, the regime of stable d -wave superconducting states is separated from the other phases and none of the d -wave states is supported. Close to the leading f -wave superconducting state, the 4-sublattice collinear SDW state has been found. Despite a significantly smaller order parameter its grand potential lies only slightly above the one of f -wave superconductivity.

Towards strong coupling ($U = 40$), the picture changes only quantitatively. The distance between the preferred f -wave superconducting phase and the 4-site collinear SDW state increases significantly, whereas the d -wave states are still not supported and nondegenerate. Compared to the medium-coupling regime, the absolute splitting of their energies did not increase with stronger interactions, which is indeed an improvement compared to the results of the 4-site cluster in Sec. 3.4.2.

The behavior of the grand potential of the respective SDW and superconducting phases for fillings around the van Hove singularity is pictured in Fig. 3.20 for the weak-coupling regime of $U = 1$, an intermediate regime at $U = 8$ and for strong-coupling at $U = 40$. As the results of Tab. 3.3 indicate, for $U = 1$ (Fig. 3.20(a)) all phases with nonvanishing order parameter are very close in energy and lie near the grand potential of the disordered state, which indicates that none of these phases might be stabilized. Additionally, no solution with finite order parameters could be found regarding time-reversal symmetry breaking $d + id$ superconductivity, which may emerge if the d -wave channels are degenerate. In the regime of intermediate couplings (Fig. 3.20(b)), an interesting transition from f -wave superconductivity at fillings smaller than van Hove filling towards collinear SDW at fillings slightly above $3/4$ filling is observed. The origin of this transition is not clear and the effect

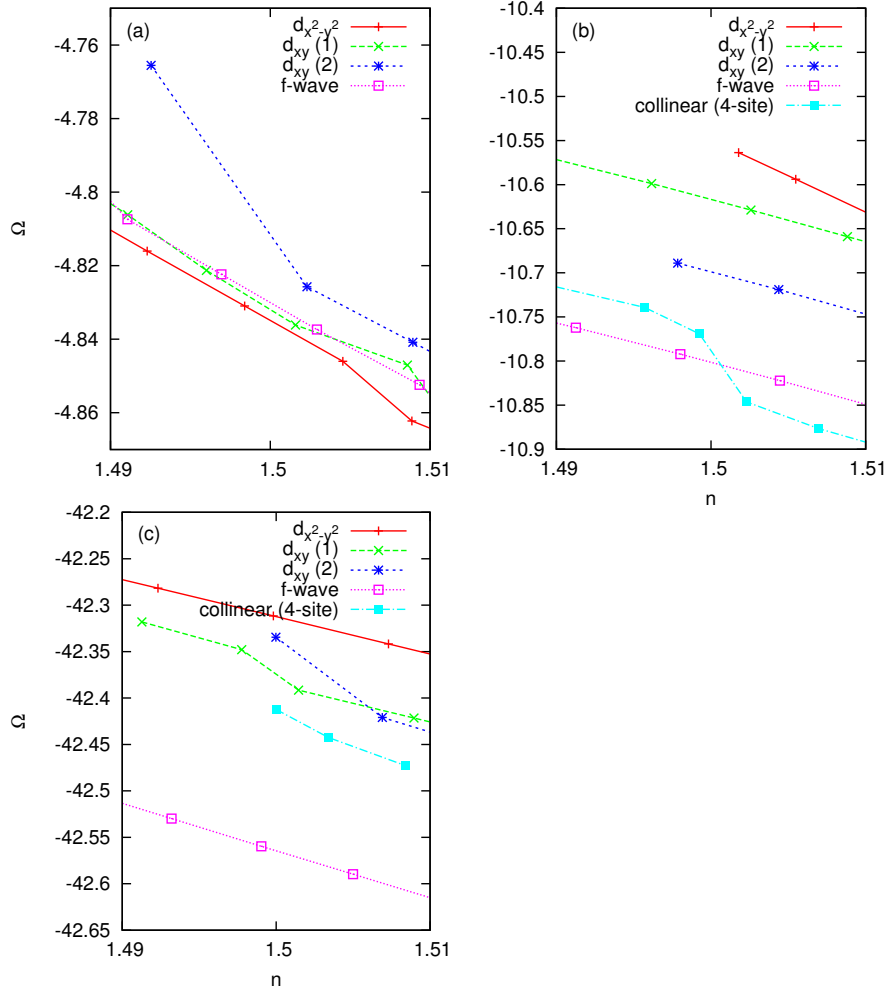


Figure 3.20: The grand potential Ω as function of the doping n around the van Hove filling for (a) $U=1$, (b) $U=8$, and (c) $U=40$ for the 8-site cluster given in Fig. 3.16(c).

is somehow counter-intuitive, as triplet f -wave superconductivity is believed to be especially stable for fillings beyond van Hove filling where the Fermi surface is disconnected into six different pockets that are situated at the corners of the Brillouin zone. In the regime of strong interactions at $U = 40$ (Fig. 3.20(a)) the large energy difference between the supported f -wave superconducting state and all other states is visible.

As a robust conclusion that may be drawn on the basis of the results of the 2×4 cluster one may state that an improvement of the results could be achieved with respect to the 4-site cluster. But still, the quality of the results is not satisfying. Since no leading instability could be found at $U = 1$, increasing interactions seem to prefer f -wave superconductivity, even at fillings slightly smaller than van Hove filling.

To further improve the results, similar studies were performed using the 8-site cluster shown in Fig. 3.16(d), which exhibits a much better isotropy.

Table 3.4 shows the results for the grand potentials and order parameters for the respective phases at different strengths of interaction for the 8-site cluster shown in Fig. 3.16(d). As SDW phases could not be stabilized within this cluster, chiral $d + id$ superconductivity is observed at certain values of Coulomb repulsion. For example, a $d + id$ -wave superconducting phase has been found at weak coupling for $U = 1$. Hereby, the emerging chiral superconducting state is a superposition of the states with $d_{x^2-y^2}$ and d_{xy} (2) symmetry. These two states are almost degenerate, allowing a complex superposition of both to form the chiral superconducting state. Unluckily, the other superconducting phase with d -wave symmetry is not degenerate with the other two as it is disfavored by a quite large amount of energy. While the superconducting phase with f -wave symmetry lies close to the (almost) degenerate d -wave states, the grand potential of the $d + id$ -wave superconducting phase is lowered slightly by the superposition of d -wave states, making it the supported ground state in the weak-coupling regime.

Towards intermediate to strong couplings, the situation gets messy with a comparable large splitting of energy between states with d -wave character at $U = 4$ and $U = 8$. This splitting of the d -wave states takes place over the whole regime of the relevant energy scale, prohibiting a reliable conclusion about the nature of the ground state. In both cases a state with d_{xy} -wave symmetry is supported, whereas at

Table 3.4: Calculated grand potentials Ω from VCA for selected types of magnetic ordering and superconducting order parameters at different on-site interactions U (in units of t) for the 8-site cluster from Fig. 3.16(d) at 3/4 filling.

U	μ	$-v\mu$	order parameter	value	Ω
1	2.804	0.214	$d_{x^2-y^2}$	0.668	-4.877
1	2.78	0.615	d_{xy} (1)	0.28	-4.841
1	2.80	0.31	d_{xy} (2)	0.770	-4.869
1	2.80	0.537	f -wave	0.118	-4.872
1	2.81	0.119	$d + id$	0.563/0.350	-4.886
4	5.38	0.367	$d_{x^2-y^2}$	0.116	-7.152
4	5.36	0.569	d_{xy} (1)	0.751	-7.121
4	5.40	0.365	d_{xy} (2)	0.720	-7.171
4	5.39	0.592	f -wave	0.198	-7.170
8	9.18	0.219	$d_{x^2-y^2}$	0.508	-10.789
8	9.14	0.504	d_{xy} (1)	0.292	-10.739
8	9.23	0.279	d_{xy} (2)	0.214	-10.870
8	9.20	0.564	f -wave	0.272	-10.830
12	13.06	0.250	$d_{x^2-y^2}$	0.445	-14.577
12	13.04	0.473	d_{xy} (1)	0.291	-14.566
12	13.08	0.295	d_{xy} (2)	0.239	-14.627
12	13.14	0.549	f -wave	0.283	-14.715
12	13.08	0.175	$d + id$	0.396/0.206	-14.609
20	21.06	0.398	$d_{x^2-y^2}$	0.110	-22.576
20	20.98	0.462	d_{xy} (1)	0.293	-22.455
20	21.04	0.477	d_{xy} (2)	0.377	-22.562
20	21.09	0.543	f -wave	0.275	-22.619
40	41.16	0.556	$d_{x^2-y^2}$	0.120	-42.721
40	40.93	0.453	d_{xy} (1)	0.293	-42.363
40	41.14	0.544	d_{xy} (2)	0.230	-42.697
40	41.08	0.556	f -wave	0.252	-42.588

$U = 4$ the state with f -wave symmetry lies exceptionally close to the ground state. At further increased Hubbard interactions of $U = 12$ again two d -wave phases exhibit similar grand potential energies, allowing the formation of a $d + id$ -wave state with slightly reduced energies. The third d -wave state is also lowered in energy compared to the other two but the lowest grand potential is found for f -wave superconductivity.

A similar picture arises at stronger couplings of $U = 20$, where f -wave superconductivity wins again. Interestingly, the other d_{xy} -wave phase is now close in energy to the $d_{x^2-y^2}$ -wave phase but no chiral $d + id$ -wave order parameter could successfully

be applied. For $U = 40$, the picture changes again with the f -wave state situated in between the d -wave states. Again, no chiral superconducting phase could be found in this regime, although two d -wave phases are relatively close in energy.

The behavior of the respective superconducting phases near van Hove filling using the 8-site cluster from Fig. 3.16(d) is plotted in Fig. 3.21 for a wide range of interactions reaching from $U = 1$ to $U = 40$. In the regime of weak interactions at $U = 1$ (Fig. 3.21(a)), the system selects a superconducting phase with chiral $d + id$ -wave order parameter, which emerges from the two almost degenerate d -wave states. Increasing the interaction towards $U = 4$ (Fig. 3.21(b)) and $U = 8$ (Fig. 3.21(c)) unfortunately leads to a large splitting of the energies of the respective d -wave phases, prohibiting the formation of a chiral superconducting phase. The large difference in energy between the two phases with d_{xy} -wave character indicates a strong influence of the cluster geometry. In this regime of intermediate interactions it is difficult to determine the nature of the supported ground state. For example, triplet f -wave superconductivity becomes the ground state at $U = 4$ for fillings slightly beyond $3/4$ filling but it never has the lowest grand potential at $U = 8$, only to become favored again at increased interactions of $U = 12$ (Fig. 3.21(d)), where the overall picture has drastically changed with now two almost degenerate d -wave channels, which allow the formation of a $d + id$ superconducting state. The picture changes again when the Hubbard repulsion is increased towards $U = 20$ (Fig. 3.21(e)). While f -wave superconductivity remains the supported phase now, the other superconducting phase with d_{xy} -wave character is degenerate with the $d_{x^2-y^2}$ -wave phase, but no $d + id$ -wave superconducting phase could be found. To make things worse, at $U = 40$ (Fig. 3.21(f)) f -wave superconductivity becomes disfavored again, compared to the two d -wave states.

Summarizing the results of the 8-site cluster with improved symmetry properties compared to the 2×4 cluster, one has to admit that the quality of the results did not improve by the desired amount. Furthermore, even new shortcomings arise. The new 8-site cluster does not show any support of any ordered SDW phase in all regimes of interaction and the unphysical splitting of the superconducting states with d -wave states is even more pronounced than in the 2×4 cluster. Further inconsistencies include the only partial ability to form a chiral superconducting state out of two phases with d -wave symmetry and the behavior of the f -wave state, which gets supported at strong interactions but gets disfavored again at $U = 40$. Regarding consistency, the results of the 2×4 cluster (Tab. 3.3 and Fig. 3.20) deliver a much

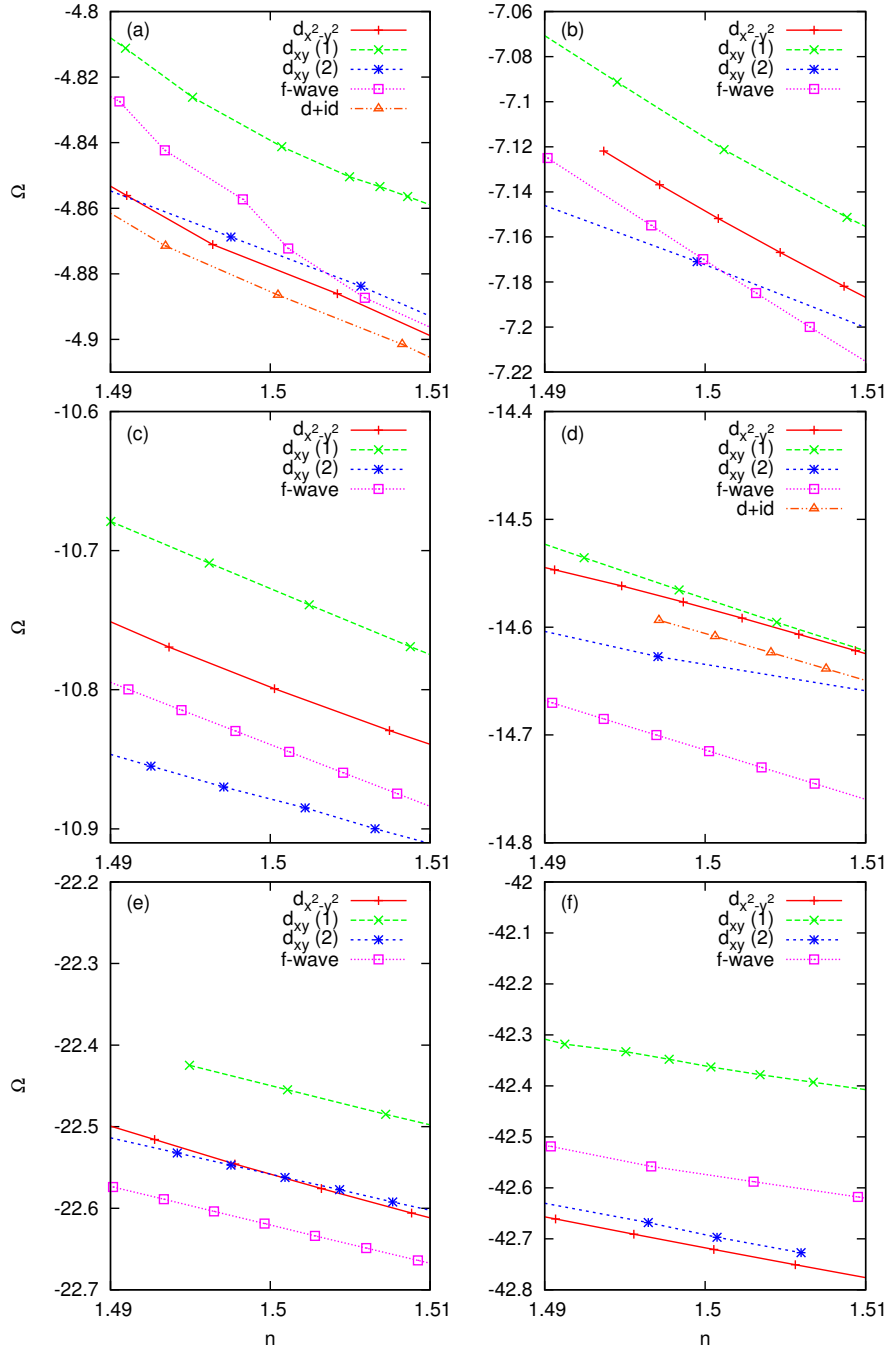


Figure 3.21: The grand potential Ω as function of the doping n around the van Hove filling for (a) $U=1$, (b) $U=4$, (c) $U=8$, (d) $U=12$, (e) $U=20$, and (f) $U=40$ for the 8-site cluster given in Fig. 3.16(d).

better quality of the results, with a clear signal towards f -wave superconductivity at strong coupling and a smaller splitting of the energies of the d -wave phases. Only in the regime of weak interactions the more symmetric 8-site cluster might have its advantages by determining the ground state to be a chiral superconductor, which is in coherence with most renormalization group studies at weak coupling.

3.4.4 Superconducting Phases on a 7-site Cluster

Due to the insufficient quality of the results of the previous sections using 8-site clusters, further cluster geometries are considered. Inspired by a study of Grandi *et al.* [58], clusters that preserve the original point group symmetry of the lattice might deliver substantially better results concerning one-particle parameters of the system. Such a 7-site cluster is shown in Fig. 3.16(b) for the triangular lattice. As the lattice symmetry is preserved, it is highly isotropic by exhibiting an equal number of bonds into the respective spatial directions. Its scaling parameter $Q \approx 0.76$ exceeds the ones of the 8-site clusters and within the bonds that are treated as a perturbation the bonds into different directions are distributed equally. This may be regarded as a huge improvement of the method. For example, every second vertical bond and an even higher percentage of diagonal bonds in the 2×4 cluster are treated as a perturbation, whereas only 14% of the horizontal bonds are treated perturbatively.

Despite the advantages, a 7-site cluster naturally prohibits the mapping of any ordered SDW phase. This shortcoming may be accepted at this point. How a comparison between different cluster geometries might be achieved nevertheless will be discussed later in Sec. 3.4.7.

Table 3.5 summarizes the results for superconducting phases within the VCA using the highly symmetric 7-site cluster shown in Fig. 3.16(b). This cluster preserves the point group symmetry of the lattice and is therefore believed to improve the quality of the results concerning superconducting phases, whereas a mapping of ordered phases with enlarged unit cells onto a cluster with seven sites is not possible. Therefore, SDW states cannot be compared to superconducting states as originally intended.

In the regime of weak interactions $U = 1$ the promising result of nearly degenerate d -wave superconducting states is found. All three phases with d -wave character lie very close in energy and chiral superconductivity emerges, lowering the grand potential considerably and therefore stabilizing $d + id$ -wave superconductivity as the

Table 3.5: Calculated grand potentials Ω from VCA for selected types of superconducting order parameters at different on-site interactions U (in units of t) for the 7-site cluster from Fig. 3.16(b) at 3/4 filling.

U	μ	$-v\mu$	order parameter	value	Ω
1	2.768	0.217	$d_{x^2-y^2}$	0.582	-4.815
1	2.764	0.153	d_{xy} (1)	0.760	-4.809
1	2.764	0.153	d_{xy} (2)	0.760	-4.809
1	2.804	0.276	$d + id$	0.513/0.737	-4.870
4	5.28	0.217	$d_{x^2-y^2}$	0.605	-6.975
4	5.22	0.214	d_{xy} (1)	0.820	-6.893
4	5.22	0.219	d_{xy} (2)	0.810	-6.893
4	5.34	0.2162	$d + id$	0.637/0.739	-7.061
12	12.86	0.418	$d_{x^2-y^2}$	0.221	-14.267
12	12.72	0.180	d_{xy} (1)	0.760	-14.060
12	12.71	0.163	d_{xy} (2)	0.790	-14.047
12	12.66	0.162	$d + id$	0.296/0.320	-13.966
20	20.76	0.434	$d_{x^2-y^2}$	0.227	-22.092
20	20.56	0.153	d_{xy} (1)	0.770	-21.797
20	20.57	0.160	d_{xy} (2)	0.760	-21.811
20	20.53	0.143	$d + id$	0.301/0.320	-21.751
40	40.66	0.444	$d_{x^2-y^2}$	0.232	-41.922
40	40.46	0.153	d_{xy} (1)	0.752	-41.625
40	40.45	0.159	d_{xy} (2)	0.746	-41.610
40	40.44	0.175	$d + id$	0.266/0.339	-41.600

ground state. Increasing Hubbard interaction towards $U = 4$ in principle yields the same result. The mayor difference lies in the lifting of the degeneracy of the d -wave phases with the $d_{x^2-y^2}$ -wave phase now being shifted towards lower energies. But still, a chiral superposition of the d -wave phases yields a stable solution for $d + id$ -wave superconductivity.

Increasing interactions towards $U = 12$ reveals a transition that might have appeared at intermediate couplings. The arrangement of the respective d -wave phases is comparable to the situation at $U = 4$ with two degenerate states with d_{xy} -wave character at a higher value of the grand potential and the $d_{x^2-y^2}$ -wave phase lying considerably lower. The chiral $d + id$ -wave phase now becomes disfavored and is lifted slightly above the superconducting phases with d_{xy} -wave character. As it is quite difficult to access the regime of intermediate interactions within the VCA, the exact regime of this transition could not be identified.

Towards strong interactions of $U = 20$ and $U = 40$ the picture obtained for $U = 12$ is retrieved with disfavored chiral superconductivity and a lowered $d_{x^2-y^2}$ -wave superconducting phase. This is of course a strange result, as all phases with d -wave character should be degenerate for symmetry reasons on the triangular lattice. The effect of a breaking of this degeneracy might indicate further shortcomings of the method like arising finite-size effects due to the small cluster size of only seven sites. Such a separation of the energies between the d -wave superconducting states may also indicate a tendency towards magnetic ordering, where the states with $d_{x^2-y^2}$ -wave symmetry and d_{xy} -wave symmetry react differently to short-range AFM correlations. This would explain the good degeneracy between the two phases with d_{xy} -wave symmetry and the increased difference to the $d_{x^2-y^2}$ -wave superconducting state when interactions are increased. A difference in the energies of the d_{xy} -wave and $d_{x^2-y^2}$ -wave phases could indicate tendencies of the system to lower its symmetry, which can be related to the formation of a SDW state. If such a SDW phase develops, the Fermi surface is modified, which would change the relative energies of the d -wave superconducting states.

Despite the partial nondegeneracy of the d -wave phases at intermediate to strong interactions the quality of the results using the symmetric 7-site cluster has indeed considerably improved. The results are now consistent with respect to the weak-coupling limit, where renormalization group approaches predict chiral superconductivity [59, 61, 78]. Additionally, the results are consistent compared with each other. Unlike previous studies on other clusters, where the stability of certain phases changes drastically with a change of interactions, the alignment of the phases in Tab. 3.5 remains consistent.

One may note that a phase found previously on smaller clusters is missing. Indeed, triplet f -wave superconductivity could not be stabilized on the 7-site cluster at van Hove filling. It is notable that f -wave superconductivity is established for lower fillings than approximately 1.4 electrons per site and again for fillings larger than 1.6 electrons per site, which means at fillings approximately 0.1 electrons per site away from van Hove filling. This is in accordance to renormalization group studies by Kiesel *et al.* [76], pictured in Fig. 3.10. Whether f -wave superconductivity really becomes the supported ground state at fillings away from $3/4$ filling remains to be studied.

The behavior of the respective superconducting phases around van Hove filling is

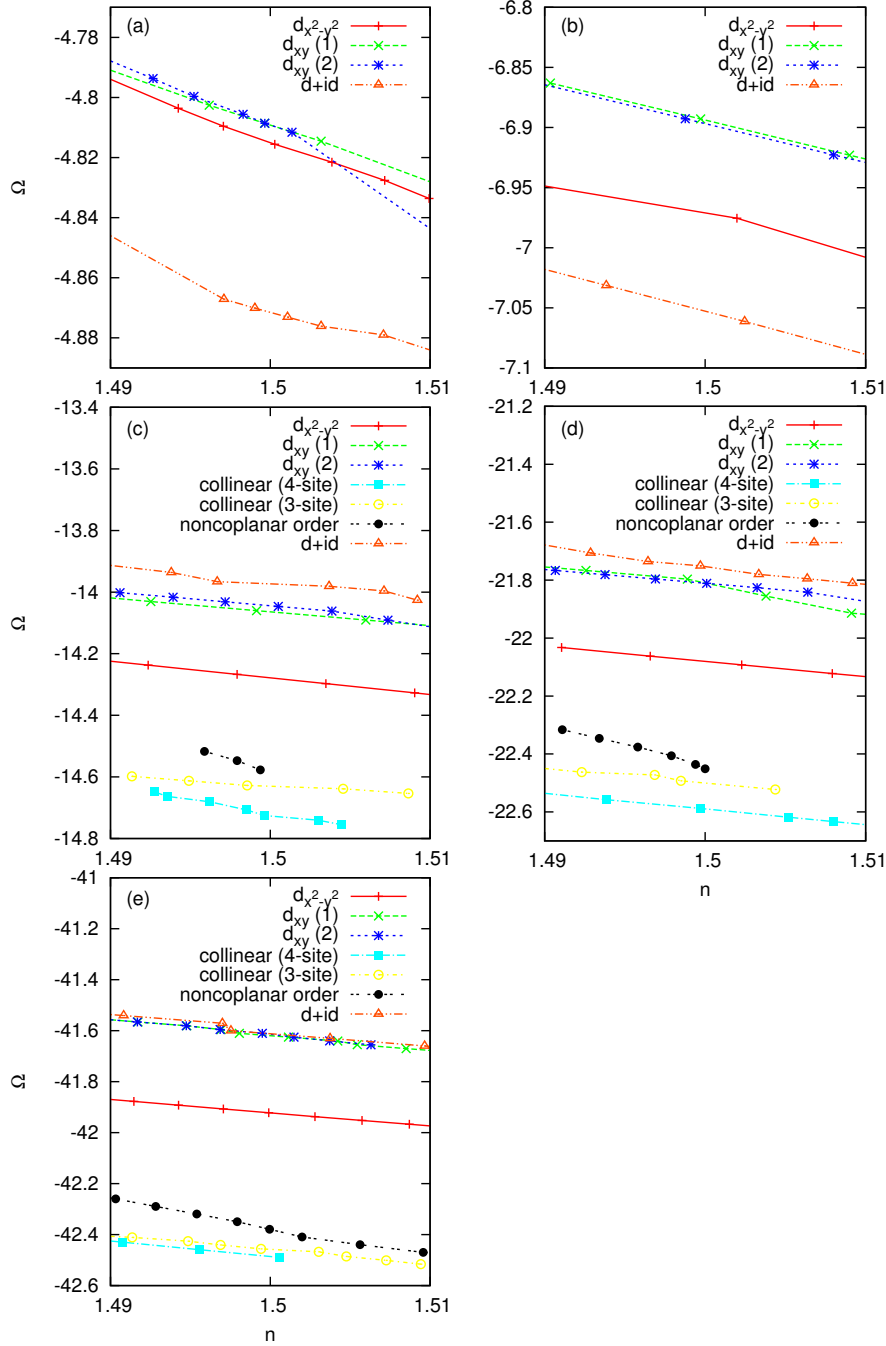


Figure 3.22: The grand potential Ω as function of the doping n around the van Hove filling for (a) $U=1$, (b) $U=4$, (c) $U=12$, (d) $U=20$, and (e) $U=40$ for superconducting phases on the 7-site cluster given in Fig. 3.16(b). The results for the SDW phases included in (c), (d) and (e) originate from the 12-site cluster given in Fig. 3.16(e)

plotted in Fig. 3.22. In the regime of weak coupling at $U = 1$ (Fig. 3.22(a)) the strong tendency of the system towards chiral $d + id$ -wave superconductivity can be seen as well as the degeneracy of the other d -wave states at larger values of the grand potential. A similar picture arises at $U = 4$ (Fig. 3.22(b)), but the $d_{x^2-y^2}$ -wave phase is now lowered in energy, compared to the phases with d_{xy} -wave symmetry.

The diagrams at stronger couplings of $U = 12$ (Fig. 3.22(c)), $U = 20$ (Fig. 3.22(d)) and $U = 40$ (Fig. 3.22(e)) additionally include the results for the SDW phases calculated in Sec. 3.4.1. Since these results were obtained using a 12-site cluster, one may argue whether a comparison of these results with the results of superconducting phases on a 7-site cluster is reasonable. A justification of this proceeding will be given in Sec. 3.4.7, where the energies of disordered phases on different cluster sizes are compared.

Comparing the values of the grand potentials of the respective phases yields the conclusion that for strong repulsions with $U \geq 12$ SDW phases are preferred, as becomes visible in Fig. 3.22(c) for $U = 12$, Fig. 3.22(d) for $U = 20$ and Fig. 3.22(e) for $U = 40$. The difference in the grand potentials is quite large, preferring SDW quite clearly to superconductivity. As discussed in Sec. 3.4.1, collinear SDW phases exhibit lower values of the grand potential than the noncoplanar phase, resulting in a ground state described by the four-sublattice collinear phase pictured in Fig. 3.7, although the energy difference to a slightly disfavored collinear phase with a tripled unit cell (see Fig. 3.15(c)) is very small.

Including SDW phases to the results for superconducting phases therefore delivers the much more reasonable result of a SDW ground state in the regime of strong interactions, as opposed to the previous result of a superconducting ground state with $d_{x^2-y^2}$ -wave symmetry, which arises from an unphysical nondegeneracy of the d -wave phases at increased interactions.

The results in Fig. 3.22 indicate a transition from chiral $d + id$ -wave superconductivity into a SDW state with collinear, nonuniform spin moments and a quadrupled unit cell. This transition has to occur somewhere between $U = 4$ and $U = 12$, in a regime of intermediate interactions. This regime is quite difficult to access with the VCA because strong nonlocal fluctuations might occur, which exceed the cluster size and are therefore not included within the theory. Results obtained in the corresponding regime are therefore rather unreliable and should be treated with caution.

3.4.5 Properties of the SDW Phases

The unique properties of the respective SDW phases have already been discussed in Sec. 3.2.1. Using the VCA allows a calculation of the spectral function from the imaginary part of the Green function

$$A(\mathbf{k}, \omega) = \lim_{\eta \rightarrow 0^+} -2 \operatorname{Im} G(\mathbf{k}, \omega + i\eta). \quad (3.15)$$

With the help of this information other one-particle properties can be treated, like a calculation of the Fermi surface or the density of states. Using these methods allows a characterization of the respective phase, for example concerning the energetic structure around the Fermi surface and the formation of gap structures.

The noncoplanar SDW from Fig. 3.6 breaks time-reversal symmetry and exhibits spontaneous quantum Hall effect, it opens a complete gap at the Fermi surface to become a spontaneous quantum Hall insulator [63], whereas collinear SDW phases might open a gap only for one spin channel and exhibit a metallic behavior in the other channel [60].

Figure 3.23 shows the spectral function for a path through the Brillouin zone including two inequivalent M points for the collinear phase with a tripled unit cell for large Coulomb interactions of $U = 40$. In this regime, collinear SDW phases are found to be preferred over other phases like noncoplanar SDW or superconductivity, see Fig. 3.22. The two channels for spin-up and spin-down electrons are printed separately in Fig. 3.23(a) and Fig. 3.23(b). While the spin branch in Fig. 3.23(a) most likely exhibits metallic behavior by not opening a gap at the Fermi energy at $\omega - \mu = 0$, the other spin branch indeed does open a gap, which is visible in Fig. 3.23(b) at the Fermi level. One may note that the quality of the band structure figures is not the best and many small gaps occur, which split up the original bands and might overstrike physical effects. This behavior is generated by finite-size effects that especially occur at strong interactions on small systems. Since the system size is limited by the VCA, these effects cannot be turned off. One might reduce them by introducing a finite linewidth but important effects might be smeared out if this parameter is chosen too large.

A more convincing insight into the gap structure of the respective spin branches of

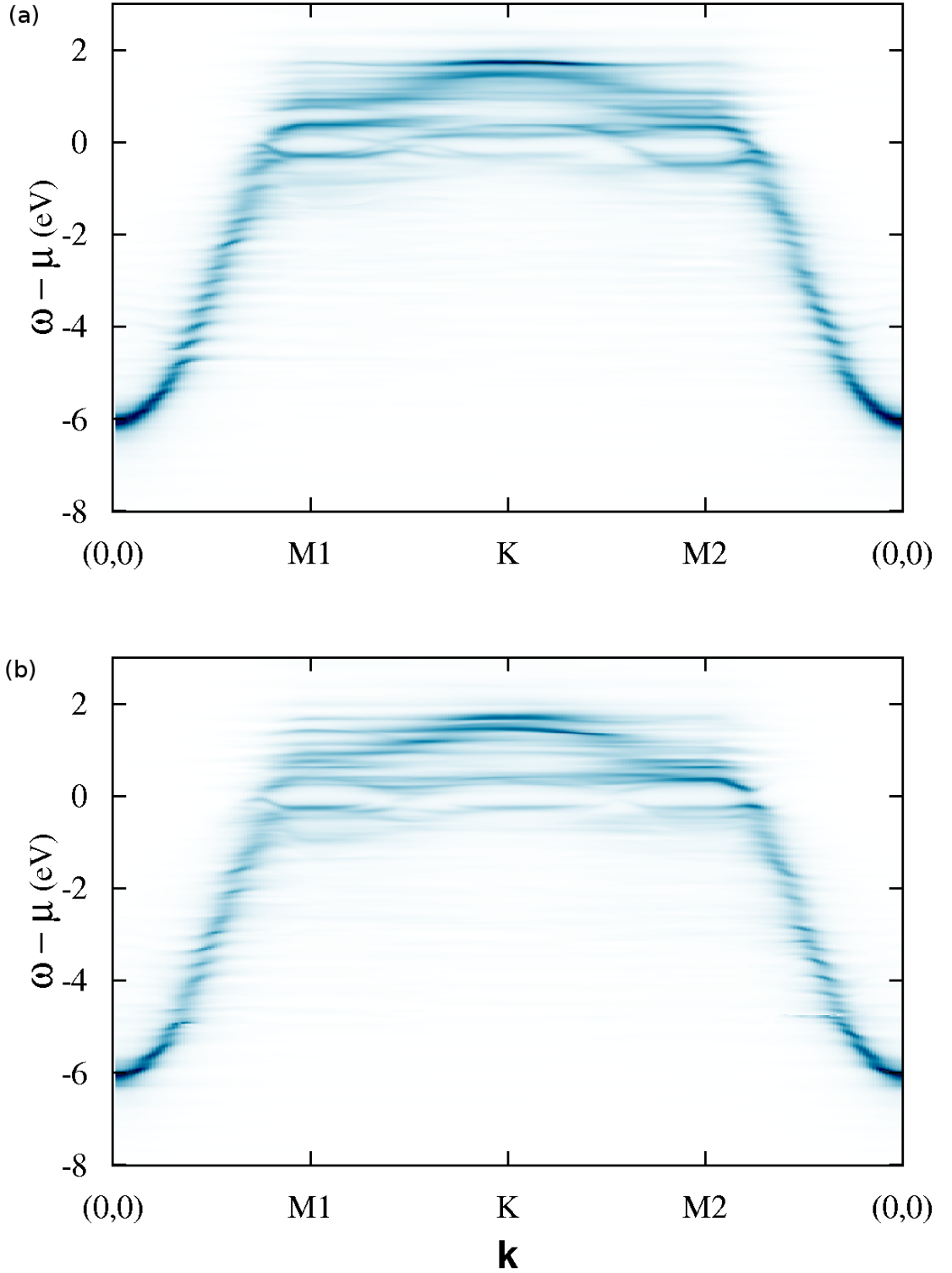


Figure 3.23: Spin resolved spectral function of the upper Hubbard band of the collinear phase from Fig. 3.15(c) at van Hove filling. The metallic spin branch is shown in (a), while a gap at the Fermi level is observed for the other spin branch (b). Note that large on-site interactions ($U = 40$) cause visible finite size effects.

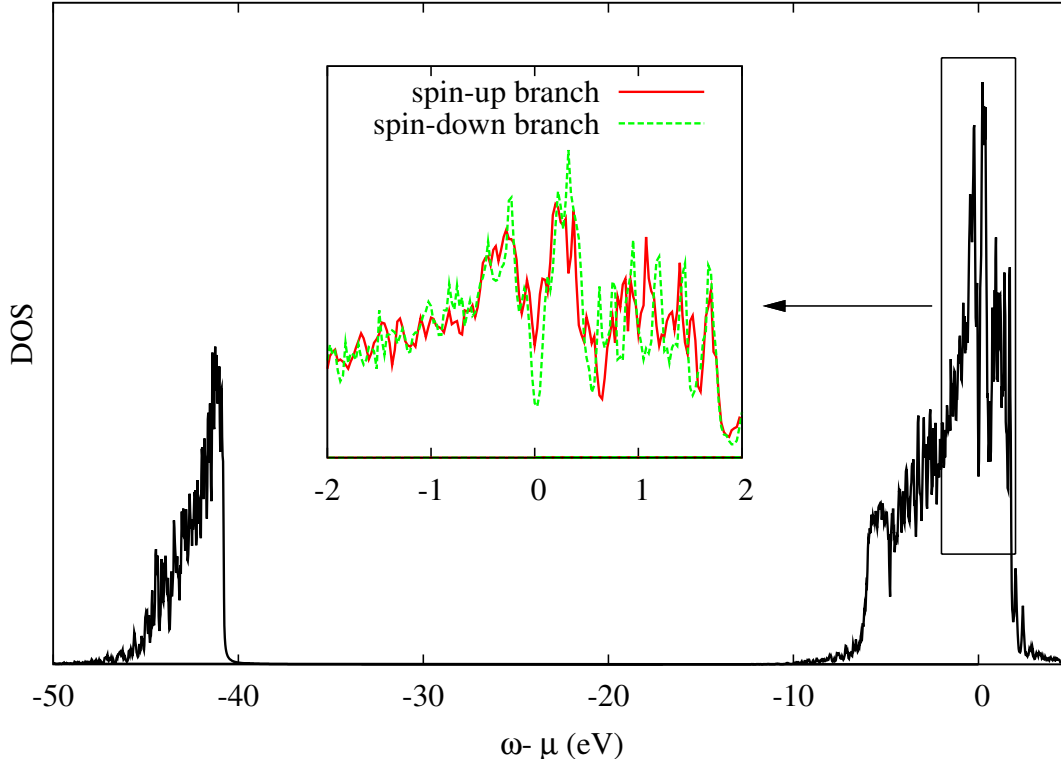


Figure 3.24: Density of states of the 3-site collinear phase (see Fig. 3.15(c)) for $U = 40$. Inset: Extract of the density of states (separated for the two spin branches) around the Fermi energy. The spin-up branch forms a gap at the Fermi energy whereas the spin-down branch is not gapped out. Note that finite line broadening was used.

the 3-sublattice collinear SDW phase is given in Fig. 3.24. Here, the DOS of the same problem as in Fig. 3.23 has been plotted. Although in the overall spectrum of the DOS a dent is visible exactly at the Fermi level, a spin-resolved analysis of the DOS (see inset of Fig. 3.24) reveals the underlying character of the gap. While the spin-down branch (dotted green line) exhibits a pronounced dip at the Fermi level, which can be safely regarded as a gap broadened by the usage of a finite linewidth of 0.05 eV, the dent for the spin-up channel (red line) is much less pronounced. Therefore, the 3-sublattice collinear SDW phase is supposed to exhibit the properties of a half metal.

In contrast to the half-metal behavior of collinear SDW phases, the chiral SDW phase becomes a spontaneous quantum Hall insulator by the opening of a complete gap. This can be observed in the spectral function of the chiral phase in Fig. 3.25 in the strong coupling regime at $U = 40$. Despite considerable finite-size effects that disturb the band structure to some extent, the opening of a gap at the M points is clearly visible.

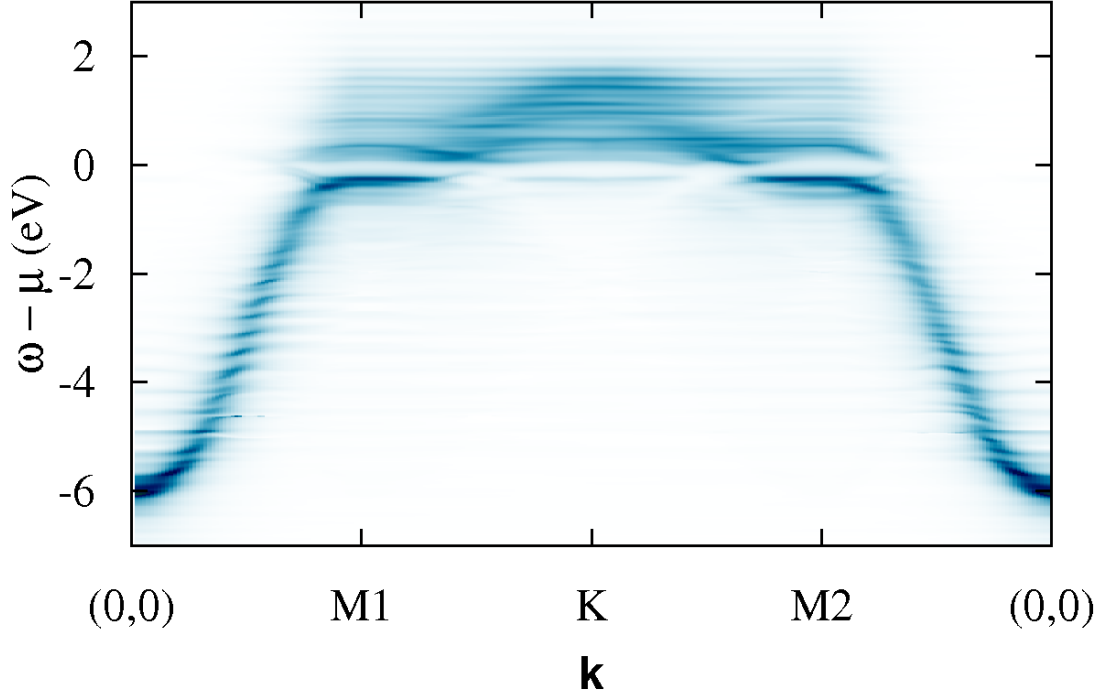


Figure 3.25: Spectral function $A(\omega, \mathbf{k})$ of the $3q$ noncoplanar phase from Fig. 3.6. The formation of a gap at the M points is visible.

Utilizing the DOS of the chiral SDW phase at $U = 40$ further supports the assumption that a full gap is established at the Fermi level of a $3/4$ filled system. The dent that is found in Fig. 3.26 in the overall DOS at the Fermi level turns out to be a full gap, with both spin channels showing the same behavior of gapping the Fermi surface out, as pictured in the inset of Fig. 3.26. Again, the usage of a finite linewidth prevents the DOS of really reaching zero at the position of the gap, but the results should be a convincing proof of the existence of the gap nevertheless. Additionally, studies of the Fermi surface revealed the Fermi surface to be empty, with gap sizes in the regime of approximately 0.1 eV. Since these gap sizes are in general one magnitude larger than the ones introduced by superconducting order parameters, this might explain the stability of SDW phases in comparison to superconducting phases in the regime of strong interactions.

The collinear SDW phase with a quadrupled unit cell (Fig. 3.7) exhibits a similar behavior like the one shown in Fig. 3.24 for the three-sublattice collinear SDW phase, with one spin branch gapped out, while the other spin branch remains metallic. The

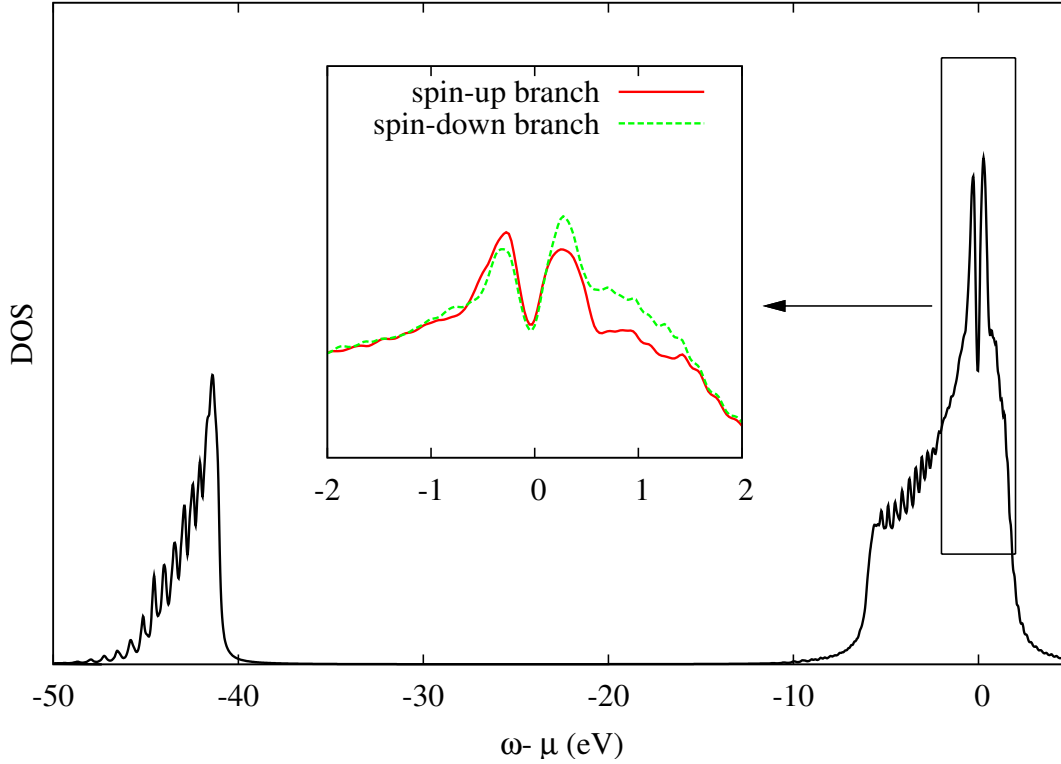


Figure 3.26: Density of states of the chiral SDW phase (see Fig. 3.6) for $U = 40$. Inset: Extract of the density of states (separated for the two spin branches) around the Fermi energy. In contrast to collinear SDW, a full gap opens for both spin branches.

collinear ‘stripe’ SDW phase (Fig 3.15(d)) on a bipartite lattice shows no differences in the respective spin channels. Here, the formation of a full gap is visible, as pictured in Fig. 3.26 for the chiral SDW phase.

3.4.6 Properties of the Superconducting Phases

Concerning the symmetry of the superconducting order parameters used (see Fig. 3.18) one expects different gap structures as some order parameters exhibit zeros along particular directions in the Brillouin zone and therefore preventing a gap to be established. This includes the two variations of d_{xy} -wave order parameters given in Fig. 3.18(b) and Fig. 3.18(c).

In Fig. 3.27 the spectral weight of all studied superconducting order parameters on the 7-site cluster is printed for $U = 4$ (left) and for the strongly interacting regime of $U = 40$ (right). Especially at strong interactions the development of a gap at only one M point is visible in Fig. 3.27(b) and Fig. 3.27(c) for d_{xy} -wave symmetry of the

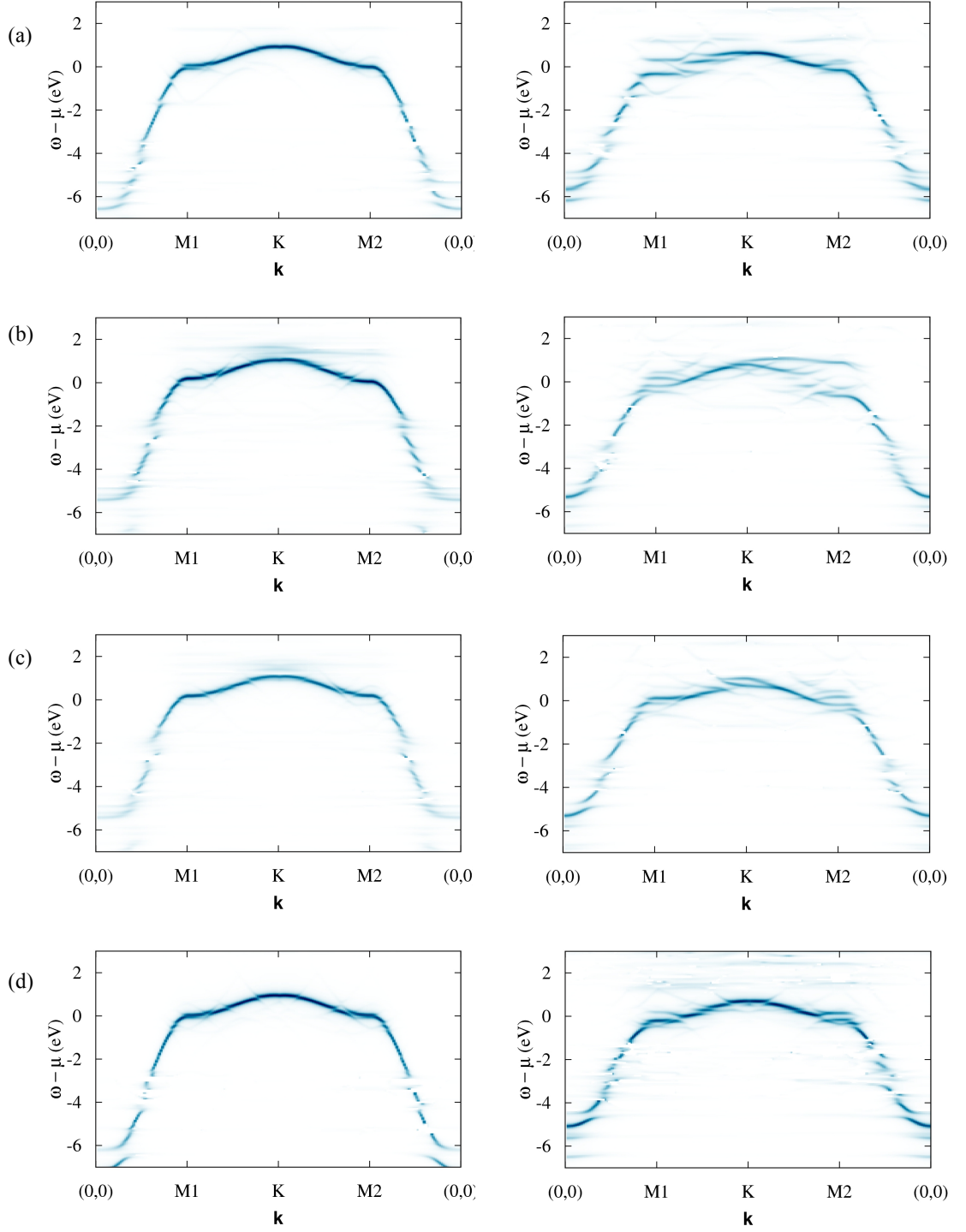


Figure 3.27: Spectral function $A(\omega, \mathbf{k})$ of different superconducting phases on the 7-site cluster for a path along the Brillouin zone including two M points at $U = 4$ (left) and $U = 40$ (right). (a) $d_{x^2-y^2}$ -wave superconductivity, (b) d_{xy} -wave superconductivity, (c) rotated d_{xy} -wave superconductivity, (d) $d + id$ -wave superconductivity.

superconducting order parameter, whereas a $d_{x^2-y^2}$ -wave order parameter seems to induce inequivalent gaps at both M points in Fig. 3.27(a), according to its symmetry.

A chiral superposition of $d_{x^2-y^2}$ and d_{xy} -wave order parameters leads to a symmetric behavior at both M points printed in Fig. 3.27(d). This phase opens a full, but small gap on the whole Fermi surface, which contributes to the lowering of the ground state energy of this phase. If it is supported at van Hove filling, also triplet f -wave superconductivity gaps out the Fermi surface entirely but on the 7-site cluster this phase does only exist at fillings slightly away from $3/4$ filling.

The effect on increased on-site interactions on the band structure in general can also be seen in Fig. 3.27. Small interactions of $U = 4$ lead only to finite-size effects far away from the Fermi energy, whereas large interactions of $U = 40$ generate considerable disruptions of the bands at all energies. Such a disruption might be situated at the Fermi level coincidentally, making a decision about gap sizes difficult in this regime. The usual gap size tends to be very small with values lower than 0.1 eV.

3.4.7 Effects of the Cluster Shape

Due to severe limitations in the choice of size and shape of the cluster the comparability between results originating from different clusters is difficult. However, since it is a main goal of this chapter to evaluate the ground state properties, taking both superconducting and magnetically ordered phases into account, it is important to find a method which allows a comparison of the studied phases.

Table 3.6: Calculated grand potentials Ω from VCA for disordered phases at different on-site interactions U for different cluster shapes pictured in Fig. 3.16 at $3/4$ filling. Hereby, the cluster labeled ‘8-site cluster (1)’ is shown in Fig. 3.16(d) and the one labeled ‘8-site cluster (2)’ is shown in Fig. 3.16(c).

U	4-site cluster	7-site cluster	8-site cl. (1)	8-site cl. (2)	12-site cluster
1	-4.852	-4.915	-4.836	-4.840	-4.818
4	-7.043	-6.861	-7.098	-7.139	-7.087
8	-11.157	-10.829	-10.769	-10.831	-10.718
12	-15.082	-14.786	-14.655	-14.704	-14.540
20	-22.980	-22.759	-22.545	-22.784	-22.418
40	-43.001	-42.721	-42.485	-42.745	-42.418

The search of a phase that can be equally established within arbitrary clusters leads to the disordered phase without any order parameters. In Tab. 3.6 the resulting values of the grand potential of the disordered phase are given for different cluster geometries at selected values of Coulomb interaction U . The clusters studied correspond to the ones that were used in the calculations determining the ground state energies of superconducting and SDW phases in the previous sections, shown in Fig. 3.16.

Because the VCA becomes exact in the limit of infinite cluster size, it is reasonable to assume that the quality of the results of the 12-site cluster is the best. Additionally, the 12-site cluster exhibits the largest scaling parameter $Q \approx 0.82$ of all clusters studied and its isotropy is good, concerning the number of bonds into the different spatial directions.

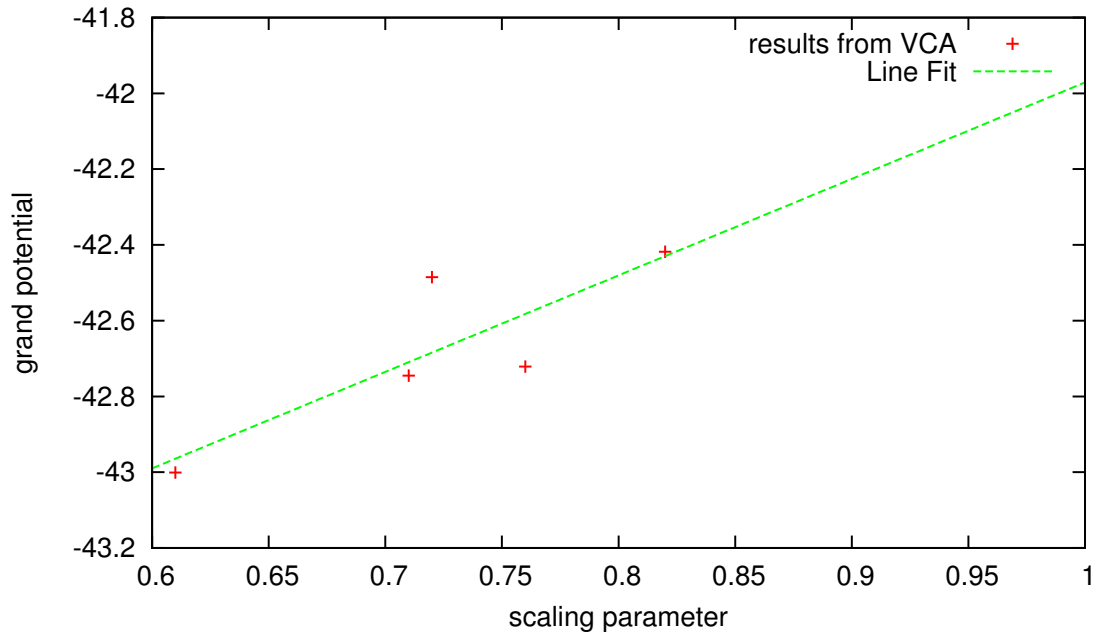


Figure 3.28: Finite-size scaling of the results obtained by VCA calculations for the disordered phase at $U = 40$. The results for the grand potential of the disordered phase on different clusters are plotted over the respective scaling parameter Q of the cluster, which describes the percentage of bonds that are treated nonperturbatively. A linear regression delivers $\Omega_\infty = -41.972$ for infinite cluster size at $Q = 1$.

As can be seen from Tab. 3.6, the grand potential of the disordered phase on the 12-site cluster is the highest of all cluster shapes in most cases. It seems therefore reasonable to assume that the finite-size effects lower the physical grand potential. To quantify this effect the results for the grand potential of the disordered phase at

$U = 40$ from Tab. 3.6 are plotted over the scaling parameter Q of the respective cluster in Fig. 3.28. On the basis of the available data points, the approximation of a linear dependence seems reasonable. A linear regression performed on the VCA values delivers a grand potential of $\Omega = -41.972$, if extrapolated towards the limit of infinite cluster size at $Q = 1$. Although such a regression is applicable in the regime of strong interactions, the behavior changes towards weak to intermediate couplings, where a linear behavior can hardly be found. Also, the discrepancies between the two 8-site clusters are unexpected because the results of the 2×4 cluster with larger anisotropies correspond much better to the results of the 12-site cluster.

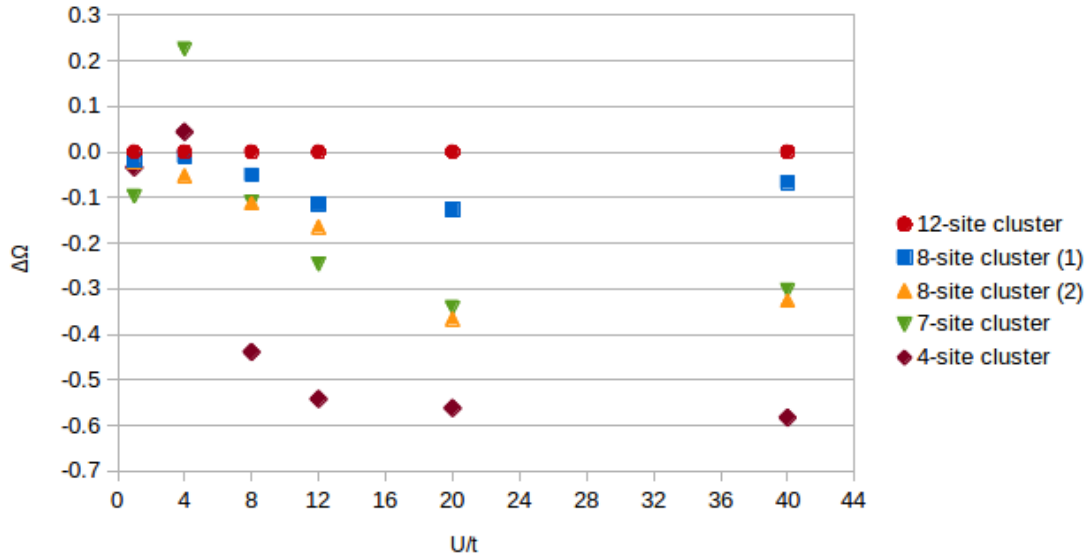


Figure 3.29: Comparison of the difference $\Delta\Omega = \Omega - \Omega_{12}$ of the grand potential Ω of disordered phases on the respective cluster with the grand potential of the disordered phase on the 12-site cluster Ω_{12} at several values of the Hubbard repulsion U .

To illustrate this effect, the difference in the grand potential of the disordered phase from the 12-site cluster with respect to the value obtained by using other clusters is plotted in Fig. 3.29. The dependence of the displacement of the ground state energy on the size and shape of the cluster is clearly visible. While the picture is coherent in the regime of strong interactions, where the difference of energies only varies slightly, a complex behavior is found at intermediate couplings of about $U = 4$ to $U = 8$. In this regime, the order of the respective grand potential is partially inverted with the results of the 4-site and 7-site cluster actually lying above the result of the 12-site cluster, indicating problems that might arise if different cluster shapes shall be compared in this regime. Towards weak interactions, naturally finite-size

effects become less important and the values of the grand potential depend only weakly on the cluster shape.

Despite the unexpected behavior at intermediate couplings, the most interesting feature of Fig. 3.29 is the obvious good quality of the results of the 2×4 cluster. As its results only differ slightly from the results of the 12-site cluster, it surprisingly beats the more symmetric 8-site cluster and the fully symmetric 7-site cluster significantly, although it has to be admitted that an implementation of ordered phases might raise the importance of cluster isotropy as can be seen in the results for superconducting d -wave order parameters on the respective clusters. Additionally, problems arise in the determination of the grand potential of the disordered phase on the 7-site cluster at weak couplings. Here, it is only possible to place either ten or eleven particles within the cluster, which corresponds to fillings of approximately $n = 0.714$ and $n = 0.786$ respectively. When studying superconducting phases, this shortcoming can be overcome by a particle-hole transformation in one spin channel and the variational optimization of the respective superconducting order parameter. Therefore, the results for the disordered phase on the 7-site cluster should be treated with caution.

The results of Fig. 3.29 might be used to ‘gauge’ the results of Fig. 3.22, where results of superconducting phases on a 7-site cluster were compared with SDW phases on a 12-site cluster. According to Tab. 3.6, the grand potential of the disordered phase on the 7-site cluster lies approximately 0.3 below the grand potential of the same phase on the 12-site cluster for strong interactions of $U = 12$ to $U = 40$, which means that in a combined picture like in Fig. 3.22, the SDW-phases should be shifted downwards by this amount to obtain a comprehensive picture. Indeed, this only strengthens the stability of the SDW phases over the superconducting states even further and supports the results pictured in Fig. 3.22.

If one compares the ground state energies of the disordered phase from Tab. 3.6 with the energies of the calculated superconducting and SDW phases, one recognizes that only few of the superconducting and SDW phases are preferred over the disordered state. For example, on the 4-site cluster only f -wave superconductivity at weak couplings of $U = 1$ and $U = 4$ remains stable, while it survives on the 8-site cluster from Fig. 3.16(d) up to $U = 12$. On the 2×4 cluster, f -wave superconductivity is actually stabilized even at strong interactions of $U = 40$. In the considered regime of strong couplings beginning at $U = 12$, all collinear SDW phases are sup-

ported and therefore remain probable ground state candidates on the 12-site cluster.

3.5 Conclusions

In this chapter the ground state properties of a triangular lattice at van Hove filling have been studied using the VCA on various cluster shapes. Superconducting phases as well as SDW phases have been taken into account over a wide range of interaction strengths. Due to limitations of ED, arising finite-size effects on different cluster sizes complicate a comparison of results originating from different clusters. Measuring the grand potential of a disordered phase without the application of an order parameter allows a comparison of the results. Whereas the system selects a time-reversal symmetry-breaking chiral $d + id$ -wave superconducting phase in the regime of weak-coupling, a transition into a collinear SDW state occurs somewhere at intermediate to strong couplings. In this regime the exact behavior of the system at a possible transition cannot be determined within the VCA because results of intermediate couplings are inconsistent.

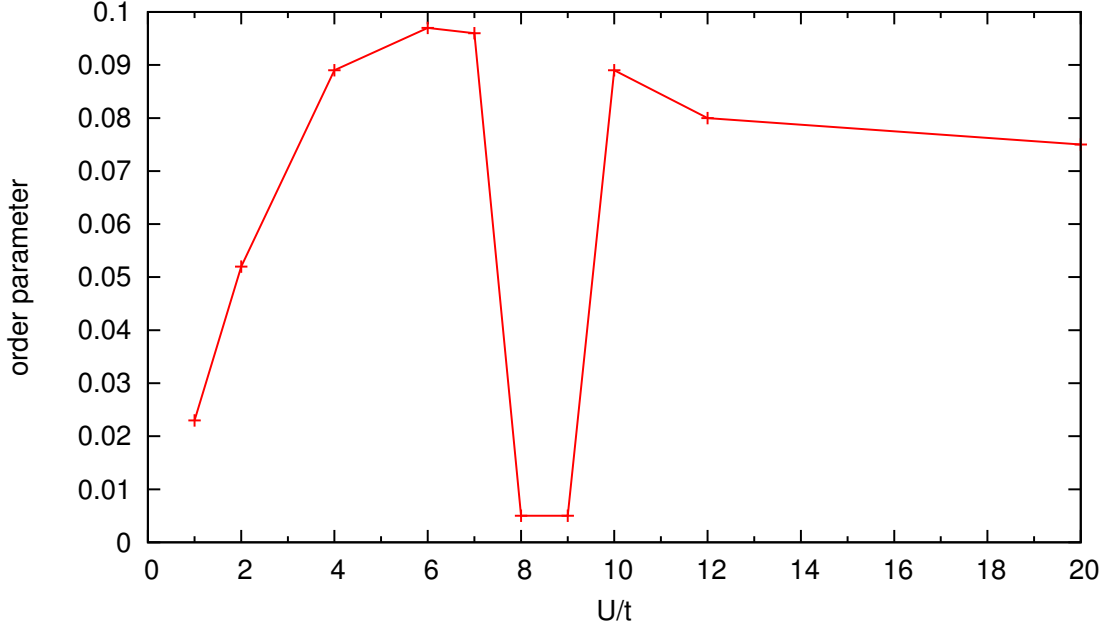


Figure 3.30: Behavior of the order parameter of the 4-sublattice collinear SDW phase on the 12-site cluster at van Hove filling in dependence of Hubbard repulsion U .

Figure 3.30 illustrates the behavior of the order parameter of the collinear SDW phase with quadrupled unit cell in dependence of the strength of the interaction

U on the 12 site cluster. The 4-sublattice collinear phase is chosen as an example because it exhibits the lowest grand potential of all SDW phases and is therefore the best candidate for the ground state. While its order parameter vanishes in the noninteracting limit and reaches a constant value towards strong interactions, its behavior in the regime of intermediate couplings between $U = 4$ and $U = 10$ is rather uncontrolled. While the collinear order parameter reaches its highest value at approximately $U = 6$, it suddenly becomes almost suppressed at $U = 8$, where its value is found to be very close to zero. But with the Hubbard repulsion reaching $U = 10$ it almost returns to its original value. In this regime, the order parameter stabilizes and the collinear phase becomes the supported ground state, whereas in the regime of weak to medium interactions this cannot be guaranteed. For example, if the grand potential is compared at $U = 4$, the 4-sublattice collinear SDW phase exhibits the lowest overall value $\Omega = -7.182$, but after applying the gauge presented in Sec. 3.4.7 using Tab. 3.6 one finds that chiral $d + id$ -wave superconductivity originating from the 7-site cluster is preferred over SDW.

Therefore, a robust conclusion that can be drawn from the VCA is only possible away from intermediate couplings. In the regime of weak interactions SDW phases get suppressed by vanishing order parameters as pictured in Fig. 3.30 for the 4-sublattice collinear phase. Therefore, the grand potential of the respective SDW phase approaches the grand potential of the disordered phase, allowing superconducting phases to develop, whose order parameters are finite in the weak-coupling limit.

In the regime of strong interactions SDW phases exhibit stabilized order parameters and a considerable lower grand potential than superconducting phases. Here, collinear SDW phases are preferred over the noncoplanar phase and the supported ground state is the collinear phase with a quadrupled unit cell, shown in Fig. 3.7.

The schematic phase diagram in Fig. 3.31 shall summarize the results of this chapter. In the weak-coupling regime, up to at least $U = 4$, $d + id$ -wave superconductivity is found to be the supported ground state within the VCA, which is in accordance with other approaches like several renormalization group studies [59, 61, 78].

At strong interactions, beginning at least at $U = 12$, the results using the largest possible cluster size of 12 sites indicate the stability of SDW phases with the interesting result of collinear phases being preferred over a chiral phase. While the

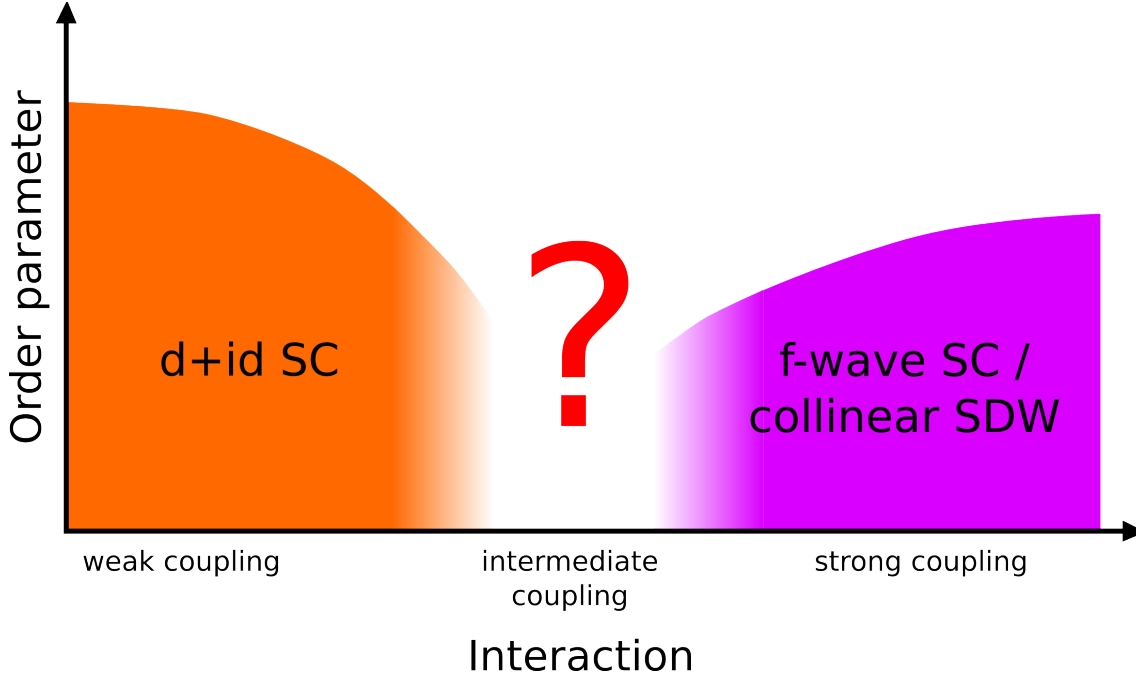


Figure 3.31: Schematic phase diagram of the triangular lattice at van Hove filling, based on the results obtained from different cluster geometries.

chiral wave opens a full gap at the Fermi level due to spontaneous quantum Hall effect, collinear phases open only a gap in one spin branch and should therefore be disfavored in energy. However, quantum spin fluctuations in the chiral phase might be the reason why collinear phases are preferred by the system [69]. The gap of the chiral phase is of the order of 0.1 eV, which is smaller than observed in mean-field calculations. Thus, it is easier for other effects like quantum fluctuations to become dominant.

SDW phases could not be stabilized using smaller clusters of 8 sites, where triplet f -wave superconductivity wins at strong interactions. Nevertheless, the formation of a SDW ground state might be the more likely scenario as f -wave superconductivity is usually found at fillings slightly away from $3/4$ filling, which is also the case for the results of the 7-site cluster.

At intermediate interactions the energy scales of superconducting phases and SDW phases get comparable and a clear distinction between different ground state scenarios is not possible as the behavior of several phases gets uncontrolled and different states may win, highly depending on finite size effects resulting from the cluster shape used. To gain more insight in this regime larger cluster sizes would be re-

quired, but as the effort increases exponentially in system size this might be hard to execute. Additionally, more cluster shapes could be studied using a mirror cluster approach [84], which allows to include a rotated mirror image of the original cluster to fill the 2D space properly. With this method it is possible to study for example highly symmetric triangular clusters with 3, 6, or 10 sites.

4 Breaking of Fourfold Lattice Symmetry in Iron-based Superconductors

The interest in iron-based superconductors arose in 2008 when superconductivity with a transition temperature of 26 K has been discovered in $\text{LaFeAsO}_{1-x}\text{F}_x$, where 11 percent of the oxygen were replaced by fluorine [85]. Under the application of pressure the critical temperature is even increased to 43 K. Subsequent studies by many groups found many iron-based superconductors with related crystal structures with transition temperatures reaching up to 56 K [86], which can be achieved by replacing the lanthanum in $\text{LaFeAsO}_{1-x}\text{F}_x$ by other rare earth elements such as neodymium or praseodymium.

Because of the large magnetic moment of iron and the strong ferromagnetic behavior of elemental iron, the discovery of superconductivity within these compounds was rather unexpected. Because it has previously been shown that magnetism disfavors superconductivity, iron has not been considered as a appropriate element to be used in the construction of new superconducting materials.

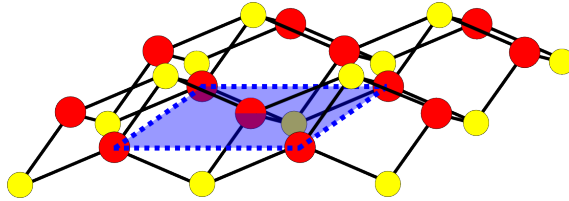


Figure 4.1: The active layer with iron cations in red and pnictogen/chalcogen anions in yellow. The dashed blue line indicates the two-iron unit cell resulting from the staggered arrangement of the anions.

Many different compounds have been found within the last years, whereas all iron-based superconductors share a similar structure consisting of quasi-two-dimensional active layers with a square lattice of iron atoms and tetrahedrally coordinated anions, such as P, As (pnictogens) or S, Se, or Te (chalcogens). These anions are placed alternately above and below the plane of iron atoms, doubling the size of the unit cell. The FeAs layer is shown in Fig. 4.1 with iron shown in red and

the anions shown in yellow. The interactions within this active layer are believed to be the driving force in the high T_c superconducting properties of this materials class.

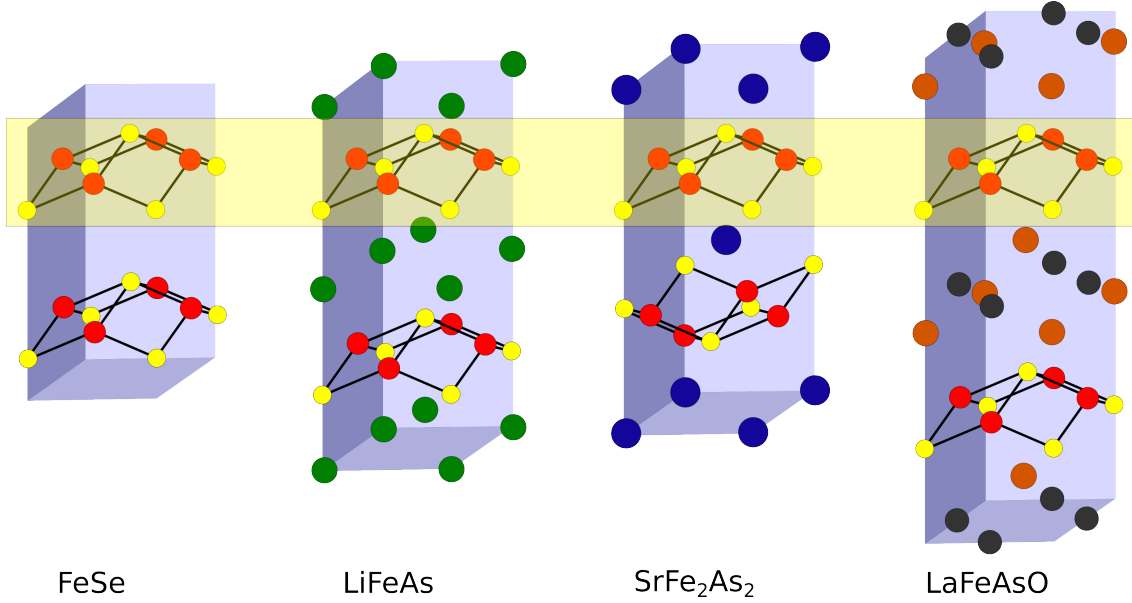


Figure 4.2: Crystallographic structure of selected iron-based superconductors with tetragonal unit cell. One active FeAs plane is highlighted. FeSe is an example for the so-called 11 type, whereas LiFeAs belongs to the 111 type, SrFe₂As₂ belongs to the 122 type and LaFeAsO belongs to the 1111 type.

Four of the tetragonal structures that exhibit superconducting properties are shown in Fig. 4.2. In FeSe, the active iron layers are simply stacked above each other, while in other compounds blocking layers separate the active planes and enhance the two-dimensional character of the system by coupling to the active layer with weak ionic bonds, whereas the intra-layer bonding between Fe and As is of strong covalent character. Such a blocking layer can consist of alkali (like lithium in LiFeAs), alkaline-earth (like strontium in SrFe₂As₂), rare-earth oxide (like LaO in LaFeAsO), rare-earth fluoride or perovskite-type structures.

In this chapter the interplay of onsite Coulomb repulsion and various mechanisms breaking the fourfold lattice symmetry for the iron planes of iron-based superconductors will be investigated using a multiband Hubbard model. Using CPT allows a local breaking of the symmetry between the x and y directions without imposing long-range magnetic order. The signatures of three different symmetry-breaking mechanisms - anisotropic magnetic couplings, an orbital ordering field and anisotropic hoppings - are compared and their features are evaluated. The results

of this chapter are published in [87].

4.1 Introduction: The Nematic Phase of Iron Pnictides

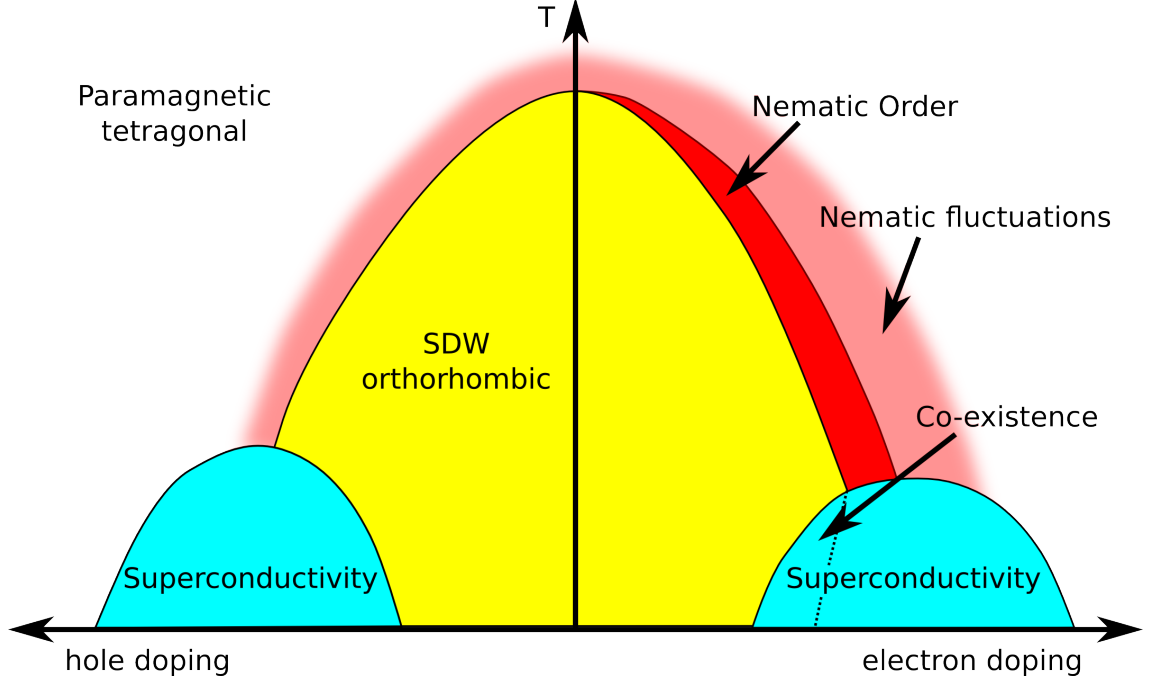


Figure 4.3: Schematic phase diagram of iron-based superconductors. The parent materials exhibit a SDW wave ground state with a stripe order shown in Fig. 4.4. The application of chemical substitution or external pressure can turn the system from SDW to a superconducting state. It is possible that a structural phase transition from a tetragonal to an orthorhombic phase occurs at slightly higher temperatures than the magnetic transition, forming a nematic phase. Nematic fluctuations may reach into the tetragonal phase.

At first sight, the phase diagram of iron-based superconductors is similar to the one of copper-based superconductors, which is still the materials class with the highest T_c , but their uniqueness in terms of the close neighborhood of magnetism and high- T_c superconductivity has been softened by the discovery of the iron pnictides and iron chalcogenides [88]. A schematic phase diagram of the iron-based superconductors is given in Fig. 4.3. It differs from the one of the cuprates mainly in the type of magnetic order at low dopings. While cuprates exhibit conventional antiferromagnetism, the spins on the iron sites in iron-based superconductors order in a stripe-type phase with ferromagnetic alignment in one direction and antiferromagnetic in the other as shown in Fig. 4.4. It is believed that the same magnetic interactions that are responsible for the formation of the SDW state might also be

a driving force for the superconducting pairing [89].

The parent compounds show metallic behavior in the SDW phase, whereas cuprates are Mott insulators. The superconducting dome is usually reached by chemical substitution of components of the parent compound, but it can also be reached by the application of external pressure. In contrast to the cuprates a chemical substitution is also possible within the active layer.

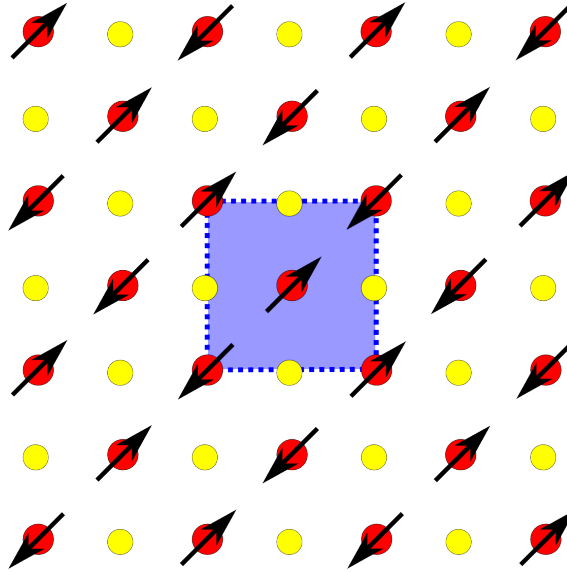


Figure 4.4: Spin arrangement on the iron sites in the FeAs layer. This stripe-type phase exhibits ferromagnetic interactions into one direction of nearest neighbors and antiferromagnetic interactions into the other direction. The two-iron unit cell is marked in blue.

The electronic structure of iron-based superconductors is dominated by the interplay of magnetic and electronic interactions. Within the active FeAs layer iron d orbitals are hybridized with arsenic p orbitals, leading to the formation of a metallic state. The main contribution to the DOS originates from the Fe d orbitals [90]. The two-dimensional character of the system is enhanced by different blocking layers, pictured in Fig. 4.2.

The resulting Fermi surface is crossed by at least four bands which mainly result from d_{xz} and d_{yz} of the iron square lattice [91], provided that the iron plane lies in the x - y plane. Here, two hole-like bands are centered around the Γ point at $\mathbf{k} = (0, 0)$ and two electronic bands are found at $(\pi, 0)$ and $(0, \pi)$ in the one iron unit cell. The staggered alignment of the pnictides/chalcogenides leads to an enlarged unit cell that contains two iron atoms. In the corresponding FS the electronic bands are shifted

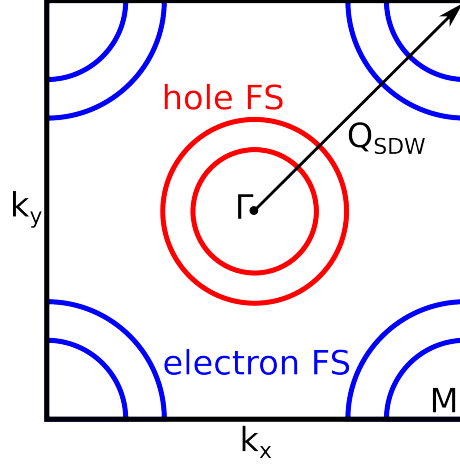


Figure 4.5: Schematic Fermi surface of iron-based superconductors. Multiple bands with hole-like character around the Γ point and electronic character around the M points cross the Fermi energy. These bands are dominated by iron d orbitals out of the active layer. $\mathbf{Q} = (\pi, \pi)$ denotes the nesting vector.

towards the corners at (π, π) as pictured in Fig. 4.5. This general structure of the FS has been confirmed in angle-resolved photoemission spectroscopy (ARPES) [92–94]. Depending on the compound the FS may exhibit a significant k_z dispersion, signaling a three-dimensional character of the sample. These three-dimensional effects may be important in the description of magnetism and superconductivity within the iron-based superconductors.

The structure of the FS in Fig. 4.5 allows nesting between the FS pockets mediated by a large but commensurate nesting vector $\mathbf{Q} = (\pi, \pi)$. In a picture of itinerant electrons this explains the instability of the FS towards SDW order.

A detailed examination of the phase diagram of iron-based superconductors reveals another phase in close proximity to the SDW state. At temperatures slightly above the onset of magnetic order $T_{\text{nem}} > T_N$ the system might spontaneously break the lattice symmetry within the iron plane. The structural distortion between the x and the y direction drives the tetragonal unit cell towards an orthorhombic unit cell while preserving time-reversal symmetry [95]. This structural transition with $T_{\text{nem}} > T_N$ is of second order in several materials like electron-doped $\text{Ba}(\text{Fe}_{1-x}\text{Co}_x)_2\text{As}_2$ [96–98], whereas it may also occur precisely at the onset of magnetic order at $T_{\text{nem}} = T_N$ to form a first-order phase transition, for example in hole-doped $(\text{Ba}_{1-x}\text{K}_x)\text{Fe}_2\text{As}_2$ [99].

This orthorhombic state with a broken lattice symmetry while time-reversal sym-

metry is preserved is called a *nematic* phase [100, 101]. Here, the corresponding order parameter points either along the x or y direction, but long-range order is not yet established [102–104]. Because only these two directions are allowed the phase is also called Ising-nematic order.

Several transport experiments found strong anisotropies of electronic properties within the orthorhombic phase, indicating that the phase transition from the tetragonal into the orthorhombic state is not a regular phase transition. For example, the resistivity anisotropy measured is much larger as can be explained with the small lattice anisotropy of the orthorhombic phase [105, 106]. This leads to the conclusion that the phase transition is not purely driven by phonons [107], but electronic degrees of freedom might become important and probably the same fluctuations that are responsible for the SDW order (and potentially also the superconducting pairing) are driving the transition into the nematic phase [102, 103, 108].

Beside the resistivity anisotropy, other properties like thermopower [109] and optical conductivity [110–112] are found to exhibit anisotropies that are larger than can be explained by a phonon-driven phase transition. Using optical methods the anisotropies observed can reach energy differences of several hundred meV. ARPES allows insight into the splitting of the onsite energies of the d_{xz} and d_{yz} Fe orbitals [113–116] within the nematic phase, indicating orbital ordering. Additional symmetry breaking in the spin degrees of freedom is observed with torque magnetometry [98] and magnetic anisotropies are visible with nuclear magnetic resonance (NMR) [117]. Using scanning tunneling microscopy (STM) a dimerization of the structure in the SDW phase can also be observed above the onset of magnetic order [118].

One central question is now to clarify the nature of the fluctuations, which means in general the ability to distinguish between orbital fluctuations and spin fluctuations. The underlying mechanism that drives the fluctuations is essential for the development of superconductivity within these correlated-electron systems as they lead to different symmetries of the order parameter in the superconducting phase. Orbital fluctuations support s^{++} -wave symmetry with an isotropic gap structure, whereas spin fluctuations favor a superconducting state with a nodal structure and a sign change of the gap function, for example a s^{+-} -wave or d -wave superconducting phase [95, 119].

Within the nematic phase three different order parameters are finite and it is a

challenging task to identify the leading instability which drives the phase transition. Beside the structural distortion with inequivalent lattice parameters along the x and y direction, the occupations and onsite energies of the d_{xz} and d_{yz} Fe orbitals become inequivalent [96, 120–122], a scenario named *orbital order*. Additionally, also the static spin susceptibility $\chi_{\text{mag}}(\mathbf{q})$ is inequivalent in q_x and q_y directions [98].

The assumption that ψ_1 is the leading of the three order parameters ψ_i allows to write the Landau free energy as [95]

$$F[\psi_1, \psi_2, \psi_3] = \frac{1}{2}\chi_1^{-1}\psi_1^2 + \frac{b}{4}\psi_1^4 + \lambda_{12}\psi_1\psi_2 + \frac{1}{2}\chi_2^{-1}\psi_2^2 + \lambda_{13}\psi_1\psi_3 + \frac{1}{2}\chi_3^{-1}\psi_3^2 + \dots \quad (4.1)$$

Here, χ_i^{-1} donate the inverse susceptibility or the respective order parameter ψ_i and λ_{ij} are coupling constants between different order parameters. At $T < T_{\text{nem}}$, ψ_1 orders with $\langle\psi_1\rangle = \pm(-\chi_1^{-1}/b)^{1/2}$ and χ_1^{-1} becomes negative. At the same point, also ψ_2 and ψ_3 order, assuming λ_{12} and λ_{13} to be nonzero. A decision, which of the three mechanisms is the driving force, is therefore not possible within the picture of equilibrium order parameters.

Experimental approaches additionally suffer from the formation of twin domains within the nematic phase, which lead to a vanishing average value of the order parameter. By the application of uniaxial stress [105, 106] or by the application of an external magnetic field [123] to break the tetragonal symmetry this problem can be solved by detwinning the crystal.

4.2 Model and Method

Since the structural transition at temperatures slightly above the onset of magnetic order is accompanied by an additional symmetry breaking of the electronic degrees of freedom, a decision between the distinct scenarios remains difficult. For example, a breaking of the orbital symmetry or the formation of a nematic phase of the spin degree of freedom, where the preferred order parameter is already selected between $\mathbf{Q} = (0, \pi)$ and $\mathbf{Q} = (\pi, 0)$, but long-range magnetic order has not been established. Nevertheless, an identification of the driving force within the nematic phase is desired as it could clarify central questions concerning iron-based superconductors, or correlated-electron systems in general. For example, the symmetry of the superconducting gap function highly depends on the orbital or spin character of the dominant

fluctuations.

As soon as one of the scenarios breaks rotational symmetry of the lattice, the symmetry of the other degrees of freedom will be broken as well because lattice [104, 124, 125] and orbital [120] degrees of freedom strongly interact with the spin. Nevertheless, a characterization of the main signatures of the different symmetry-breaking mechanisms may be useful to elucidate the most important effects.

CPT is used to be able to locally break the fourfold rotational symmetry by including short-range anisotropic AFM interactions within the cluster without imposing long-range order [126]. Hereby, the biggest drawback of cluster methods like CPT or VCA actually turns into an advantage. While correlations are only treated on an accurate level within the cluster by ED, long-ranged effects are treated on the mean-field level. As a result, a locally broken symmetry within a cluster does not impose a long-range ordered field.

To reproduce the ARPES results [114–116], which show a momentum dependent shifting of the bands with d_{xz} and d_{yz} character, additional scenarios are studied, for example by the inclusion of an orbital ordering field or the application of anisotropic hoppings. The spectral weight $A(\mathbf{k}, \omega)$ is calculated using Eq. (3.15), which connects the one-particle spectral function to the imaginary part of the Green function and therefore allows a direct comparison of the calculated results with ARPES measurements.

Due to the limitations of ED concerning the systems size the desire to study at least 4-site square clusters prohibits the usage of all Fe d bands. Although *ab initio* calculations found a strong hybridization of the five Fe $3d$ bands [127, 128], ARPES experiments found the Fermi surface of iron-based superconductors to be dominated by the d_{xz} and d_{yz} orbitals [129]. Such minimal two-band models were especially studied in the early days of the iron-based superconductors in 2008 [130–132]. Later studies argued that such a minimal model would miss important features [128, 133, 134]. For example, parts of the electron pockets of the Fermi surface are determined primarily by a band with d_{xy} character and the bands that produce the hole pockets are expected to be degenerate at the Γ point [135]. In a two-band model orbital both bands have to be half filled to reproduce the Fermi surface. In this situation any excitation would have to pay both U and J , which results in an almost complete suppression of orbital fluctuations [136].

Subsequently to the two-orbital model, models that include three [134, 135] and even four [126, 137] bands were proposed. A three-band model with 2/3 filling is used here, which allows orbital ordering effects to occur if the d_{xy} orbital is partially filled.

For the construction of the tight-binding Hamiltonian the Slater-Koster formalism [132, 138, 139] is applied. Since the three-band model is restricted to the Fe d_{xz} , d_{yz} and d_{xy} orbitals, their hybridization with the As p orbitals has to be included to estimate the amplitude of the hopping between iron sites. In the two-band model the Fe-As hopping integrals are used to calculate the Fe-Fe tight-binding hopping parameters [132]. To obtain a plausible Fermi surface, the hopping elements are fitted within the three-band model.

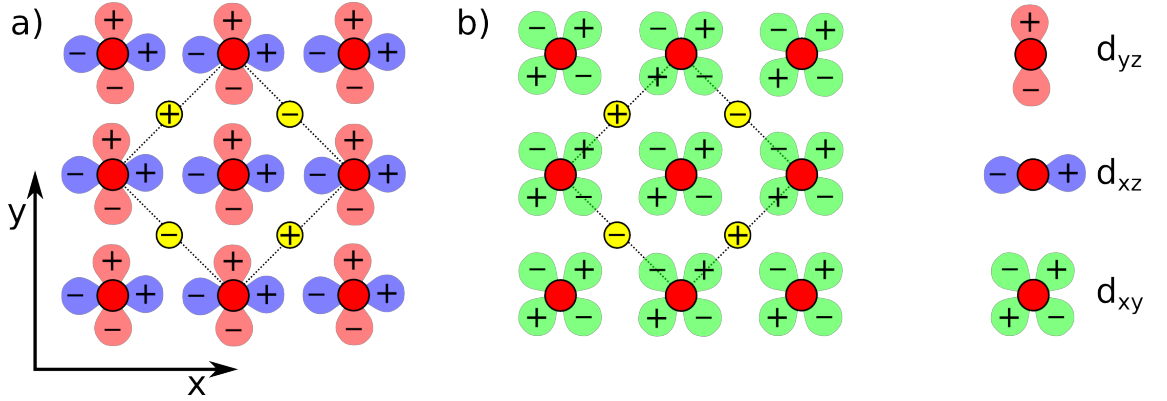


Figure 4.6: Top view of the iron 3d orbitals within the FeAs plane for (a) d_{xz} (red) and d_{yz} (blue) orbitals and (b) for $d_{x^2-y^2}$ orbitals (green). The sign \pm at the arsenic site (yellow) indicates the position of the arsenic atom with respect to the iron plane. Picture adapted from [134].

The three relevant iron d orbitals are shown in Fig. 4.6. Since the hopping is mainly mediated by the arsenic p orbitals, their symmetry has to be included and their contribution to the effective Fe-Fe hopping has to be evaluated. Due to the staggered alignment of the arsenic atoms their contributions are dependent from the relative position of the respective atom with respect to the iron plane. An additional contribution to the hopping amplitudes comes from direct Fe-Fe hopping.

Taking the effective Fe-Fe hoppings for nearest neighbors and next-nearest neighbors produces the tight-binding Hamiltonian for the d_{xz} and d_{yz} iron orbitals [135],

$$\begin{aligned}
 H^{xz,yz} = & -t_1 \sum_{\mathbf{i},\sigma} \left(d_{\mathbf{i},1,\sigma}^\dagger d_{\mathbf{i}+\hat{y},1,\sigma} + d_{\mathbf{i},2,\sigma}^\dagger d_{\mathbf{i}+\hat{x},2,\sigma} + \text{H.c.} \right) \\
 & -t_2 \sum_{\mathbf{i},\sigma} \left(d_{\mathbf{i},1,\sigma}^\dagger d_{\mathbf{i}+\hat{x},1,\sigma} + d_{\mathbf{i},2,\sigma}^\dagger d_{\mathbf{i}+\hat{y},2,\sigma} + \text{H.c.} \right) \\
 & -t_3 \sum_{\mathbf{i},\hat{\mu},\hat{\nu},\sigma} \left(d_{\mathbf{i},1,\sigma}^\dagger d_{\mathbf{i}+\hat{\mu}+\hat{\nu},1,\sigma} + d_{\mathbf{i},2,\sigma}^\dagger d_{\mathbf{i}+\hat{\mu}+\hat{\nu},2,\sigma} + \text{H.c.} \right) \\
 & +t_4 \sum_{\mathbf{i},\sigma} \left(d_{\mathbf{i},1,\sigma}^\dagger d_{\mathbf{i}+\hat{x}+\hat{y},2,\sigma} + d_{\mathbf{i},2,\sigma}^\dagger d_{\mathbf{i}+\hat{x}+\hat{y},1,\sigma} + \text{H.c.} \right) \\
 & -t_4 \sum_{\mathbf{i},\sigma} \left(d_{\mathbf{i},1,\sigma}^\dagger d_{\mathbf{i}+\hat{x}-\hat{y},2,\sigma} + d_{\mathbf{i},2,\sigma}^\dagger d_{\mathbf{i}+\hat{x}-\hat{y},1,\sigma} + \text{H.c.} \right) - \mu \sum_{\mathbf{i}} (n_{\mathbf{i},1} + n_{\mathbf{i},2}), \quad (4.2)
 \end{aligned}$$

where $d_{\mathbf{i},1,\sigma}^\dagger$ creates an electron at site \mathbf{i} with spin σ . The index $\alpha = 1$ between the spatial index and the spin index denotes the symmetry of the orbital. Here, ‘1’ indicates the d_{xz} orbital and ‘2’ indicates the d_{yz} orbital. Intraorbital hoppings are given by t_1 , t_2 and t_3 , whereas interorbital hoppings are denoted by t_4 . The chemical potential is determined by μ .

Up to this point, Eq. (4.2) describes a two-band model. An inclusion of a third orbital is needed to obtain accurate results as discussed previously. Including the d_{yx} orbital leads to additional terms. The additional intraorbital part of the d_{yx} orbital is given by

$$\begin{aligned}
 H^{xy} = & -t_5 \sum_{\mathbf{i},\hat{\mu},\sigma} \left(d_{\mathbf{i},3,\sigma}^\dagger d_{\mathbf{i}+\hat{\mu},3,\sigma} + \text{H.c.} \right) + t_6 \sum_{\mathbf{i},\hat{\mu},\hat{\nu},\sigma} \left(d_{\mathbf{i},3,\sigma}^\dagger d_{\mathbf{i}+\hat{\mu}+\hat{\nu},3,\sigma} + \text{H.c.} \right) \\
 & - \mu \sum_{\mathbf{i}} n_{\mathbf{i},3} + \Delta_{xy} \sum_{\mathbf{i}} n_{\mathbf{i},3}, \quad (4.3)
 \end{aligned}$$

where the index $\alpha = 3$ denotes the d_{xy} orbital and the energy difference between the d_{xy} orbital and the degenerate d_{xz} and d_{yz} orbitals is given by Δ_{xy} . The hybridization of the d_{xy} orbital with the other two orbitals is denoted by

$$\begin{aligned}
H^{xz,yz,xy} = & -t_7 \sum_{\mathbf{i},\sigma} \left[(-1)^{|\mathbf{i}|} d_{\mathbf{i},1,\sigma}^\dagger d_{\mathbf{i}+\hat{x},3,\sigma} + \text{H.c.} \right] - t_7 \sum_{\mathbf{i},\sigma} \left[(-1)^{|\mathbf{i}|} d_{\mathbf{i},3,\sigma}^\dagger d_{\mathbf{i}+\hat{x},1,\sigma} + \text{H.c.} \right] \\
& -t_7 \sum_{\mathbf{i},\sigma} \left[(-1)^{|\mathbf{i}|} d_{\mathbf{i},2,\sigma}^\dagger d_{\mathbf{i}+\hat{y},3,\sigma} + \text{H.c.} \right] - t_7 \sum_{\mathbf{i},\sigma} \left[(-1)^{|\mathbf{i}|} d_{\mathbf{i},3,\sigma}^\dagger d_{\mathbf{i}+\hat{y},2,\sigma} + \text{H.c.} \right] \\
& -t_8 \sum_{\mathbf{i},\sigma} \left[(-1)^{|\mathbf{i}|} d_{\mathbf{i},1,\sigma}^\dagger d_{\mathbf{i}+\hat{x}+\hat{y},3,\sigma} + \text{H.c.} \right] + t_8 \sum_{\mathbf{i},\sigma} \left[(-1)^{|\mathbf{i}|} d_{\mathbf{i},3,\sigma}^\dagger d_{\mathbf{i}+\hat{x}+\hat{y},1,\sigma} + \text{H.c.} \right] \\
& -t_8 \sum_{\mathbf{i},\sigma} \left[(-1)^{|\mathbf{i}|} d_{\mathbf{i},1,\sigma}^\dagger d_{\mathbf{i}+\hat{x}-\hat{y},3,\sigma} + \text{H.c.} \right] + t_8 \sum_{\mathbf{i},\sigma} \left[(-1)^{|\mathbf{i}|} d_{\mathbf{i},3,\sigma}^\dagger d_{\mathbf{i}+\hat{x}-\hat{y},1,\sigma} + \text{H.c.} \right] \\
& -t_8 \sum_{\mathbf{i},\sigma} \left[(-1)^{|\mathbf{i}|} d_{\mathbf{i},2,\sigma}^\dagger d_{\mathbf{i}+\hat{x}+\hat{y},3,\sigma} + \text{H.c.} \right] + t_8 \sum_{\mathbf{i},\sigma} \left[(-1)^{|\mathbf{i}|} d_{\mathbf{i},3,\sigma}^\dagger d_{\mathbf{i}+\hat{x}+\hat{y},2,\sigma} + \text{H.c.} \right] \\
& +t_8 \sum_{\mathbf{i},\sigma} \left[(-1)^{|\mathbf{i}|} d_{\mathbf{i},2,\sigma}^\dagger d_{\mathbf{i}+\hat{x}-\hat{y},3,\sigma} + \text{H.c.} \right] - t_8 \sum_{\mathbf{i},\sigma} \left[(-1)^{|\mathbf{i}|} d_{\mathbf{i},3,\sigma}^\dagger d_{\mathbf{i}+\hat{x}-\hat{y},2,\sigma} + \text{H.c.} \right].
\end{aligned} \tag{4.4}$$

The sign change denoted by $(-1)^{|\mathbf{i}|}$ results from the staggered arrangement of the arsenic atoms within the two-iron unit cell. Equations (4.2), (4.3), and (4.4) can be transformed into momentum space using

$$d_{\mathbf{k},\alpha,\sigma}^\dagger = \frac{1}{\sqrt{N}} \sum_{\mathbf{i}} e^{-i\mathbf{k}\mathbf{i}} d_{\mathbf{i},\alpha,\sigma}^\dagger, \tag{4.5}$$

with the wave vector \mathbf{k} and the number of sites N . As long as isolated planes are considered, an internal symmetry allows a transformation into a one-iron unit cell [134, 140], which corresponds to the representation of the tight-binding Hamiltonian in terms of the pseudo-crystal momentum $\tilde{\mathbf{k}}$. Hereby, the momentum of the d_{xy} orbital is shifted by $\tilde{\mathbf{k}} = \mathbf{k} + (\pi, \pi)$, which corresponds to the contribution originating from an enlarged one-iron unit cell. For the d_{xz} and d_{yz} orbitals $\tilde{\mathbf{k}} = \mathbf{k}$ remains true. Therefore, if results obtained within the picture of the pseudocrystal momentum $\tilde{\mathbf{k}}$ are compared to results with ‘lab-space’ momentum \mathbf{k} , contributions from d_{xy} , $d_{x^2-y^2}$ and $d_{3z^2-r^2}$ orbitals are shifted by (π, π) [122, 126, 141].

In real space the physics of the one-iron unit cell can be described by a local gauge transformation where orbitals with d_{xy} character gain a prefactor $(-1)^{|\mathbf{i}|}$ depending on the position of the orbital at site \mathbf{i} . This transformation leads to the Hamiltonian from Eq. (4.4) describing the hybridization of the d_{xy} orbital with d_{xz} and d_{yz} orbitals within the three-band model [126].

Switching from a two-iron unit cell to a one-iron unit cell has the additional ad-

vantage of allowing a distinction between momenta $(\pi, 0)$ and $(0, \pi)$ and therefore allowing a separated evaluation of the electronic properties at the X and Y points. In the two-iron unit cell both X and Y would map to (π, π) .

The momentum dependent tight-binding Hamiltonian in terms of the pseudo-crystal momentum can be written as

$$H_{\text{TB}}(\tilde{\mathbf{k}}) = \sum_{\tilde{\mathbf{k}}, \sigma, \mu, \nu} T^{\mu, \nu}(\tilde{\mathbf{k}}) d_{\tilde{\mathbf{k}}, \mu, \sigma}^\dagger d_{\tilde{\mathbf{k}}, \nu, \sigma}, \quad (4.6)$$

where electrons with pseudo-crystal momentum $\tilde{\mathbf{k}}$ and spin σ are annihilated (created) by $d_{\tilde{\mathbf{k}}, \mu, \sigma}$ ($d_{\tilde{\mathbf{k}}, \mu, \sigma}^\dagger$) in orbital μ . Since a three-band model is used the orbital indices μ and ν indicate the number of the orbital with d_{xz} , d_{yz} or d_{xy} symmetry. The hoppings are defined by $T^{\mu, \nu}(\tilde{\mathbf{k}})$ and are given by

$$T^{1,1/2,2} = 2t_{2/1} \cos k_x + 2t_{1/2} \cos k_y + 4t_3 \cos k_x \cos k_y \pm 2t_{11} [\cos(2k_x) - \cos(2k_y)] + 4t_{12} \cos(2k_x) \cos(2k_y), \quad (4.7)$$

$$T^{3,3} = \Delta_{xy} + 2t_5 (\cos k_x + \cos k_y) + 4t_6 \cos k_x \cos k_y + 2t_9 [\cos(2k_x) + \cos(2k_y)] + 4t_{10} [\cos(2k_x) \cos k_y + \cos k_x \cos(2k_y)], \quad (4.8)$$

$$T^{1,2} = T^{2,1} = 4t_4 \sin k_x \sin k_y, \quad (4.9)$$

$$T^{1,3} = \bar{T}^{3,1} = 2it_7 \sin k_x + 4it_8 \sin k_x \cos k_y, \quad (4.10)$$

$$T^{2,3} = \bar{T}^{3,2} = 2it_7 \sin k_y + 4it_8 \sin k_y \cos k_x, \quad (4.11)$$

where the hopping parameters are $t_1 = -0.08$, $t_2 = 0.1825$, $t_3 = 0.08375$, $t_4 = -0.03$, $t_5 = 0.15$, $t_6 = 0.15$, $t_7 = -0.12$, $t_8 = -t_7/2$, $t_{10} = -0.024$, $t_{11} = -0.01$, $t_{12} = 0.0275$ and $\Delta_{xy} = 0.75$ describes the difference of the energy of the d_{xy} orbital with respect to the d_{xz} and d_{yz} orbitals.

Within the three-band model the filling has to be re-defined as only three of the original five Fe 3d orbitals are used. Within low density approximation (LDA) calculations a filling of six electrons within all five d bands has been found. Filling the orbitals according to the crystal-field splitting, where the lowest-lying $d_{x^2-y^2}$ and $d_{3z^2-r^2}$ are completely filled, results in a filling of 1/3 of the remaining d_{xz} , d_{yz} and d_{xy} orbitals with two electrons in three orbitals [120, 135]. However, the Fermi surface obtained with this filling fraction does not reproduce the Fermi surface predicted by LDA calculations. To obtain similar results to LDA filling fractions above half filling (roughly two thirds) are needed [107, 135, 142]. For example, in a half

filled three-band model hole pockets arise at the \mathbf{M} points, which are not observed in the physical system [134], whereas at a filling fraction of $1/3$, the two almost degenerate hole pockets are not visible [135]. To obtain a filling fraction of $2/3$ with four electrons per site, $\mu = 0.47$ has been used.

Onsite Coulomb interactions [25, 26] are included by

$$H_{\text{int}} = U \sum_{\mathbf{i}, \alpha} n_{\mathbf{i}, \alpha, \uparrow} n_{\mathbf{i}, \alpha, \downarrow} + (U' - J/2) \sum_{\mathbf{i}, \alpha < \beta} n_{\mathbf{i}, \alpha} n_{\mathbf{i}, \beta} - 2J \sum_{\mathbf{i}, \alpha < \beta} \mathbf{S}_{\mathbf{i}, \alpha} \cdot \mathbf{S}_{\mathbf{i}, \beta} + J \sum_{\mathbf{i}, \alpha < \beta} (d_{\mathbf{i}, \alpha, \uparrow}^\dagger d_{\mathbf{i}, \alpha, \downarrow}^\dagger d_{\mathbf{i}, \beta, \downarrow} d_{\mathbf{i}, \beta, \uparrow} + \text{H.c.}), \quad (4.12)$$

where the intraorbital Coulomb repulsion U , the interorbital Coulomb repulsion U' , Hund's rule coupling J and pair hopping J' were used. The indices α and β denote the orbital and $\mathbf{S}_{\mathbf{i}, \alpha} = \frac{1}{2} \sum_{s, s'} d_{\mathbf{i}, \alpha, s}^\dagger \sigma_{s, s'} d_{\mathbf{i}, \alpha, s'}$ denotes the electron spin operator using the vector of Pauli matrices $\sigma = (\sigma^x, \sigma^y, \sigma^z)$. In principle, the couplings of the d_{xy} orbital can differ from the ones of d_{xz} and d_{yz} orbital, but they have been chosen to be the same for simplicity. Additionally, the relation $U = U' + 2J$ is applied due to rotational invariance and $J' = J$ is used [143].

The first two terms of Eq. (4.12) describe the energy cost of placing a second electron on an already occupied site in the same orbital (first term) and in different orbitals (second term). The third term describes the mechanism of Hund's rule coupling, favoring a ferromagnetic spin alignment between spins of different orbitals at the same site, while the fourth term gives rise to pair hopping. Choosing $U = 1.02$ eV and $J = U/4$ brings the system very close to the SDW transition [87, 126].

As discussed previously one way of introducing a breaking of the fourfold lattice symmetry consists of introducing a magnetic anisotropy. Within the Hubbard model, this corresponds to the introduction of an additional phenomenological Hamiltonian, which describes anisotropic Heisenberg interactions

$$H_{\text{Heis}} = J_x \sum_{\substack{\langle \mathbf{i}, \mathbf{j} \rangle || x \\ \mu, \nu}} \mathbf{S}_{\mathbf{i}, \mu} \cdot \mathbf{S}_{\mathbf{j}, \nu} + J_y \sum_{\substack{\langle \mathbf{i}, \mathbf{j} \rangle || y \\ \mu, \nu}} \mathbf{S}_{\mathbf{i}, \mu} \cdot \mathbf{S}_{\mathbf{j}, \nu}, \quad (4.13)$$

where the orbitals are denoted by μ, ν and the neighboring spins interact with different strengths via nearest-neighbor bonds $\langle \mathbf{i}, \mathbf{j} \rangle$ along x and y direction. The couplings J_x and J_y can have different magnitudes and signs. An AFM coupling

is achieved by choosing both $J_{x/y} > 0$. Because rotational symmetry is only broken locally on the small cluster by the introduction of these anisotropic Heisenberg couplings long-range order is not introduced and the system does not undergo a transition into the SDW state. Within the formalism of CPT of Sec. 2.2, small 4-site clusters are treated accurately via ED and the purely kinetic intercluster interaction is treated perturbatively.

Another approach to break rotational symmetry close to the SDW transition is the introduction of a symmetry-breaking orbital ordering field. The corresponding Hamiltonian

$$H_{\text{orb}} = \Delta \sum_{\mathbf{i}} (n_{\mathbf{i},yz} - n_{\mathbf{i},xz}) \quad (4.14)$$

describes the breaking of the symmetry between d_{xz} and d_{yz} orbitals by introducing an energy difference Δ between the onsite energies. Choosing $\Delta > 0$ favors the occupation of the d_{xz} orbital. This situation has been proposed as an explanation of the anisotropy seen in the spectral density [113, 122].

A third mechanism to describe the symmetry breaking of the fourfold lattice symmetry within the Hubbard model consists of introducing an anisotropy of the hopping parameters t_i along one direction. Although there is consensus that the structural phase transition is not purely driven by phonons, introducing a lattice anisotropy might give a hint on how large the tetragonal distortion should be in order to explain the rather large anisotropies in the electronic and orbital degrees of freedom.

While CPT is used here to treat the nematic phase and to keep interaction short-range within the 4-site cluster, the SDW phase can be treated within the VCA formalism by the variational optimization of the grand potential with respect to a fictitious ordering field [131, 144]. Although basically all parameters of one-particle operators of the Hamiltonian can be optimized via this approach, only the optimization of a fictitious chemical potential is needed for thermodynamic consistency as discussed previously in Sec. 3.3.

4.3 Results

The Hamiltonian given in Eq. (4.6), (4.7) and (4.12) has been treated within the VCA method using a four-site cluster. Here, a fictitious chemical potential was used as an optimization parameter. The fourfold rotational lattice symmetry is explicitly

broken by the insertion of an orbital ordering field (Eq. (4.14)), the introduction of anisotropic Heisenberg couplings (Eq. (4.13)) and the usage of anisotropic hoppings.

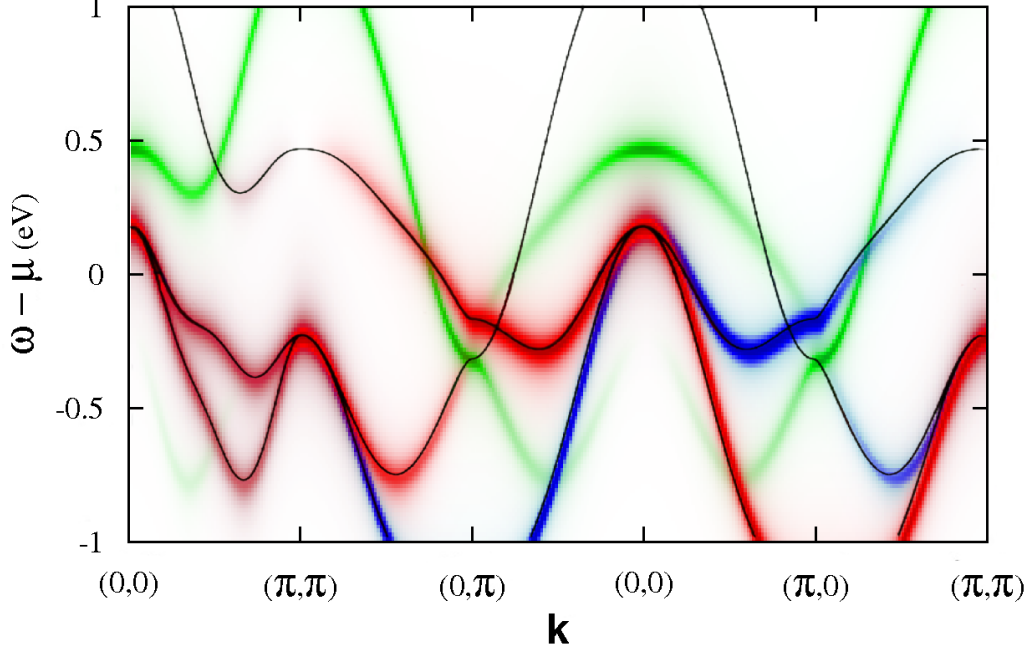


Figure 4.7: Spectral density $A(\mathbf{k}, \omega)$ of the noninteracting three-band model. Solid lines indicate the band structure in terms of the pseudocrystal momentum $\tilde{\mathbf{k}}$, while shaded areas indicate the spectral weight in terms of the ‘lab-space’ momentum \mathbf{k} . In this representation the weight with d_{xy} character (green) is shifted by (π, π) . Spectral density with dominant d_{xz} character is shaded in red, whereas spectral weight with d_{yz} character is shaded in blue.

The noninteracting band structure is shown in Fig. 4.7. Hereby, the difference between the pseudocrystal momentum $\tilde{\mathbf{k}}$ and the ‘lab-space’ momentum \mathbf{k} becomes visible by a shift of the spectral weight of the d_{xy} orbital by (π, π) . Using a one-iron unit cell allows a distinction between the $X = (\pi, 0)$ and $Y = (0, \pi)$ points of the Brillouin zone, which would both map to (π, π) in the two-iron unit cell. At Y the spectral weight is dominated by the d_{xz} orbital and at X the spectral density has d_{yz} character.

All three symmetry-breaking mechanisms presented in Sec. 4.2 in principal reproduce the band structure observed by ARPES, with band distortions mostly pronounced at X and Y . The d_{yz} band moves towards higher energies at X , compared to the d_{xz} band at the Y point, while changes around $\Gamma = (0, 0)$ are far less pronounced.

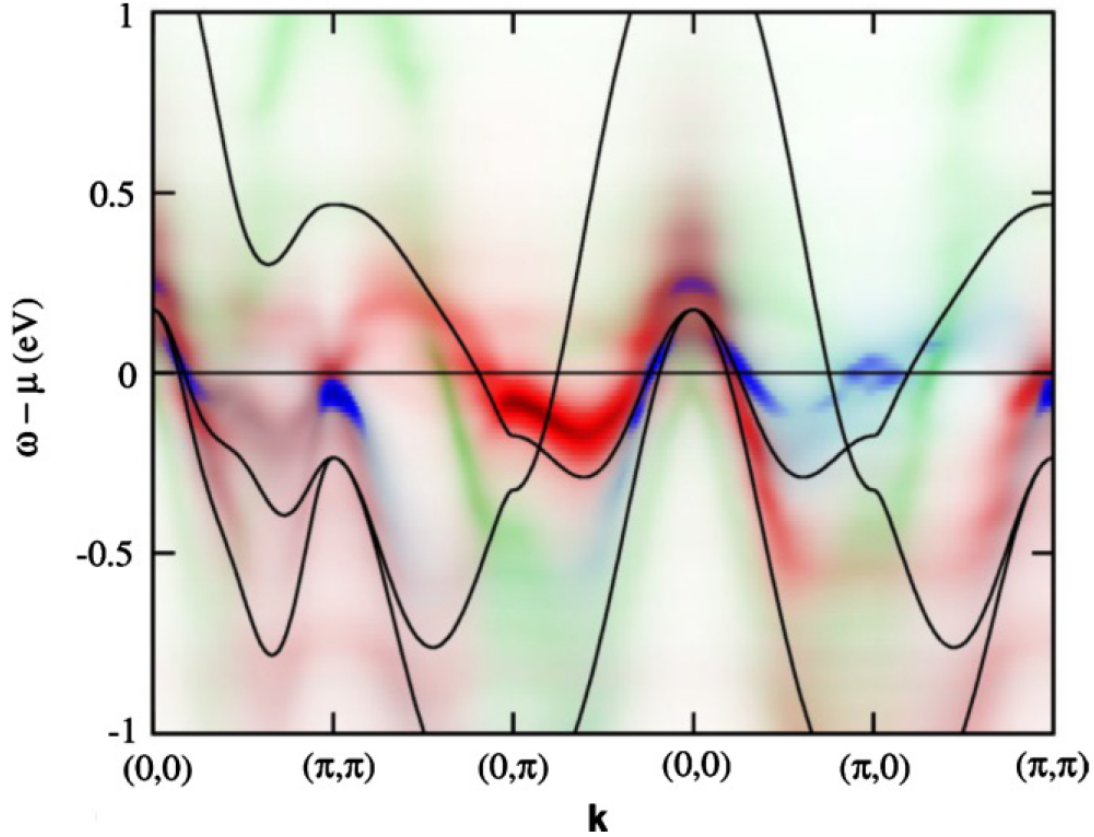


Figure 4.8: Spectral density with additional short-range anisotropic AFM couplings $J_x = 0.04$ eV and $J_y = 0.01$ eV, following Eq. (4.13). Solid lines indicate the noninteracting band structure in terms of the pseudocrystal momentum $\tilde{\mathbf{k}}$. Figure taken from [87].

In Fig. 4.8 the spectral density with inserted anisotropic magnetic couplings is shown using a Hubbard repulsion of $U = 1.02$ eV, which pushes the system very close to the SDW transition. Within CPT the clusters are only coupled kinetically, which keeps the magnetic couplings of short-range. Here, both couplings $J_x = 0.04$ eV and $J_y = 0.01$ eV are AFM. In a previous study by Daghofer *et al.* [126] the couplings were chosen to be AFM along the x direction ($J_x = 0.015$ eV) and FM along the y direction ($J_y = -0.015$ eV). The results are comparable to the spectral weight in Fig. 4.8, which allows the conclusion that the result basically depends only on the difference of the magnetic couplings into x and y direction. Furthermore, interactions strongly enhance the effect of anisotropic Heisenberg couplings. If interactions are strong enough to push the system very close to the SDW transition, a very small anisotropy in the Heisenberg couplings of 0.03 eV is needed to push the spectral weight of the d_{yz} orbital above the Fermi energy. This can also be seen in ARPES experiments on NaFeAs [114] at temperatures right above the SDW transition.

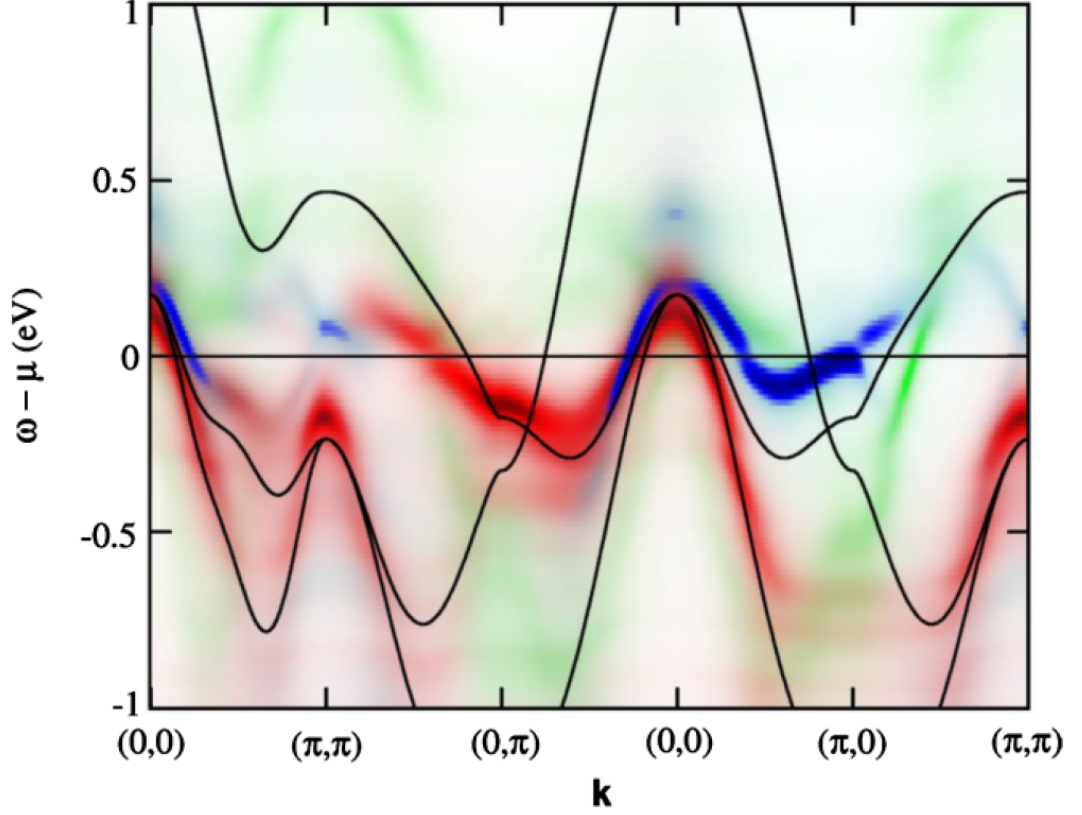


Figure 4.9: Spectral density $A(\mathbf{k}, \omega)$ of the three-band model near the SDW transition ($U = 1.02$ eV, $J = U/4$) with an additional symmetry-breaking field $\Delta = 0.1$ eV which breaks the orbital symmetry between d_{xz} and d_{yz} orbitals (see Eq. (4.14)). Figure taken from [87].

The spectral density of the system including a phenomenological orbital ordering field $\Delta = 0.1$ eV is shown in Fig. 4.9. The distribution of the spectral weight with a lifting of the d_{yz} states at the X point is comparable to the effects in Fig. 4.8, where anisotropic Heisenberg couplings were used instead of an orbital ordering field. Nevertheless, the amplitude of orbital energy splitting needed to obtain this behavior is quite large. The applied $\Delta = 0.1$ eV in Fig. 4.9 is of the order of the observed band anisotropy, whereas the difference in the AFM couplings in Fig. 4.8 is only $\Delta J = 0.03$ eV. Thus, AFM couplings become more effective when onsite interactions are strong [126] while orbital energy splitting is not enhanced by interactions.

While the electronic and orbital degrees of freedom were explicitly broken in Fig. 4.8 and Fig. 4.9, a similar result can be obtained by the introduction of anisotropic kinetic hoppings as shown in Fig. 4.10. Introducing a difference between the x and y

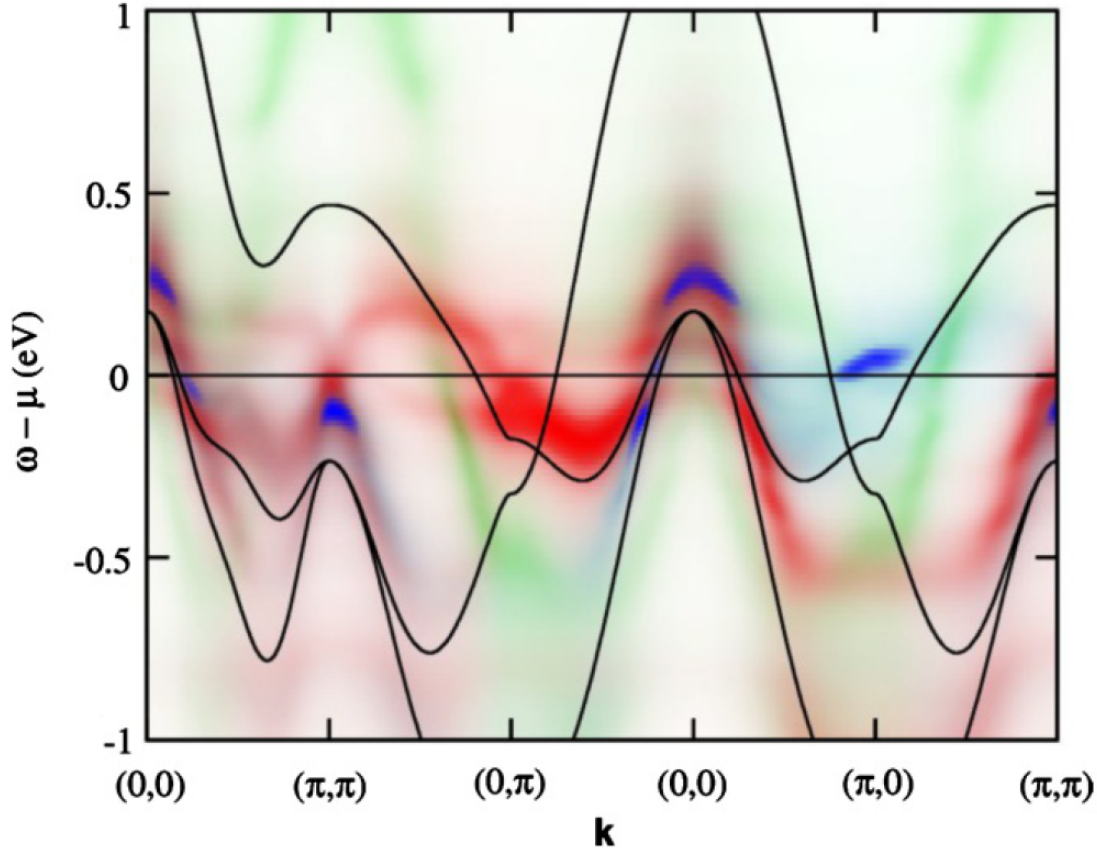


Figure 4.10: Spectral density with phenomenological anisotropy in the hopping parameter t_2 , which is 10% larger in the y direction. Figure taken from [87].

directions of the hopping parameters therefore can reproduce the picture of a lifting of the d_{yz} states at X , although a rather large difference of 5-10% is needed to lift the weight of the d_{yz} orbital above the Fermi energy. Figure 4.10 shows the spectral weight for an anisotropy purely in the hopping parameter t_2 , which has been found to deliver the dominant contribution to the energy splitting, while an anisotropy in t_1 , t_5 and t_7 leads to far smaller effects.

In the noninteracting system anisotropic hoppings do not lift the energy of the d_{yz} states, they just increase the dispersion. The large anisotropy needed to push the states above the Fermi energy in the interacting system close to the SDW transition leads to a distortion of the bands. The d_{yz} band becomes incoherent between Γ and X , leaving only some coherent contributions above the Fermi energy at the X point. Therefore, the breaking of the orbital symmetry within the nematic phase is likely to be not purely phonon driven, which is in consensus with the opinion that the phase transition is more likely driven by spin fluctuations or orbital ordering [107].

4.4 Conclusions

Since all three scenarios presented above break the same symmetry, a decision between the distinct scenarios is difficult. As soon as one scenario breaks the rotational symmetry of the lattice, the other degrees of freedom are broken as well, which hinders the identification of a possible driving force. Studying the signatures of the three isolated scenarios above may help to identify the most important effects.

Both scenarios of short-range anisotropic magnetic couplings (Fig. 4.8) and orbital ordering (Fig. 4.9) produce similar band structures if interactions are strong enough to bring the system close to the SDW transition. For example, the d_{yz} orbital is then pushed to higher energies [87, 122, 126], which corresponds to ARPES measurements.

Differences between the mechanisms consist in a different dependence of interactions and in the strength of the orbital polarization. An orbital ordering field does not profit from increased interactions, whereas anisotropic Heisenberg couplings are much more effective when interactions are strong. To obtain a splitting of ≈ 100 meV, an orbital ordering field of $\Delta = 0.1$ eV is needed (Fig. 4.9), while a much smaller anisotropy of short-range magnetic couplings $J_x - J_y = 0.03$ eV produces a similar result. In the latter case, the orbital polarization $n_{xz} - n_{yz} \approx 0.02$ is nearly vanishing, whereas it is much stronger when an orbital ordering field $\Delta = 0.1$ eV is applied ($n_{xz} - n_{yz} \approx 0.38$). An anisotropy of the hoppings has to be unphysically large to obtain a comparable splitting of the orbital energies.

Further differences between the scenarios include changes of the spectral weight distribution around Γ in the case of an applied orbital energy splitting, compared to anisotropic hoppings and anisotropic magnetic interactions. If anisotropic hoppings are large enough to lift d_{yz} states at X , a large incoherent region appears between Γ and X . The spectral weight of the d_{yz} band almost vanishes in this region, leaving only a coherent part above the Fermi level at the X point. Such a lack of coherence is in disagreement with ARPES measurements [92–94], which makes a purely lattice-driven transition rather unlikely.

A distinction between the remaining two scenarios is difficult. A splitting in the orbital energies large enough to lift the d_{yz} states above the Fermi level at X induces also changes of the spectral weight around the Γ point which are not seen by ARPES. Additionally, this scenario is not supported by onsite interactions, which

support anisotropic short-range Heisenberg interactions instead. But still, a decision of the isolated scenarios based on ARPES data remains difficult as they all produce similar features while breaking the same symmetries. As several classes of the variety of compounds in the family of the pnictide superconductors exhibit different electronic properties it might happen that different mechanisms are the driving force for the in different compounds of the iron pnictides.

Finally, in order to be able to apply quantum cluster methods to the materials class of iron pnictides, substantial approximations have to be applied. Using a three-band model limits the cluster size to four. Only iron sites are treated and possible three-dimensional effects are ignored. Onsite correlations are treated exactly only within the small cluster. Furthermore, it is not possible to study spontaneous symmetry breaking between the d_{xz} and d_{yz} orbitals within this CPT analysis. Applying the VCA and using the difference in onsite energies Δ as a variational parameter could be used to observe this effect but very preliminary results do not indicate such a tendency.

5 Summary and Outlook

After an introduction on a variety of quantum cluster methods and a derivation of the two methods of choice within this thesis, CPT and the VCA, these methods were applied to clarify open questions within the field of correlated-electron systems.

Quantum cluster theories such as CPT and the VCA are powerful tools to calculate electronic properties of systems with strong short-range correlations. As there is always a prize to pay, only systems which can be idealized by a small number of degrees of freedom can be treated as cluster dimensions are usually strongly limited. Due to small cluster sizes, finite-size effects may arise and the results can depend on the geometry of the chosen cluster. Larger clusters would be possible if more memory would be available, but the effort increases exponentially.

In Chapter 3 the nature of the ground state of a triangular lattice at $3/4$ filling has been determined by the application of the VCA to various cluster geometries. Here, several previously proposed phases were studied by comparing their grand potentials using the VCA to optimize the respective order parameters and chemical potentials. The strength of quantum cluster approaches lies in particular in the regime of strong coupling, where fluctuations are generally of short range and therefore localized mainly within the cluster, which is treated numerically exactly by ED. This allows robust statements about ground state properties in the system in the strongly interacting limit, where previous renormalization group approaches fail or become uncontrolled.

In the weak-coupling regime the results of the VCA are in agreement with renormalization group investigations. Here, a superconducting phase with a time-reversal symmetry breaking chiral $d+id$ -wave order parameter has been found to be the ground state. Towards the regime of strong interactions the system most likely undergoes a phase transition into a collinear SDW state with a quadrupled unit cell and nonuniform local moments. Depending on the cluster geometry also triplet f -wave symmetry has been found at strong interactions, making it an additional candidate for the ground state.

Within the study of triangular lattices problems and limitations of quantum cluster methods became strongly visible. The most limiting restraint lies in the restriction to relatively small clusters sizes as they would otherwise exceed the capability of ED. The desire to study all possible phases on equal footing limits the shape of possible cluster geometries even further. Due to a particle-hole transformation in one spin channel, which is necessary to study superconducting phases, the Hilbert space is additionally increased, resulting in an additional limitation of the cluster size. SDW states have been studied for a 12-site cluster, whereas superconducting phases can be treated for clusters up to a size of 8 sites.

A comparison of the grand potential of the disordered state has been used as an indication for the stability of superconducting and magnetically ordered phases between different cluster geometries. This procedure became necessary as the results strongly depend on the size and the particular shape of the cluster. These finite size effects are a shortcoming of VCA and prevent a robust conclusion about the nature of the ground state in the regime of intermediate couplings, where correlations are of the order of the cluster size.

The open question of the ground state of the $3/4$ filled triangular lattice with strong interactions could surprisingly be answered with a collinear SDW state with nonuniform local moments. Previously, a chiral SDW state has been proposed to be the ground state as it lowers its energy by the formation of a gap due to spontaneous quantum Hall effect. Here, this chiral state suffers from spin fluctuations as it does in the Kondo lattice model and is therefore suppressed. The collinear SDW ground state has unique electronic and transport properties since it opens a gap only in one spin channel. Such an exotic state could be highly desirable for the electrical control of spin currents.

In Chapter 4 several mechanisms were studied that break the fourfold lattice symmetry of the FeAs planes in the nematic phase of iron pnictide superconductors using CPT on a three-band model in order to find the leading mechanism which is responsible for the large orbital energy splitting between the X and the Y point observed by ARPES. Short-range magnetic couplings, an orbital energy splitting field as well as anisotropic hoppings delivered similar features in the spectral density distribution when interactions are large enough to bring the system close to the SDW transition. Since interactions support the effect arising from anisotropic magnetic couplings, a small anisotropy is sufficient to observe a large splitting of the orbital

energies. On the other hand, a phenomenological orbital splitting is not enhanced by interactions. The anisotropy of the hoppings has to be unphysically large to observe qualitatively similar effects as they lead to incoherent band structures. As soon as the lattice symmetry is broken by one mechanism the symmetry of the other degrees of freedom is broken as well. Thus, a decision between the isolated scenarios is impossible, but the driving force of the transition is likely to have a magnetic or orbital origin.

The models and methods used rely on substantial approximations. The three most important iron d -bands were taken into account and the calculations were performed on a small four-site cluster, allowing only short-range correlations to be treated accurately. Since the importance of the arsenic p orbitals has recently been a matter of debate, more detailed evaluations are desired. In its present form, the model used only provides a generic picture of the iron-based superconductors without incorporating characteristics of different compounds. The general question, which features a system should provide to allow orbital ordering to occur, remains to be answered. In several compounds of the materials class the formation of the nematic phase has proven to be orbital driven, including FeSe [145], whereas the calculations in this thesis indicate that the mechanism is spin driven.

Bibliography

- [1] E. Dagotto. “Correlated electrons in high-temperature superconductors”. In: *Rev. Mod. Phys.* 66 (1994), pp. 763–840. URL: <http://link.aps.org/doi/10.1103/RevModPhys.66.763>.
- [2] M. M. Qazilbash, J. J. Hamlin, R. E. Baumbach, L. Zhang, and D. J. Singh. “Electronic correlations in the iron pnictides”. In: *Nat. Phys.* 5 (2009), pp. 647–650. URL: <http://dx.doi.org/10.1038/nphys1343>.
- [3] P. Soven. “Coherent-Potential Model of Substitutional Disordered Alloys”. In: *Phys. Rev.* 156 (1967), pp. 809–813. URL: <http://link.aps.org/doi/10.1103/PhysRev.156.809>.
- [4] D. Taylor. “Vibrational Properties of Imperfect Crystals with Large Defect Concentrations”. In: *Phys. Rev.* 156 (1967), pp. 1017–1029. URL: <http://link.aps.org/doi/10.1103/PhysRev.156.1017>.
- [5] H. Shiba. “A Reformulation of the Coherent Potential Approximation and Its Applications”. In: *Progress of Theoretical Physics* 46 (1971), pp. 77–94. URL: <http://ptp.oxfordjournals.org/content/46/1/77.abstract>.
- [6] W. Metzner and D. Vollhardt. “Correlated Lattice Fermions in $d = \infty$ Dimensions”. In: *Phys. Rev. Lett.* 62 (1989), pp. 324–327. URL: <http://link.aps.org/doi/10.1103/PhysRevLett.62.324>.
- [7] A. Georges, G. Kotliar, W. Krauth, and M. Rozenberg. “Dynamical mean-field theory of strongly correlated fermion systems and the limit of infinite dimensions”. In: *Rev. Mod. Phys.* 68 (1996), pp. 13–125. URL: <http://link.aps.org/doi/10.1103/RevModPhys.68.13>.
- [8] M. Potthoff, M. Aichhorn, and C. Dahnken. “Variational Cluster Approach to Correlated Electron Systems in Low Dimensions”. In: *Phys. Rev. Lett.* 91 (2003), p. 206402. URL: <http://link.aps.org/doi/10.1103/PhysRevLett.91.206402>.
- [9] M. H. Hettler, A. N. Tahvildar-Zadeh, M. Jarrell, T. Pruschke, and H. R. Krishnamurthy. “Nonlocal dynamical correlations of strongly interacting electron systems”. In: *Phys. Rev. B* 58 (1998), R7475–R7479. URL: <http://link.aps.org/doi/10.1103/PhysRevB.58.R7475>.

- [10] G. Kotliar, S. Y. Savrasov, G. Pálsson, and G. Biroli. “Cellular Dynamical Mean Field Approach to Strongly Correlated Systems”. In: *Phys. Rev. Lett.* 87 (2001), p. 186401. URL: <http://link.aps.org/doi/10.1103/PhysRevLett.87.186401>.
- [11] C. Gros and R. Valenti. “A self-consistent cluster study of the Emery model”. In: *Ann.Phys. (Leipzig)* 3 (1994), p. 460.
- [12] D. Sénéchal, D. Perez, and M. Pioro-Ladrière. “Spectral Weight of the Hubbard Model through Cluster Perturbation Theory”. In: *Phys. Rev. Lett.* 84 (2000), pp. 522–525. URL: <http://link.aps.org/doi/10.1103/PhysRevLett.84.522>.
- [13] M. Potthoff. “Making use of self-energy functionals: The variational cluster approximation”. In: *DMFT at 25: Infinite Dimensions. Lecture Notes of the Autumn School on Correlated Electrons 2014*. Ed. by E. Pavarini, E. Koch, D. Vollhardt, and A. Lichtenstein. Forschungszentrum Jülich GmbH, 2014. Chap. 9.
- [14] R. Eder. “The Variational Cluster Approximation”. In: *Emergent Phenomena in Correlated Matter*. Ed. by E. Pavarini, E. Koch, and U. Schollwöck. Forschungszentrum Jülich GmbH, 2013. Chap. 4.
- [15] M. Potthoff. “Self-energy-functional approach to systems of correlated electrons”. English. In: *The European Physical Journal B - Condensed Matter and Complex Systems* 32 (2003), p. 429. URL: <http://epjb.epj.org/articles/epjb/abs/2003/08/b03014/b03014.html>.
- [16] M. C. Gutzwiller. “Effect of Correlation on the Ferromagnetism of Transition Metals”. In: *Phys. Rev. Lett.* 10 (1963), pp. 159–162. URL: <http://link.aps.org/doi/10.1103/PhysRevLett.10.159>.
- [17] J. Kanamori. “Electron Correlation and Ferromagnetism of Transition Metals”. In: *Progress of Theoretical Physics* 30 (1963), pp. 275–289. URL: <http://ptp.oxfordjournals.org/content/30/3/275.abstract>.
- [18] J. Hubbard. “Electron Correlations in Narrow Energy Bands”. In: *Proceedings of the Royal Society of London. Series A. Mathematical and Physical Sciences* 276 (1963), pp. 238–257. URL: <http://rspa.royalsocietypublishing.org/content/276/1365/238.abstract>.
- [19] “The Hubbard model at half a century”. In: *Nat. Phys.* 9 (2013), pp. 523–523. ISSN: 1745-2473. URL: <http://dx.doi.org/10.1038/nphys275910.1038/nphys2759>.

- [20] F. H. Essler, H. Frahm, F. Göhmann, A. Klümper, and V. E. Korepin. *The one-dimensional Hubbard model*. Cambridge University Press, 2005.
- [21] E. H. Lieb and F. Wu. “The one-dimensional Hubbard model: a reminiscence”. In: *Physica A: Statistical Mechanics and its Applications* 321 (2003). Statphys-Taiwan-2002: Lattice Models and Complex Systems, pp. 1–27. ISSN: 0378-4371. URL: <http://www.sciencedirect.com/science/article/pii/S0378437102017855>.
- [22] A. Georges, L. d. Medici, and J. Mravlje. “Strong Correlations from Hund’s Coupling”. In: *Annual Review of Condensed Matter Physics* 4 (2013), pp. 137–178. URL: <http://dx.doi.org/10.1146/annurev-conmatphys-020911-125045>.
- [23] L. de’Medici. “Hund’s coupling and its key role in tuning multiorbital correlations”. In: *Phys. Rev. B* 83 (2011), p. 205112. URL: <http://link.aps.org/doi/10.1103/PhysRevB.83.205112>.
- [24] F. Hund. “Zur Deutung verwickelter Spektren, insbesondere der Elemente Scandium bis Nickel”. In: *Z. Phys* 33 (1925), pp. 345–371.
- [25] A. M. Oleś. “Antiferromagnetism and correlation of electrons in transition metals”. In: *Phys. Rev. B* 28 (1983), pp. 327–339. URL: <http://link.aps.org/doi/10.1103/PhysRevB.28.327>.
- [26] C. Castellani, C. R. Natoli, and J. Ranninger. “Magnetic structure of V_2O_3 in the insulating phase”. In: *Phys. Rev. B* 18 (1978), pp. 4945–4966. URL: <http://link.aps.org/doi/10.1103/PhysRevB.18.4945>.
- [27] C. Lanczos. “An Iteration Method for the Solution of the Eigenvalue Problem of Linear Differential and Integral Operators”. In: *J. Res. Natl. Bur. Stand.* 45 (1950), p. 255.
- [28] R. W. Freund. “Band Lanczos Method”. In: *Templates for the Solution of Algebraic Eigenvalue Problems: A Practical Guide*. Ed. by Z. Bai, J. Demmel, J. Dongarra, A. Ruhe, and H. van der Vorst. SIAM, Philadelphia, 2000. Chap. 9.
- [29] S. Pairault, D. Sénéchal, and A.-M. S. Tremblay. “Strong-Coupling Expansion for the Hubbard Model”. In: *Phys. Rev. Lett.* 80 (1998), pp. 5389–5392. URL: <http://link.aps.org/doi/10.1103/PhysRevLett.80.5389>.
- [30] A. Abrikosov, L. Gorkov, and I. Dzyaloshinski. *Methods of quantum field theory in statistical physics*. New York, N.Y.: Dover, 1963.

- [31] J. W. Negele and H. Orland. *Quantum many-particle systems*. Advanced book classics. Addison-Wesley edition. Boulder, CO: Westview, 1988.
- [32] T. Maier, M. Jarrell, T. Pruschke, and M. H. Hettler. “Quantum cluster theories”. In: *Rev. Mod. Phys.* 77 (2005), pp. 1027–1080. URL: <http://link.aps.org/doi/10.1103/RevModPhys.77.1027>.
- [33] M. Potthoff. “Self-energy-functional approach: Analytical results and the Mott-Hubbard transition”. English. In: *The European Physical Journal B - Condensed Matter and Complex Systems* 36 (2003), pp. 335–348. ISSN: 1434-6028. URL: <http://dx.doi.org/10.1140/epjb/e2003-00352-7>.
- [34] J. M. Luttinger and J. C. Ward. “Ground-State Energy of a Many-Fermion System. II”. In: *Phys. Rev.* 118 (1960), pp. 1417–1427. URL: <http://link.aps.org/doi/10.1103/PhysRev.118.1417>.
- [35] M. Aichhorn, H. G. Evertz, W. von der Linden, and M. Potthoff. “Charge ordering in extended Hubbard models: Variational cluster approach”. In: *Phys. Rev. B* 70 (2004), p. 235107. URL: <http://link.aps.org/doi/10.1103/PhysRevB.70.235107>.
- [36] C. Dahnken, M. Aichhorn, W. Hanke, E. Arrigoni, and M. Potthoff. “Variational cluster approach to spontaneous symmetry breaking: The itinerant antiferromagnet in two dimensions”. In: *Phys. Rev. B* 70 (2004), p. 245110. URL: <http://link.aps.org/doi/10.1103/PhysRevB.70.245110>.
- [37] G. Knizia and G. K.-L. Chan. “Density Matrix Embedding: A Simple Alternative to Dynamical Mean-Field Theory”. In: *Phys. Rev. Lett.* 109 (2012), p. 186404. URL: <http://link.aps.org/doi/10.1103/PhysRevLett.109.186404>.
- [38] G. Knizia and G. K.-L. Chan. “Density Matrix Embedding: A Strong-Coupling Quantum Embedding Theory”. In: *Journal of Chemical Theory and Computation* 9 (2013), pp. 1428–1432. URL: <http://dx.doi.org/10.1021/ct301044e>.
- [39] A. Liebsch and H. Ishida. “Temperature and bath size in exact diagonalization dynamical mean field theory”. In: *Journal of Physics: Condensed Matter* 24 (2012), p. 053201. URL: <http://stacks.iop.org/0953-8984/24/i=5/a=053201>.
- [40] P. W. Anderson. “Localized Magnetic States in Metals”. In: *Phys. Rev.* 124 (1961), pp. 41–53. URL: <http://link.aps.org/doi/10.1103/PhysRev.124.41>.

-
- [41] N. Bickers, D. Scalapino, and S. White. “Conserving Approximations for Strongly Correlated Electron Systems: Bethe-Salpeter Equation and Dynamics for the Two-Dimensional Hubbard Model”. In: *Phys. Rev. Lett.* 62 (1989), pp. 961–964. URL: <http://link.aps.org/doi/10.1103/PhysRevLett.62.961>.
- [42] N. Bickers and S. White. “Conserving approximations for strongly fluctuating electron systems. II. Numerical results and parquet extension”. In: *Phys. Rev. B* 43 (1991), pp. 8044–8064. URL: <http://link.aps.org/doi/10.1103/PhysRevB.43.8044>.
- [43] K. Aryanpour, M. Hettler, and M. Jarrell. “Dynamical cluster approximation employing the fluctuation exchange approximation as a cluster solver”. In: *Phys. Rev. B* 67 (2003), p. 085101. URL: <http://link.aps.org/doi/10.1103/PhysRevB.67.085101>.
- [44] H. Keiter and J. Kimball. “Perturbation Technique for the Anderson Hamiltonian”. In: *Phys. Rev. Lett.* 25 (1970), pp. 672–675. URL: <http://link.aps.org/doi/10.1103/PhysRevLett.25.672>.
- [45] N. Bickers. “Review of techniques in the large- N expansion for dilute magnetic alloys”. In: *Rev. Mod. Phys.* 59 (1987), pp. 845–939. URL: <http://link.aps.org/doi/10.1103/RevModPhys.59.845>.
- [46] K. Wilson. “The renormalization group: Critical phenomena and the Kondo problem”. In: *Rev. Mod. Phys.* 47 (1975), pp. 773–840. URL: <http://link.aps.org/doi/10.1103/RevModPhys.47.773>.
- [47] H. Krishnamurthy, J. Wilkins, and K. Wilson. “Renormalization-group approach to the Anderson model of dilute magnetic alloys. I. Static properties for the symmetric case”. In: *Phys. Rev. B* 21 (1980), pp. 1003–1043. URL: <http://link.aps.org/doi/10.1103/PhysRevB.21.1003>.
- [48] H. Krishnamurthy, J. Wilkins, and K. Wilson. “Renormalization-group approach to the Anderson model of dilute magnetic alloys. II. Static properties for the asymmetric case”. In: *Phys. Rev. B* 21 (1980), pp. 1044–1083. URL: <http://link.aps.org/doi/10.1103/PhysRevB.21.1044>.
- [49] A. C. Hewson. *The Kondo Problem to Heavy Fermions*. Cambridge Books Online. Cambridge University Press, 1993. ISBN: 9780511470752. URL: <http://dx.doi.org/10.1017/CB09780511470752>.

- [50] R. Haydock, V. Heine, and M. J. Kelly. “Electronic structure based on the local atomic environment for tight-binding bands. II”. In: *Journal of Physics C: Solid State Physics* 8 (1975), p. 2591. URL: <http://stacks.iop.org/0022-3719/8/i=16/a=011>.
- [51] C. C. Paige. “Computational variants of the Lanczos Method”. In: *J. Inst. Math. Appl.* 10 (1972), p. 373.
- [52] H. Lin and J. Gubernatis. “Exact diagonalization methods for quantum systems”. In: *Computers in Physics* 7 (1993).
- [53] M. Capone, L. de’Medici, and A. Georges. “Solving the dynamical mean-field theory at very low temperatures using the Lanczos exact diagonalization”. In: *Phys. Rev. B* 76 (2007), p. 245116. URL: <http://link.aps.org/doi/10.1103/PhysRevB.76.245116>.
- [54] M. Caffarel and W. Krauth. “Exact diagonalization approach to correlated fermions in infinite dimensions: Mott transition and superconductivity”. In: *Phys. Rev. Lett.* 72 (1994), pp. 1545–1548. URL: <http://link.aps.org/doi/10.1103/PhysRevLett.72.1545>.
- [55] J. Jaklič and P. Prelovšek. “Finite-temperature properties of doped anti-ferromagnets”. In: *Advances in Physics* 49 (2000), pp. 1–92. URL: <http://dx.doi.org/10.1080/000187300243381>.
- [56] D. D. Betts, S. Matsui, N. Vats, and G. E. Stewart. In: *Can. J. Phys.* 74 (1996), p. 54.
- [57] M. Jarrell, T. Maier, C. Huscroft, and S. Moukouri. “Quantum Monte Carlo algorithm for nonlocal corrections to the dynamical mean-field approximation”. In: *Phys. Rev. B* 64 (2001), p. 195130. URL: <http://link.aps.org/doi/10.1103/PhysRevB.64.195130>.
- [58] F. Grandi, F. Manghi, O. Corradini, C. M. Bertoni, and A. Bonini. “Topological invariants in interacting quantum spin Hall: a cluster perturbation theory approach”. In: *New Journal of Physics* 17 (2015), p. 023004. URL: <http://stacks.iop.org/1367-2630/17/i=2/a=023004>.
- [59] S. Raghu, S. A. Kivelson, and D. J. Scalapino. “Superconductivity in the repulsive Hubbard model: An asymptotically exact weak-coupling solution”. In: *Phys. Rev. B* 81 (2010), p. 224505. URL: <http://link.aps.org/doi/10.1103/PhysRevB.81.224505>.

-
- [60] R. Nandkishore, G.-W. Chern, and A. V. Chubukov. “Itinerant Half-Metal Spin-Density-Wave State on the Hexagonal Lattice”. In: *Phys. Rev. Lett.* 108 (2012), p. 227204. URL: <http://link.aps.org/doi/10.1103/PhysRevLett.108.227204>.
- [61] R. Nandkishore, L. S. Levitov, and A. V. Chubukov. “Chiral superconductivity from repulsive interactions in doped graphene”. In: *Nature Phys.* 8 (2012), p. 158. URL: <http://dx.doi.org/10.1038/nphys2208>.
- [62] I. Martin and C. D. Batista. “Itinerant Electron-Driven Chiral Magnetic Ordering and Spontaneous Quantum Hall Effect in Triangular Lattice Models”. In: *Phys. Rev. Lett.* 101 (2008), p. 156402. URL: <http://link.aps.org/doi/10.1103/PhysRevLett.101.156402>.
- [63] K. Ohgushi, S. Murakami, and N. Nagaosa. “Spin anisotropy and quantum Hall effect in the *kagomé* lattice: Chiral spin state based on a ferromagnet”. In: *Phys. Rev. B* 62 (2000), R6065–R6068. URL: <http://link.aps.org/doi/10.1103/PhysRevB.62.R6065>.
- [64] L. N. Bulaevskii, C. D. Batista, M. V. Mostovoy, and D. I. Khomskii. “Electronic orbital currents and polarization in Mott insulators”. In: *Phys. Rev. B* 78 (2008), p. 024402. URL: <http://link.aps.org/doi/10.1103/PhysRevB.78.024402>.
- [65] B. Ueland, C. Miclea, Y. Kato, O. Ayala-Valenzuela, R. McDonald, R. Okazaki, P. Tobash, M. Torrez, F. Ronning, R. Movshovich, Z. Fisk, E. Bauer, I. Martin, and J. Thompson. “Controllable chirality-induced geometrical Hall effect in a frustrated highly correlated metal”. In: *Nat Commun* 3 (2012). 10.1038/ncomms2075, p. 1067. URL: http://www.nature.com/ncomms/journal/v3/n9/supinfo/ncomms2075_S1.html.
- [66] G.-W. Chern and C. D. Batista. “Spontaneous Quantum Hall Effect via a Thermally Induced Quadratic Fermi Point”. In: *Phys. Rev. Lett.* 109 (2012), p. 156801. URL: <http://link.aps.org/doi/10.1103/PhysRevLett.109.156801>.
- [67] Y. Akagi and Y. Motome. “Spin Chirality Ordering and Anomalous Hall Effect in the Ferromagnetic Kondo Lattice Model on a Triangular Lattice”. In: *Journal of the Physical Society of Japan* 79 (2010), p. 083711. URL: <http://jpsj.ipap.jp/link?JPSJ/79/083711/>.

- [68] Y. Akagi, M. Udagawa, and Y. Motome. “Hidden Multiple-Spin Interactions as an Origin of Spin Scalar Chiral Order in Frustrated Kondo Lattice Models”. In: *Phys. Rev. Lett.* 108 (2012), p. 096401. URL: <http://link.aps.org/doi/10.1103/PhysRevLett.108.096401>.
- [69] Y. Akagi, M. Udagawa, and Y. Motome. “Effect of Quantum Spin Fluctuation on Scalar Chiral Ordering in the Kondo Lattice Model on a Triangular Lattice”. In: *Journal of the Physical Society of Japan* 82 (2013), p. 123709. URL: <http://jpsj.ipap.jp/link?JPSJ/82/123709/>.
- [70] S. Reja, R. Ray, J. van den Brink, and S. Kumar. “Coupled spin-charge order in frustrated itinerant triangular magnets”. In: *ArXiv e-prints* (2014). URL: <http://adsabs.harvard.edu/abs/2014arXiv1412.2319R>.
- [71] A. V. Chubukov and T. Jolicoeur. “Order-from-disorder phenomena in Heisenberg antiferromagnets on a triangular lattice”. In: *Phys. Rev. B* 46 (1992), pp. 11137–11140. URL: <http://link.aps.org/doi/10.1103/PhysRevB.46.11137>.
- [72] C. Honerkamp. “Instabilities of interacting electrons on the triangular lattice”. In: *Phys. Rev. B* 68 (2003), p. 104510. URL: <http://link.aps.org/doi/10.1103/PhysRevB.68.104510>.
- [73] C. Honerkamp and M. Salmhofer. “Magnetic and Superconducting Instabilities of the Hubbard Model at the Van Hove Filling”. In: *Phys. Rev. Lett.* 87 (2001), p. 187004. URL: <http://link.aps.org/doi/10.1103/PhysRevLett.87.187004>.
- [74] J. González. “Kohn-Luttinger superconductivity in graphene”. In: *Phys. Rev. B* 78 (2008), p. 205431. URL: <http://link.aps.org/doi/10.1103/PhysRevB.78.205431>.
- [75] R. Nandkishore and A. V. Chubukov. “Interplay of superconductivity and spin-density-wave order in doped graphene”. In: *Phys. Rev. B* 86 (2012), p. 115426. URL: <http://link.aps.org/doi/10.1103/PhysRevB.86.115426>.
- [76] M. L. Kiesel, C. Platt, W. Hanke, D. A. Abanin, and R. Thomale. “Competing many-body instabilities and unconventional superconductivity in graphene”. In: *Phys. Rev. B* 86 (2012), p. 020507. URL: <http://link.aps.org/doi/10.1103/PhysRevB.86.020507>.

-
- [77] A. H. Castro Neto, F. Guinea, N. M. R. Peres, K. S. Novoselov, and A. K. Geim. “The electronic properties of graphene”. In: *Rev. Mod. Phys.* 81 (2009), pp. 109–162. URL: <http://link.aps.org/doi/10.1103/RevModPhys.81.109>.
- [78] R. Nandkishore, R. Thomale, and A. V. Chubukov. “Superconductivity from weak repulsion in hexagonal lattice systems”. In: *Phys. Rev. B* 89 (2014), p. 144501. URL: <http://link.aps.org/doi/10.1103/PhysRevB.89.144501>.
- [79] W. Kohn and J. M. Luttinger. “New Mechanism for Superconductivity”. In: *Phys. Rev. Lett.* 15 (1965), pp. 524–526. URL: <http://link.aps.org/doi/10.1103/PhysRevLett.15.524>.
- [80] J. M. Luttinger. “New Mechanism for Superconductivity”. In: *Phys. Rev.* 150 (1966), pp. 202–214. URL: <http://link.aps.org/doi/10.1103/PhysRev.150.202>.
- [81] J. Friedel. “XIV. The distribution of electrons round impurities in monovalent metals”. In: *Philosophical Magazine Series 7* 43 (1952), pp. 153–189. URL: <http://dx.doi.org/10.1080/14786440208561086>.
- [82] S. Jiang, A. Mesaros, and Y. Ran. “Chiral Spin-Density Wave, Spin-Charge-Chern Liquid, and $d + id$ Superconductivity in 1/4-Doped Correlated Electronic Systems on the Honeycomb Lattice”. In: *Phys. Rev. X* 4 (2014), p. 031040. URL: <http://link.aps.org/doi/10.1103/PhysRevX.4.031040>.
- [83] M. Aichhorn, E. Arrigoni, M. Potthoff, and W. Hanke. “Antiferromagnetic to superconducting phase transition in the hole- and electron-doped Hubbard model at zero temperature”. In: *Phys. Rev. B* 74 (2006), p. 024508. URL: <http://link.aps.org/doi/10.1103/PhysRevB.74.024508>.
- [84] P. Sahebsara and D. Sénéchal. “Hubbard Model on the Triangular Lattice: Spiral Order and Spin Liquid”. In: *Phys. Rev. Lett.* 100 (2008), p. 136402. URL: <http://link.aps.org/doi/10.1103/PhysRevLett.100.136402>.
- [85] Y. Kamihara, T. Watanabe, M. Hirano, and H. Hosono. “Iron-Based Layered Superconductor $\text{La}_{1-x}\text{F}_x\text{FeAs}$ ($x = 0.05\text{--}0.12$) with $T_c = 26\text{ K}$ ”. In: *Journal of the American Chemical Society* 130 (2008). PMID: 18293989, pp. 3296–3297. URL: <http://dx.doi.org/10.1021/ja800073m>.
- [86] D. C. Johnston. “The puzzle of high temperature superconductivity in layered iron pnictides and chalcogenides”. In: *Advances in Physics* 59 (2010), pp. 803–1061. URL: <http://dx.doi.org/10.1080/00018732.2010.513480>.

- [87] M. Daghofer and A. Fischer. “Breaking of fourfold lattice symmetry in a model for pnictide superconductors”. In: *Superconductor Science and Technology* 25 (2012), p. 084003. URL: <http://stacks.iop.org/0953-2048/25/i=8/a=084003>.
- [88] D. N. Basov and A. V. Chubukov. “Manifesto for a higher T_c ”. In: *Nat Phys* 7 (2011), pp. 272–276. ISSN: 1745-2473. URL: <http://dx.doi.org/10.1038/nphys1975>.
- [89] I. Mazin and J. Schmalian. “Pairing symmetry and pairing state in ferropnictides: Theoretical overview”. In: *Physica C: Superconductivity* 469 (2009), pp. 614 –627. ISSN: 0921-4534. URL: <http://www.sciencedirect.com/science/article/pii/S0921453409001002>.
- [90] D. Singh. “Electronic structure of Fe-based superconductors”. In: *Physica C: Superconductivity* 469 (2009), pp. 418 –424. ISSN: 0921-4534. URL: <http://www.sciencedirect.com/science/article/pii/S0921453409000768>.
- [91] M. Sunagawa, T. Ishiga, K. Tsubota, T. Jabuchi, J. Sonoyama, K. Iba, K. Kudo, M. Nohara, K. Ono, H. Kumigashira, T. Matsushita, M. Arita, K. Shimada, H. Namatame, M. Taniguchi, T. Wakita, Y. Muraoka, and T. Yokoya. “Characteristic two-dimensional Fermi surface topology of high- T_c iron-based superconductors”. In: *Sci. Rep.* 4 (2014). URL: <http://www.nature.com/srep/2014/140314/srep04381/abs/srep04381.html#supplementary-information>.
- [92] D. H. Lu, M. Yi, S.-K. Mo, A. S. Erickson, J. Analytis, J.-H. Chu, D. J. Singh, Z. Hussain, T. H. Geballe, I. R. Fisher, and Z.-X. Shen. “Electronic structure of the iron-based superconductor LaOFeP ”. In: *Nature* 455 (2008), pp. 81–84. ISSN: 0028-0836. URL: http://www.nature.com/nature/journal/v455/n7209/supinfo/nature07263_S1.html.
- [93] T. Kondo, A. F. Santander-Syro, O. Copie, C. Liu, M. E. Tillman, E. D. Mun, J. Schmalian, S. L. Bud’ko, M. A. Tanatar, P. C. Canfield, and A. Kaminski. “Momentum Dependence of the Superconducting Gap in $\text{NdFeAsO}_{0.9}\text{F}_{0.1}$ Single Crystals Measured by Angle Resolved Photoemission Spectroscopy”. In: *Phys. Rev. Lett.* 101 (2008), p. 147003. URL: <http://link.aps.org/doi/10.1103/PhysRevLett.101.147003>.
- [94] H. Ding, P. Richard, K. Nakayama, K. Sugawara, T. Arakane, Y. Sekiba, A. Takayama, S. Souma, T. Sato, T. Takahashi, Z. Wang, X. Dai, Z. Fang, G. F. Chen, J. L. Luo, and N. L. Wang. “Observation of Fermi-surface-dependent nodeless superconducting gaps in $\text{Ba}_{0.6}\text{K}_{0.4}\text{Fe}_2\text{As}_2$ ”. In: *EPL (Europhysics*

- Letters*) 83 (2008), p. 47001. URL: <http://stacks.iop.org/0295-5075/83/i=4/a=47001>.
- [95] R. M. Fernandes, A. V. Chubukov, and J. Schmalian. “What drives nematic order in iron-based superconductors?” In: *Nat Phys* 10 (2014), pp. 97–104. ISSN: 1745-2473. URL: <http://dx.doi.org/10.1038/nphys2877>.
- [96] M. G. Kim, R. M. Fernandes, A. Kreyssig, J. W. Kim, A. Thaler, S. L. Bud’ko, P. C. Canfield, R. J. McQueeney, J. Schmalian, and A. I. Goldman. “Character of the structural and magnetic phase transitions in the parent and electron-doped BaFe_2As_2 compounds”. In: *Phys. Rev. B* 83 (2011), p. 134522. URL: <http://link.aps.org/doi/10.1103/PhysRevB.83.134522>.
- [97] C. R. Rotundu and R. J. Birgeneau. “First- and second-order magnetic and structural transitions in $\text{BaFe}_{2(1-x)}\text{Co}_{2x}\text{As}_2$ ”. In: *Phys. Rev. B* 84 (2011), p. 092501. URL: <http://link.aps.org/doi/10.1103/PhysRevB.84.092501>.
- [98] S. Kasahara, H. J. Shi, K. Hashimoto, S. Tonegawa, Y. Mizukami, T. Shibauchi, K. Sugimoto, T. Fukuda, T. Terashima, A. H. Nevidomskyy, and Y. Matsuda. “Electronic nematicity above the structural and superconducting transition in $\text{BaFe}_2(\text{As}_{1-x}\text{P}_x)_2$ ”. In: *Nature* 486 (2012), pp. 382–385. ISSN: 0028-0836. URL: <http://www.nature.com/nature/journal/v486/n7403/abs/nature11178.html>.
- [99] S. Avci, O. Chmaissem, D. Y. Chung, S. Rosenkranz, E. A. Goremychkin, J. P. Castellan, I. S. Todorov, J. A. Schlueter, H. Claus, A. Daoud-Aladine, D. D. Khalyavin, M. G. Kanatzidis, and R. Osborn. “Phase diagram of $\text{Ba}_{1-x}\text{K}_x\text{Fe}_2\text{As}_2$ ”. In: *Phys. Rev. B* 85 (2012), p. 184507. URL: <http://link.aps.org/doi/10.1103/PhysRevB.85.184507>.
- [100] R. M. Fernandes, E. Abrahams, and J. Schmalian. “Anisotropic In-Plane Resistivity in the Nematic Phase of the Iron Pnictides”. In: *Phys. Rev. Lett.* 107 (2011), p. 217002. URL: <http://link.aps.org/doi/10.1103/PhysRevLett.107.217002>.
- [101] R. M. Fernandes, A. V. Chubukov, J. Knolle, I. Eremin, and J. Schmalian. “Preemptive nematic order, pseudogap, and orbital order in the iron pnictides”. In: *Phys. Rev. B* 85 (2012), p. 024534. URL: <http://link.aps.org/doi/10.1103/PhysRevB.85.024534>.

- [102] C. Fang, H. Yao, W.-F. Tsai, J. Hu, and S. A. Kivelson. “Theory of electron nematic order in LaFeAsO”. In: *Phys. Rev. B* 77 (2008), p. 224509. URL: <http://link.aps.org/doi/10.1103/PhysRevB.77.224509>.
- [103] C. Xu, M. Müller, and S. Sachdev. “Ising and spin orders in the iron-based superconductors”. In: *Phys. Rev. B* 78 (2008), p. 020501. URL: <http://link.aps.org/doi/10.1103/PhysRevB.78.020501>.
- [104] A. Cano, M. Civelli, I. Eremin, and I. Paul. “Interplay of magnetic and structural transitions in iron-based pnictide superconductors”. In: *Phys. Rev. B* 82 (2010), p. 020408. URL: <http://link.aps.org/doi/10.1103/PhysRevB.82.020408>.
- [105] J.-H. Chu, J. G. Analytis, K. De Greve, P. L. McMahon, Z. Islam, Y. Yamamoto, and I. R. Fisher. “In-Plane Resistivity Anisotropy in an Underdoped Iron Arsenide Superconductor”. In: *Science* 329 (2010), pp. 824–826. URL: <http://www.sciencemag.org/content/329/5993/824.abstract>.
- [106] M. A. Tanatar, E. C. Blomberg, A. Kreyssig, M. G. Kim, N. Ni, A. Thaler, S. L. Bud’ko, P. C. Canfield, A. I. Goldman, I. I. Mazin, and R. Prozorov. “Uniaxial-strain mechanical detwinning of CaFe₂As₂ and BaFe₂As₂ crystals: Optical and transport study”. In: *Phys. Rev. B* 81 (2010), p. 184508. URL: <http://link.aps.org/doi/10.1103/PhysRevB.81.184508>.
- [107] L. Boeri, O. V. Dolgov, and A. A. Golubov. “Is LaFeAsO_{1-x}F_x an Electron-Phonon Superconductor?” In: *Phys. Rev. Lett.* 101 (2008), p. 026403. URL: <http://link.aps.org/doi/10.1103/PhysRevLett.101.026403>.
- [108] A. Chubukov. “Pairing Mechanism in Fe-Based Superconductors”. In: *Annual Review of Condensed Matter Physics* 3 (2012), pp. 57–92. URL: <http://dx.doi.org/10.1146/annurev-conmatphys-020911-125055>.
- [109] S. Jiang, H. S. Jeevan, J. Dong, and P. Gegenwart. “Thermopower as a Sensitive Probe of Electronic Nematicity in Iron Pnictides”. In: *Phys. Rev. Lett.* 110 (2013), p. 067001. URL: <http://link.aps.org/doi/10.1103/PhysRevLett.110.067001>.
- [110] A. Dusza, A. Lucarelli, F. Pfner, J.-H. Chu, I. R. Fisher, and L. Degiorgi. “Anisotropic charge dynamics in detwinned Ba(Fe_{1-x}Co_x)₂As₂”. In: *EPL (Europhysics Letters)* 93 (2011), p. 37002. URL: <http://stacks.iop.org/0295-5075/93/i=3/a=37002>.

-
- [111] M. Nakajima, T. Liang, S. Ishida, Y. Tomioka, K. Kihou, C. H. Lee, A. Iyo, H. Eisaki, T. Kakeshita, T. Ito, and S. Uchida. “Unprecedented anisotropic metallic state in undoped iron arsenide BaFe_2As_2 revealed by optical spectroscopy”. In: *Proceedings of the National Academy of Sciences* 108 (2011), pp. 12238–12242. URL: <http://www.pnas.org/content/108/30/12238.abstract>.
- [112] I. R. Fisher, L. Degiorgi, and Z. X. Shen. “In-plane electronic anisotropy of underdoped ‘122’ Fe-arsenide superconductors revealed by measurements of detwinned single crystals”. In: *Reports on Progress in Physics* 74 (2011), p. 124506. URL: <http://stacks.iop.org/0034-4885/74/i=12/a=124506>.
- [113] M. Yi, D. Lu, J.-H. Chu, J. G. Analytis, A. P. Sorini, A. F. Kemper, B. Moritz, S.-K. Mo, R. G. Moore, M. Hashimoto, W.-S. Lee, Z. Hussain, T. P. Devereaux, I. R. Fisher, and Z.-X. Shen. “Symmetry-breaking orbital anisotropy observed for detwinned $\text{Ba}(\text{Fe}_{1-x}\text{Co}_x)_2\text{As}_2$ above the spin density wave transition”. In: *Proceedings of the National Academy of Sciences* 108 (2011), pp. 6878–6883. URL: <http://www.pnas.org/content/108/17/6878.abstract>.
- [114] M. Yi, D. H. Lu, R. G. Moore, K. Kihou, C.-H. Lee, A. Iyo, H. Eisaki, T. Yoshida, A. Fujimori, and Z.-X. Shen. “Electronic reconstruction through the structural and magnetic transitions in detwinned NaFeAs ”. In: *New Journal of Physics* 14 (2012), p. 073019. URL: <http://stacks.iop.org/1367-2630/14/i=7/a=073019>.
- [115] C. He, Y. Zhang, B. P. Xie, X. F. Wang, L. X. Yang, B. Zhou, F. Chen, M. Arita, K. Shimada, H. Namatame, M. Taniguchi, X. H. Chen, J. P. Hu, and D. L. Feng. “Electronic-Structure-Driven Magnetic and Structure Transitions in Superconducting NaFeAs Single Crystals Measured by Angle-Resolved Photoemission Spectroscopy”. In: *Phys. Rev. Lett.* 105 (2010), p. 117002. URL: <http://link.aps.org/doi/10.1103/PhysRevLett.105.117002>.
- [116] Y. Zhang, C. He, Z. R. Ye, J. Jiang, F. Chen, M. Xu, Q. Q. Ge, B. P. Xie, J. Wei, M. Aeschlimann, X. Y. Cui, M. Shi, J. P. Hu, and D. L. Feng. “Symmetry breaking via orbital-dependent reconstruction of electronic structure in detwinned NaFeAs ”. In: *Phys. Rev. B* 85 (2012), p. 085121. URL: <http://link.aps.org/doi/10.1103/PhysRevB.85.085121>.
- [117] M. Fu, D. A. Torchetti, T. Imai, F. L. Ning, J.-Q. Yan, and A. S. Sefat. “NMR Search for the Spin Nematic State in a LaFeAsO Single Crystal”. In:

- Phys. Rev. Lett.* 109 (2012), p. 247001. URL: <http://link.aps.org/doi/10.1103/PhysRevLett.109.247001>.
- [118] E. P. Rosenthal, E. F. Andrade, C. J. Arguello, R. M. Fernandes, L. Y. Xing, X. C. Wang, C. Q. Jin, A. J. Millis, and A. N. Pasupathy. “Visualization of electron nematicity and unidirectional antiferroic fluctuations at high temperatures in NaFeAs”. In: *Nat Phys* 10 (2014), pp. 225–232. ISSN: 1745-2473. URL: <http://dx.doi.org/10.1038/nphys2870>.
 - [119] J. Paglione and R. L. Greene. “High-temperature superconductivity in iron-based materials”. In: *Nat Phys* 6 (2010), pp. 645–658. ISSN: 1745-2473. URL: <http://dx.doi.org/10.1038/nphys1759>.
 - [120] F. Krüger, S. Kumar, J. Zaanen, and J. van den Brink. “Spin-orbital frustrations and anomalous metallic state in iron-pnictide superconductors”. In: *Phys. Rev. B* 79 (2009), p. 054504. URL: <http://link.aps.org/doi/10.1103/PhysRevB.79.054504>.
 - [121] W. Lv, F. Krüger, and P. Phillips. “Orbital ordering and unfrustrated $(\pi,0)$ magnetism from degenerate double exchange in the iron pnictides”. In: *Phys. Rev. B* 82 (2010), p. 045125. URL: <http://link.aps.org/doi/10.1103/PhysRevB.82.045125>.
 - [122] W. Lv and P. Phillips. “Orbitally and magnetically induced anisotropy in iron-based superconductors”. In: *Phys. Rev. B* 84 (2011), p. 174512. URL: <http://link.aps.org/doi/10.1103/PhysRevB.84.174512>.
 - [123] J.-H. Chu, J. G. Analytis, D. Press, K. De Greve, T. D. Ladd, Y. Yamamoto, and I. R. Fisher. “In-plane electronic anisotropy in underdoped $\text{Ba}(\text{Fe}_{1-x}\text{Co}_x)_2\text{As}_2$ revealed by partial detwinning in a magnetic field”. In: *Phys. Rev. B* 81 (2010), p. 214502. URL: <http://link.aps.org/doi/10.1103/PhysRevB.81.214502>.
 - [124] P. M. R. Brydon and C. Timm. “Theory of the excitonic spin-density-wave state in iron pnictides”. In: *Phys. Rev. B* 79 (2009), p. 180504. URL: <http://link.aps.org/doi/10.1103/PhysRevB.79.180504>.
 - [125] I. Paul. “Magnetoelastic Quantum Fluctuations and Phase Transitions in the Iron Superconductors”. In: *Phys. Rev. Lett.* 107 (2011), p. 047004. URL: <http://link.aps.org/doi/10.1103/PhysRevLett.107.047004>.
 - [126] M. Daghofer, A. Nicholson, and A. Moreo. “Spectral density in a nematic state of iron pnictides”. In: *Phys. Rev. B* 85 (2012), p. 184515. URL: <http://link.aps.org/doi/10.1103/PhysRevB.85.184515>.

-
- [127] D. J. Singh and M.-H. Du. “Density Functional Study of $\text{LaFeAsO}_{1-x}\text{F}_x$: A Low Carrier Density Superconductor Near Itinerant Magnetism”. In: *Phys. Rev. Lett.* 100 (2008), p. 237003. URL: <http://link.aps.org/doi/10.1103/PhysRevLett.100.237003>.
 - [128] Z. Hai-Jun, X. Gang, D. Xi, and F. Zhong. “Enhanced Orbital Degeneracy in Momentum Space for LaOFeAs ”. In: *Chinese Physics Letters* 26 (2009), p. 017401. URL: <http://stacks.iop.org/0256-307X/26/i=1/a=017401>.
 - [129] Y. Zhang, F. Chen, C. He, B. Zhou, B. P. Xie, C. Fang, W. F. Tsai, X. H. Chen, H. Hayashi, J. Jiang, H. Iwasawa, K. Shimada, H. Namatame, M. Taniguchi, J. P. Hu, and D. L. Feng. “Orbital characters of bands in the iron-based superconductor $\text{BaFe}_{1.85}\text{Co}_{0.15}\text{As}_2$ ”. In: *Phys. Rev. B* 83 (2011), p. 054510. URL: <http://link.aps.org/doi/10.1103/PhysRevB.83.054510>.
 - [130] S. Raghu, X.-L. Qi, C.-X. Liu, D. J. Scalapino, and S.-C. Zhang. “Minimal two-band model of the superconducting iron oxypnictides”. In: *Phys. Rev. B* 77 (2008), p. 220503. URL: <http://link.aps.org/doi/10.1103/PhysRevB.77.220503>.
 - [131] M. Daghofer, A. Moreo, J. A. Riera, E. Arrigoni, D. J. Scalapino, and E. Dagotto. “Model for the Magnetic Order and Pairing Channels in Fe Pnictide Superconductors”. In: *Phys. Rev. Lett.* 101 (2008), p. 237004. URL: <http://link.aps.org/doi/10.1103/PhysRevLett.101.237004>.
 - [132] A. Moreo, M. Daghofer, J. A. Riera, and E. Dagotto. “Properties of a two-orbital model for oxypnictide superconductors: Magnetic order, B_{2g} spin-singlet pairing channel, and its nodal structure”. In: *Phys. Rev. B* 79 (2009), p. 134502. URL: <http://link.aps.org/doi/10.1103/PhysRevB.79.134502>.
 - [133] G. Xu, W. Ming, Y. Yao, X. Dai, S.-C. Zhang, and Z. Fang. “Doping-dependent phase diagram of LaOMAs ($\text{M}=\text{V}-\text{Cu}$) and electron-type superconductivity near ferromagnetic instability”. In: *EPL (Europhysics Letters)* 82 (2008), p. 67002. URL: <http://stacks.iop.org/0295-5075/82/i=6/a=67002>.
 - [134] P. A. Lee and X.-G. Wen. “Spin-triplet p -wave pairing in a three-orbital model for iron pnictide superconductors”. In: *Phys. Rev. B* 78 (2008), p. 144517. URL: <http://link.aps.org/doi/10.1103/PhysRevB.78.144517>.

- [135] M. Daghofer, A. Nicholson, A. Moreo, and E. Dagotto. “Three orbital model for the iron-based superconductors”. In: *Phys. Rev. B* 81 (2010), p. 014511. URL: <http://link.aps.org/doi/10.1103/PhysRevB.81.014511>.
- [136] K. Kubo and P. Thalmeier. “Multiorbital Effects on Antiferromagnetism in Fe Pnictides”. In: *Journal of the Physical Society of Japan* 78 (2009), p. 083704. URL: <http://dx.doi.org/10.1143/JPSJ.78.083704>.
- [137] R. Yu and Q. Si. “Mott transition in multiorbital models for iron pnictides”. In: *Phys. Rev. B* 84 (2011), p. 235115. URL: <http://link.aps.org/doi/10.1103/PhysRevB.84.235115>.
- [138] J. C. Slater and G. F. Koster. “Simplified LCAO Method for the Periodic Potential Problem”. In: *Phys. Rev.* 94 (1954), pp. 1498–1524. URL: <http://link.aps.org/doi/10.1103/PhysRev.94.1498>.
- [139] D. A. Papaconstantopoulos and M. J. Mehl. “The Slater–Koster tight-binding method: a computationally efficient and accurate approach”. In: *Journal of Physics: Condensed Matter* 15 (2003), R413. URL: <http://stacks.iop.org/0953-8984/15/i=10/a=201>.
- [140] H. Eschrig and K. Koepernik. “Tight-binding models for the iron-based superconductors”. In: *Phys. Rev. B* 80 (2009), p. 104503. URL: <http://link.aps.org/doi/10.1103/PhysRevB.80.104503>.
- [141] S.-H. Lee, G. Xu, W. Ku, J. S. Wen, C. C. Lee, N. Katayama, Z. J. Xu, S. Ji, Z. W. Lin, G. D. Gu, H.-B. Yang, P. D. Johnson, Z.-H. Pan, T. Valla, M. Fujita, T. J. Sato, S. Chang, K. Yamada, and J. M. Tranquada. “Coupling of spin and orbital excitations in the iron-based superconductor $\text{FeSe}_{0.5}\text{Te}_{0.5}$ ”. In: *Phys. Rev. B* 81 (2010), p. 220502. URL: <http://link.aps.org/doi/10.1103/PhysRevB.81.220502>.
- [142] K. Haule, J. H. Shim, and G. Kotliar. “Correlated Electronic Structure of $\text{LaO}_{1-x}\text{F}_x\text{FeAs}$ ”. In: *Phys. Rev. Lett.* 100 (2008), p. 226402. URL: <http://link.aps.org/doi/10.1103/PhysRevLett.100.226402>.
- [143] A. M. Oleś, G. Khaliullin, P. Horsch, and L. F. Feiner. “Fingerprints of spin-orbital physics in cubic Mott insulators: Magnetic exchange interactions and optical spectral weights”. In: *Phys. Rev. B* 72 (2005), p. 214431. URL: <http://link.aps.org/doi/10.1103/PhysRevB.72.214431>.

- [144] R. Yu, K. T. Trinh, A. Moreo, M. Daghofer, J. A. Riera, S. Haas, and E. Dagotto. “Magnetic and metallic state at intermediate Hubbard U coupling in multiorbital models for undoped iron pnictides”. In: *Phys. Rev. B* 79 (2009), p. 104510. URL: <http://link.aps.org/doi/10.1103/PhysRevB.79.104510>.
- [145] S.-H. Baek, D. V. Efremov, J. M. Ok, J. S. Kim, J. van den Brink, and B. Büchner. “Orbital-driven nematicity in FeSe”. In: *Nat Mater* 14 (2015), pp. 210–214. ISSN: 1476-1122. URL: <http://www.nature.com/nmat/journal/v14/n2/abs/nmat4138.html#supplementary-information>.

Zusammenfassung auf Deutsch

In dieser Dissertation werden elektronische Eigenschaften korrelierter Elektronensysteme mit Quanten-Cluster-Methoden behandelt. Ein großes Interesse gilt dabei der Frage nach dem Grundzustand von Dreiecksgittern bei $3/4$ -Füllung. An diesem Punkt wird die elektronische Zustandsdichte singulär und die Fermi-Fläche zeigt perfektes nesting. In solch einer Konstellation sind viele geordnete Zustände möglich. Ebenso könnte das System eine Instabilität in Richtung unkonventioneller Supraleitung entwickeln. Solch eine supraleitende Phase mit chiraler $d + id$ -Symmetrie ist womöglich der Grundzustand im Bereich schwacher Wechselwirkungen, während die Situation für starke Kopplung unklar ist.

Zusätzlich werden die vorgestellten Cluster-Methoden für Untersuchungen der Wechselwirkung zwischen Coulomb-Abstoßung und symmetriebrechender Mechanismen in der nematischen Phase von Eisen-Pniktiden benutzt. Die elektronischen Eigenschaften ändern sich beim Phasenübergang von der tetragonalen in die orthorhombische Phase stärker, als mit einem Phononen-getriebenen Phasenübergang erklärbar ist. Magnetische und orbitale Fluktuationen könnten diese Diskrepanz erklären. Ihr Einfluss soll mit Quanten-Cluster-Methoden untersucht werden.

Um die Effekte von Korrelationen in diesen Systemen behandeln zu können, werden Cluster-Perturbation-Theorie (CPT) und dessen variationelle Erweiterung VCA eingesetzt. Kurzreichweitige Korrelationen werden dabei numerisch exakt mit Exakter Diagonalisierung (ED) auf der Längenskala der Clustergröße einbezogen. Langreichweitige Wechselwirkungen können im Rahmen der VCA durch ein variationelles Optimierungsverfahren im Rahmen der Selbstenergie-Funktional-Theorie behandelt werden. Die Größe der Cluster wird durch ED stark eingeschränkt.

VCA-Rechnungen für das $3/4$ -gefüllte Dreiecksgitter werden mit verschiedenen Clustergrößen durchgeführt. Auftretende finite-size-Effekte erschweren dabei die Vergleichbarkeit von Resultaten unterschiedlicher Cluster. Bei schwachen Wechselwirkungen ist der Grundzustand supraleitend mit chiraler $d+id$ -Symmetrie, in Übereinstimmung mit früheren Berechnungen im Rahmen der Renormalisierungsgruppentheorie. Im Bereich starker Wechselwirkung sind Spindichte-Wellen (SDW) ener-

getisch bevorzugt gegenüber supraleitenden Phasen. Der Grundzustand ist kollinear und besitzt eine vierfach vergrößerte Einheitszelle mit ungleichgroßen lokalen Momenten. Ein in der Molekularfeld-Theorie vorhergesagter chiraler SDW-Zustand erwies sich durch die Berücksichtigung kurzreichweitiger Korrelationen nicht als Grundzustand im Bereich starker Wechselwirkungen. Bei mittleren Wechselwirkungen hat die Methode jedoch Schwächen und es können keine belastbaren Aussagen getroffen werden.

Um die Mechanismen zu behandeln, die in der nematischen Phase der Eisen-Pniktide zur Symmetriebrechung führen, wurde ein Drei-Band-Modell auf einem Cluster mit vier Plätzen genutzt. Mit CPT ist es möglich, kurzreichweitige magnetische Wechselwirkungen im Cluster zu implementieren, ohne langreichweitige Ordnung hervorzurufen - ein essenzieller Vorteil gegenüber der Molekularfeld-Theorie, in welcher diese nematische Phase nur schwer zugänglich ist. Drei Mechanismen wurden genutzt, um die vierzählige Gittersymmetrie zu brechen. Es wurden die Effekte anisotroper kurzreichweitiger magnetischer Kopplung, orbitaler Ordnung und anisotroper kinetischer Hüpfsterme auf die Spektraldichte verglichen. Trotz vergleichbarer Ergebnisse aller drei Szenarien ist eine Symmetriebrechung alleine durch Phononen unwahrscheinlich, da eine unphysikalisch große Anisotropie benötigt wird, um die Resultate aus ARPES-Messungen reproduzieren zu können.

Acknowledgements

A lot of people have provided me with help, answers to my questions, assistance, discussions and good temper during the last years. Since naming all of them would go beyond the scope, I will focus on the most important of them.

During my time at the ITF, Maria Daghofer always helped me with her enormous knowledge about pretty much everything and especially about physics. Discussions with here were always enlightening and led to new solutions. With her deep insight, Maria always encouraged me to try new paths and I am deeply grateful for her advices and her excellent mentoring.

I am especially thankful for Jeroen van den Brink and all other colleagues at the IFW, who provided an inspiring environment at the ITF. Grit Rötzer provided help whenever complications arose filling out applications and forms. Ulrike Nitzsche was always able to rescue the computer cluster from my programming attempts and provided quick solutions every time errors were encountered. I also thank my longtime office mate Frank Kirtschig for the pleasant atmosphere and enjoyable conversations.

Within the research training group GRK 1621 ‘Itinerant magnetism and superconductivity in intermetallic compounds’, Hans-Henning Klauß as the speaker and Marion Malkoc as the coordinator did excellent work within the GRK and I always enjoyed the time with the other fellows. My second advisor within the GRK was Carsten Timm. I am especially grateful to him for helping me at times Maria was busy and for advisory concerning scientific writing.

During the last three years, the TUD and the GRK gave me the opportunity to attend a lot of lectures. Many of them increased my knowledge in certain topics to a large extend. Additionally, the opportunity of being a supervisor for the exercises of two lectures was given to me.

Finally, I thank my family and friends for everything they do to support me and for all the precious moments we share together. My wife Elisabeth is the best mother for our son Finn that I can imagine and Finn has the special ability to always make

Acknowledgements

me happy when he is smiling. I thank my parents for always encouraging me to find my own way and my parents-in-law for supporting us in so many ways.

This dissertation is dedicated to my son Finn.

Publication List

1. *Breaking of fourfold lattice symmetry in a model for pnictide superconductors*
M. Daghofer and A. Fischer
Supercond. Sci. Technol. **25** 084003 (2012)

Abstract: We investigate the interplay of onsite Coulomb repulsion and various mechanisms breaking the fourfold lattice symmetry in a three-band model for the iron planes of iron-based superconductors. Using cluster-perturbation theory allows us to locally break the symmetry between the x and y directions without imposing long-range magnetic order. Previously investigated anisotropic magnetic couplings are compared to an orbital ordering field and anisotropic hoppings. We find that all three mechanisms for a broken rotational symmetry lead to similar signatures once onsite interactions are strong enough to bring the system close to a spin-density wave. The band distortions near the Fermi level are independent of differences between the total densities found in xz and yz orbitals.

A large part of this publication has been included in Chapter 4 of this dissertation.

Preprints to appear:

1. *Magnetic Ordering and Superconductivity in Triangular Lattices in the Hubbard Model*
A. Fischer and M. Daghofer
to appear (2015)

Abstract: The 2D triangular lattice provides a simple model with intrinsic geometric frustration and is therefore well suited to study effects induced by electronic interactions. The aim of this paper is to find possible ground state scenarios at the van-Hove filling within the Hubbard model, taking various magnetically ordered states and superconducting states into account. Using cluster perturbation theory allows us to treat the system on a level beyond

mean field theory. We find a time reversal symmetry breaking chiral superconducting state to be the supported ground state at weak couplings. In the strong coupling limit magnetically ordered states might beat superconductivity. A comparison of selected magnetically ordered states does not show a support of a previously proposed chiral phase.

A large part of this publication have been included in Chapter 3 of this dissertation.